SYNTHESIS AND CHARACTERIZATION OF GRAPHITIC CARBON NITRIDE BASED NANOSTRUCTURED COMPOSITES

BY

ADEKOLAPO ADENIRAN ADESIDA

A Thesis Presented to the
DEANSHIP OF GRADUATE STUDIES

KING FAHD UNIVERSITY OF PETROLEUM & MINERALS

DHAHRAN, SAUDI ARABIA

In Partial Fulfillment of the
Requirements for the Degree of

MASTER OF SCIENCE

In

CHEMISTRY

MAY, 2015.

KING FAHD UNIVERSITY OF PETROLEUM & MINERALS
DHAHRAN- 31261, SAUDI ARABIA
DEANSHIP OF GRADUATE STUDIES

This thesis, written by **ADEKOLAPO ADENIRAN ADESIDA** under the direction his thesis advisor and approved by his thesis committee, has been presented and accepted by the Dean of Graduate Studies, in partial fulfillment of the requirements for the degree of **MASTER OF SCIENCE IN CHEMISTRY.**

Dr. Al-Saadi, Abdulaziz Abdulrahman
Department Chairman

Dr. Salam A. Zummo
Dean of Graduate Studies

26/5/15
Date

Dr. Al-Arfaj, Abdulrahman Ahmed
(Advisor)

Dr. Tawfik Abdo Saleh
(Member)

M. A. Gondal
Dr. Mohammad Ashraf Gondal
(Member)

DEDICATED TO MY PARENT, SIBLINGS AND FAMILY.

Acknowledgement

I want to thank almighty God for giving me the opportunity, strength, wisdom, and adaptability to be able to finish this research successfully.

I also want to express my gratitude to the government of the kingdom of Saudi arabia for extending this opportunity to my country, which I am a full beneficiary. In that wise, I thank the staff of King Fahd University of petroleum and minerals for making my master degree study convenient for me during my stay.

Furthermore, I wish to express my acknowledgement to Dr. Al-Arfaj, Abdulrahman Ahmed, who served as my main supervisor for his guidance, patience and encouragement thought the research. I also want to appreciate the massive effort of Dr. Mohammad Ashraf Gondal, my committee member, who made sure to attend to my need at all-time possible and gave me advise which helped me to stay focused and eventually triumph on this path; and also Dr. Tawfik Abdo Saleh` s consistent effort, advice and encouragement on the road to the successful completion of this work which cannot be ignored, and it is well appreciated.

I also want to appreciate the effort of the chairman of Chemistry department, Dr. Al-Saadi, Abdulaziz Abdulrahman for his provision of an excellent academic environment and enabling facilities.

I am indeed grateful to all my lecturers and other faculty members who have in one way or the other helped me with one advice or the other to make my research possible and convenient in the department.

I will also like to recognize the assistance and appreciate the effort of M. Dastageer, Inayatuh Rehman, Rashid Siddique, M arif, Pilli, Xiaofeng Chang and the entire member of the laser group.

I also want to appreciate the Nigerian community that made the stay a worthwhile and less lonely.

I will like to appreciate the support and assistantship by King Fahd University of petroleum and minerals under Centre of Excellence in Nanotechnology.

Last, but not the least is the encouragement and prayers I got from home and abroad from my loving parents (Mr and Mrs Adesida), siblings (Mr Adeleke Adesida, Mrs Ronke Oludare, and Mr Adewale Adesida) and my cousins, uncles, aunties and friends towards the successful completion of my master's degree. I am forever grateful.

TABLE OF CONTENTS

LIST OF TABLES

LIST OF FIGURES

LIST OF ABBREVIATIONS

CB : Conduction Band

DRS : Diffused Reflectance Spectroscopy

FESEM : Field Emission Scanning Electron Microscope

HRTEM : High Resolution Transmission Electron Microscope

ROS : Reactive Oxygen Species

MOS : Metal Oxide Semiconductor

NHE : Normal Hydrogen Electrode

NPs : Nanoparticles

Rh B : Rhodamine B

SPR : Surface Plasmon Resonance

TOC : Total Organic Carbon

UV : Ultraviolet

VLD : Visible Light Driven

XRD : X-ray Diffraction

XPS : X-ray Photoelectron Spectroscopy

Abstract

Full Name : Adekolapo Adeniran Adesida

Thesis Title : Synthesis and Characterization of Graphitic Carbon Nitride based nano structured composite

Major Field : Chemistry

Date of Degree : April, 2015.

This Master thesis deals with preparation of series of WO_3/g-C_3N_4 and Au/Ag/ g-C_3N_4 composites with different mass ratios. WO_3/g-C_3N_4 composite was prepared by simple pyrolysis method, using tungstic acid and melamine as the starting materials; while Au/Ag/ g-C_3N_4 was prepared by wet incipient impregnation and photodeposition methods using gold chloride , silver nitrate, and melamine as precursors. The microstructure and optical properties of as-synthesized WO_3/g-C_3N_4 composites were investigated by X-ray diffraction, UV–Vis diffuse reflection spectroscopy, field emission scanning electron microscopy (FESEM), and photoluminescence spectroscopy; and also high-resolution transmission electron microscopy (HRTEM) was also used to study the nanostructure property of the as-synthesized Au/Ag/ g-C_3N_4 composites.

Compared with WO_3, g-C_3N_4 and well-known commercial photocatalysts, an improved visible-light-induced photodegradation of Rhodamine B and methyl tertiary butyl ether in aqueous solution was observed on WO_3/g-C_3N_4 composite, due to the high carrier separation efficiency at the interface between WO_3 and g-C_3N_4. Moreover, the photoactivity and photostability of catalyst after many runs was also evaluated**.** Furthermore**,** studies revealed that the synthesized g-C_3N_4 doped with silver and gold nanoparticles (Au/Ag/g-C3N4) were having a range of 12 to 50 nm. The nano-catalysts were also applied for the removal of organic contaminants (dyes). The effect of different experimental parameters such as mass ratio, dopants content, and exposure to irradiation time on removal of dye was investigated. Results showed that various parameters mentioned above have effect on the photoactivity of the catalysts. Reaction kinetics for the degradation process was also discussed.

ملخص الرسالة

الاسم بالكامل : أديكولابو أدريان أديسينا

عنوان الرسالة : تخليق وتشخيص نتريدات الكربون الجرافيتيه نانوية التركيب المركبة

التخصص : الكيمياء

تاريخ نيل الدرجة : أبريل, 2015

بحث الماجستير هذا يعنى بتحضير سلاسل من $WO_3/g\text{-}C_3N_4$ and $Au/Ag/\ g\text{-}C_3N_4$ المركبة بمختلف النسب الوزنية. $WO_3/g\text{-}C_3N_4$ المركب تم تحضيره بطريقة التحلل الحراري البسيطة, باستخدام حمض التنجستيك و الميلامين كمواد بادئة; في حين تم تحضير $Au/Ag/\ g\text{-}C_3N_4$ بطريقة التشريب الرطب الاولية و الايداع الضوئي باستخدام كلوريد الذهب ونترات الفضة و الميلامين كمواد اولية التركيب الدقيق والخصائص الضوئية لمركبة $WO_3/g\text{-}C_3N_4$ المخلق تم فحصها بحيود الاشعة السينية, مطيافية انتشار الانعكاس للضوء المرئي والاشعة فوق البنفسجية, انبعاث مجال المجهر الماسح الضوئي, وايضا مجهر الانتقال الالكتروني ذو الدقة العالية تم استخدامه لدراسة خصائص التريب النانوي لمركبات $Au/Ag/\ g\text{-}C_3N_4$ المخلقة مقارنة WO_3, $g\text{-}C_3N_4$ مع الحفاز الضوئي المعروف جيدا المتوفر تجاريا تمت ملاحظة تحسن في التكسير الضوئي المستحث ضوئيا للرودامين (ب) و ايثر ميثيل ثلاثي البيتويل في الوسط المائي على مركب $WO_3/g\text{-}C_3N_4$, بسبب الفصل بالحمل عند التداخل بين WO_3و$g\text{-}C_3N_4$, اضافة الى ذلك تمت دراسة الفعالية الضوئية والثبات الضوئي للحفاز بعد اجراء عدة تجارب عليه, وايضا اظهرت الدراسات ان $g\text{-}C_3N_4$ المخلق المدخل علية جسيمات الذهب والفضة النانوية ($Au/Ag/g\text{-}C_3N_4$)لديها مدى من 12 الى 50 نانوميتر. ايضا تم تطبيق الحفاز النانوي في عمليات ازلة الملوثات العضوية (الاصباغ). تم فحص تاثير المتغيرات العملية مثل النسب الوزنية, كمية الذرات المدخلة, وزمن التعريض للأشعاع.أظهرت النتائج ان كل هذه المتغيرات لها تاثير على الفغالية الضوئية للحفاز. ايضا تمت مناقشة حركية التفاعل لعملية التكسير .

CHAPTER 1

INTRODUCTION

Owing to the effect of global warming on the atmosphere and global energy demands, the need for an alternative clean energy to address environmental and energy issue cannot be neglected [1]. Among the alarming environmental issues is the lack of fresh water supply especially among underdeveloped and developing countries, owing to factors such as underdevelopment of infrastructures, industrial growth etc. Water is a very important component of the human body. Lack of clean water in the body also known as dehydration could lead to reduction in mental performance and physical coordination. This also leads to inhibition in several basic physical processes such as muscle movement, breathing, digestion etc. Especially in developing countries, wastewater is mostly discharged into streams and river directly without proper treatment. This in turn results into a lot of incurable water borne diseases that causes a lot of death in underdeveloped and developing nations. Hence, a clean water source is a prerogative of every nation for healthy living. Several sectors of the economy such as construction, agriculture, chemical industries also make use of a large amount of water to realize their services. Developed and industrialized countries most of the times encounter enormous array of environmental issues associated with rectification of hazardous wastewater, groundwater and toxic air treatment. Industrial and municipal wastewater have been found to contain wide range of organic pollutants [2]. The release of organic pollutants like dyes in wastewater in our environment is a source of pollution, perturbation and eutrophication in aquatic life. Rhodamines B (RhB) as well as some N-containing dyes undergo natural reductive anaerobic degradation to yield potentially carcinogenic aromatic amines; and most of the dyes are resistant to direct photolysis and biodegradation [3, 4]. Synthetic organic substances like Nitrogen-containing contaminants such as rhodamine B, present in these wastewaters, constitute harsh problem in biological treatment systems as a result of their resistance to biodegradation and conventional treatment, and have proved abortive and environmentally not compatible [4, 5]. Hence, there is need for pretreatment methods to reduce the concentration of organic pollutants form water bodies before reuse, prevent exposure to disease causing microbes, preserve aquatic life and wild life habitat, and eventually promote public hygiene. Several conventional techniques for remediation of contaminants such as adsorption, flocculation/sedimentation, membrane separation, distillation/evaporation, high temperature incineration, ozonation, chlorination, ion exchange, reverse osmosis, aeration, chemical oxidation and extraction have all been utilized in the past. However, most of the techniques above have a drawback in that the products formed after require further treatment since they are most times not biodegradable. Hence, the application of alternative treatment technologies, like photocatalytic technology applying semiconductor particulate system, is of great appeal than other conventional methods, for decomposition of toxic compounds to non-hazardous products [5-10].

Abundance of sunlight containing a large amount of visible light ensures photocatalytic technology is worth considering. This is because the techhnology ensures complete degradation of dissolved organic pollutants in water and soil into harmless and environmental friendly byproducts like carbondioxide and water. Advanced oxidation process (phocatalytic technology) also has an advantage of being able to be carried out under mild conditions of low temperature, pressure and energy consumption in comparison to other conventional techniques. Ever since the report of fujishima and Honda in 1972 about the light-driven splitting of water into H_2 and O_2 with the aid of TiO_2 [11], photocatalytic process with semiconductor has become a promising technology in combating environmental and energy global demand issues. Applications like production of renewable fuel [1, 12-16] via degradation of carbondioxide and water splitting into production of hydrogen for fuel cell technology [11, 17] are made possible efficiently and environmentally friendly by photocatalytic process.

Photocatalytic technology involves the application of a substance, semiconductors mostly, to energise and speed up a light-sensitive reaction without experiencing deterioration.

Principally, when a solid undergoes photoactivation, whereby an equally energetic photon is absorbed by a semiconductor; an electron is excited from a valence band where a hole is created, to the conduction band as shown in fig 1.1 [5]. Semiconductors have a vacant energy region where no energy levels are capable of recombining the electron and the positively charged hole. The unoccupied energy region which extends from top of the filled valence band and the bottom of the vacant conduction band is called band gap. Following the generation of the positive holes and the electrons under photocatalytic effect, redox (oxidation and reduction) reactions takes place at the surface of semiconductors [5, 18]. Hydroxyl and peroxide radicals can react with the electrons as well as organic compounds with valence bond holes through oxidative degradation [7]. The conversion efficiency of redox reaction initiated by the photogeneration of e^{-}-h^{+} depends on larger band gap energy than desired reaction, suitability of CB and VB for induced redox processes, and faster redox reaction rate than e^{-}-h+ recombination process [5, 18].

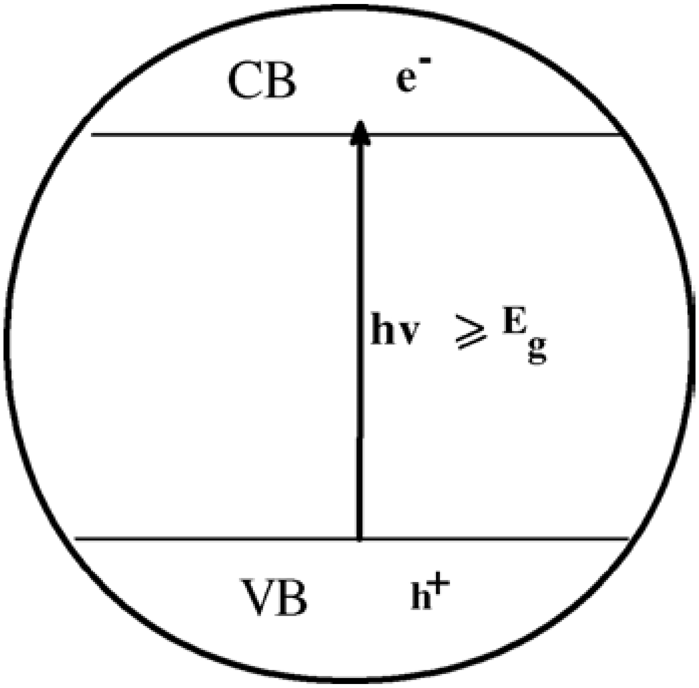

Figure 1.1 e−– h+ pair formation by illuminated semiconductor particle from valence band (VB) to the conduction band (CB)

Also, focus on photocatalytic technology has been shifted onto use of nano structured particles. Knowing that the size of a particle has an inverse relationship with the surface area; increase in surface area in nanoparticles can be utilized to maximize light absorption [19]. Furthermore, the band gap energy is directly related to the particle size. Decreasing the particle size of the photocatalyst to an extent ensures a display of high band gap energies in that there is a valence band energy shift to lower energies whereas the conducting band shifts to the higher energies. On the contrary, with significant narrow band gap energy, it is difficult to achieve required redox potentials for the redox reaction necessary for the process. Hence, there is a need to develop a nano structure which demonstrates efficient band gap energy range and improved particle size.

In the whole energy of incoming solar spectrum, ultraviolet radiation (k < 400 nm) accounts to only less than 4% [6, 8], while the visible light (380-800)nm is around 42% [20]. Hence, effective utilization of the visible light of solar radiation, as in the photosynthesis of plants, has been a long ‘‘dream’’ of the photochemical researchers. Hence, effort has to be made to synthesize material with visible light absorption edge. Otherwise, materials that absorb in the UV region have to either be improved by combination with other semiconductors or be doped with metals or nonmetals to shift their absorbing edges.

Since the discovery by Fujisima and Honda in 1972 for photocatalytic splitting of water into oxygen and hydrogen [11], semiconductor TiO_2 in presence of UV radiation has become the benchmark photocatalyst for degradation of water bound pollutants as documented in the literature. This is due to its availability, nontoxicity, efficiency, high chemical stability and superior photoactivity [21]. Nevertheless, the drawback of TiO_2 semiconductor is that it absorbs a small portion of solar spectrum in the UV region with band gap energy between 3.0eV–3.2 eV [6, 20-23]. Although semiconductors with large band gaps have strong photo activity but they are limited to UV absorption only.

In addition to TiO_2, several other semiconductors (oxides, sulphides such as WO_3, TiO_2, ZnO, ZnS, CdS, In_2O_3etc.) have been also probed and have been found useful as catalyst in advanced oxidation processes owing to their suitable entirely occupied valence band and vacant conduction band [24]. Among the oxides, the rutile and anatase forms of TiO_2 exhibits better performance when irradiated due to properties highlighted above[19, 24]. Also, the formation of $Zn(OH)_2$ from unstable ZnO deactivates the catalyst and makes it less efficient. Sulphides of cadmium and zinc are alternatives but they undergo self-oxidation which leads to photo corrosion.

Hence, there is a need to develop a high photoactivity, visible light sensitive, good particle size and band gap energy range catalysts, such as g-C_3N_4 based materials with narrow band gap 2.8eV [20], to exploit more solar power energy. Therefore, the development of new materials (visible light sensitive catalyst with tunable properties, narrow and appropriate band gap) is needed to increase the activity for the practical applications using visible/solar energy.

Since it was first studied and reported as a visible light response catalyst in 2009 by wang et al for hydrogen production via water splitting[25]; graphitic carbon nitride has been widely accepted and improved upon to counter its disadvantage of high recombination of photogenerated e^--h^+, which reduces its photoactivity.

Thus, for efficiency and high conversion of solar power, this thesis investigated g-C_3N_4 based semiconductors with following properties:

A) non-toxicity

B) large surface area,

C) broad absorption spectra with high absorption coefficients,

D) Tunable properties which can be modified by size reduction, doping, photosensitizers

E) Facility for multielectron transfer process and

F) High activity stability.

Thus, g-C_3N_4 based nano structured materials was synthesized, investigated and doped in different portions with metals and nonmetals with appropriate properties to improve its efficiency.

General scheme for advanced oxidation process (photocatalysis) is shown below in fig 1.2. Typically, the semiconductor absorbs photons with energy value higher than band gap energy of the semiconductor which then excites electron to the conduction band and creates a hole in the valence band. The e^--h^+ generated can drive a redox reaction depending on following factors:

A) Band gap energy between e– and h+ is larger than the energy required for desired reaction.

B) The redox potentials of the e– and h+ (thus the position of CB and VB) are suitable for inducing redox processes.

C) The rates of these redox reactions are faster than or at least fast enough to compete with the e– – h+ recombination.

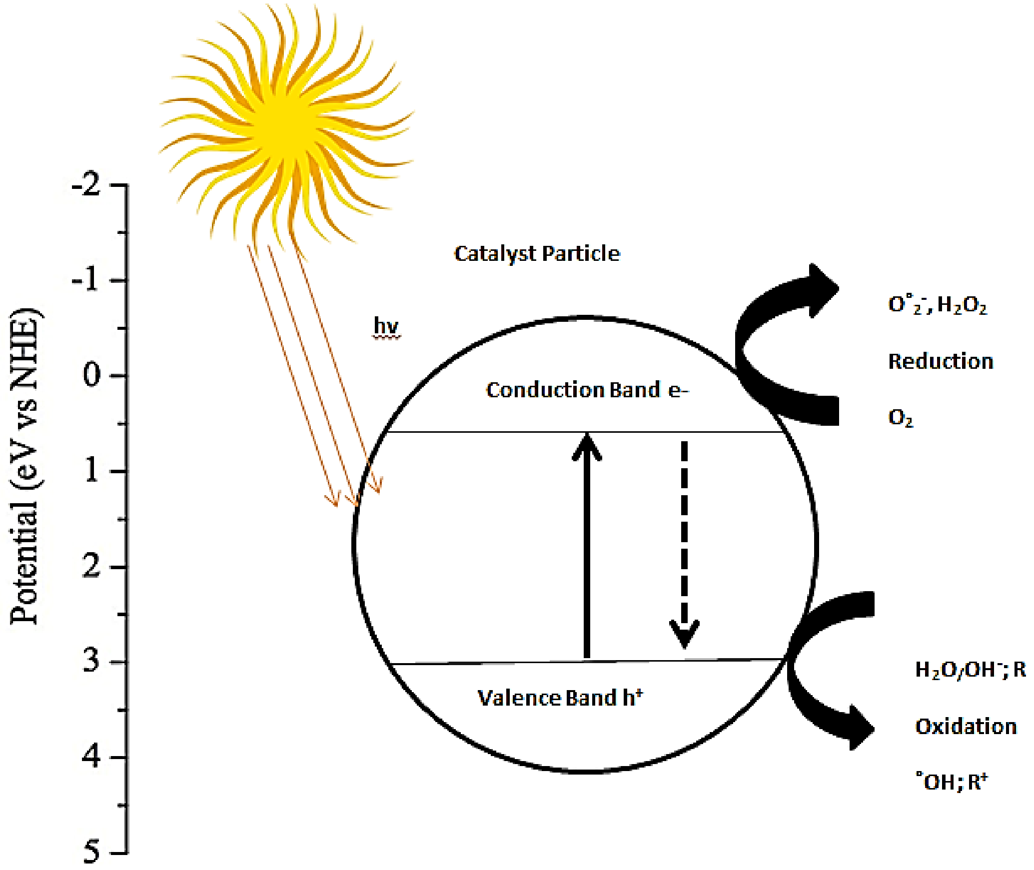

Figure 2.2 Schematic diagram of photocatalytical process initiated by photon acting on the semiconductor

Hence, atmospheric oxygen and water molecules at the surface of the photocatalyst reacts with the e– and h+ generated; and yields oxidizing intermediates such as superoxide radicals, hydroxyl radicals etc. which are capable of oxidative degradation of organic pollutants according to the following equations below.

$$SC + hv \longrightarrow SC\,(e^{-}_{cb}, h^{+})$$

$$SC\,(h^{+}) + D_{ads} \longrightarrow SC + D^{+}_{ads}$$

$$SC\,(e^{-}_{cb}) + A_{ads} \longrightarrow SC + A^{-}_{ads}$$

$$HO^{o} + HO^{o} \longrightarrow H_2O_2 \longrightarrow H_2O + 1/2\,O_2$$

$$SC\,(e^{-}_{cb}) + H^{+} \longrightarrow SC + H^{o}$$

$$H^{o} + H^{o} \longrightarrow H_2$$

$$HO^{o} + H^{o} \longrightarrow H_2O\ \text{(Recombination)}$$

$$H_2 + 1/2\,O_2 \longrightarrow H_2O\ \text{(Recombination)}$$

$$O_{2(ads)} + e^{-}_{cb} \longrightarrow O_2^{o-}$$

$$H^{+} + O_2^{o-} \longrightarrow H_2O^{o}$$

$$e^{-}_{cb} + h^{+} \longrightarrow \text{heat (Recombination)}$$

A_{ads} = Adsorbed acceptor D_{ads} = Adsorbed donor

SC = Semiconductor

In this thesis, effort was made to investigate the improvement of the performance of the graphitic carbon nitride through the photocatalytic degradation of toxic dye (organic pollutant), Rhodamine B, using graphitic carbon nitride combined with metal oxide (tungstic oxide) and doped graphitic carbon nitride with silver and gold nanoparticles. Several modified samples of graphitic nitride (pure, combined with metal oxides in different mass ratios, doped with metal and nonmetal nanoparticles) were synthesized by several methods such as hydrothermal and photodeposition. Synthesized materials were applied for removal of contaminants from water using Xenon lamp irradiation with cut-off light filters restricting the irradiation to visible region [20].

The daunting challenge of graphitic carbon nitride as a semiconductor is the high recombination of photogenerated e^--h^+, which reduces its photoefficiency. Efforts have been made to overcome the e_{cb}^--h_{vb}^+ recombination process by coupling g-C_3N_4 with other suitable catalyst such as tungstic oxide, metal/nonmetal species etc.

In this study, two different techniques were utilized to inhibit the e^--h^+ recombination effect which eventually improves the photo efficiency of graphitic carbon nitride. Firstly, in combination with a suitable metal oxide, the recombination effect is reduced by the formation of heterostructure junction between the two semiconductors owing to the synergetic effect between them.

Secondly, the strong surface plasmonic effect of electron trappers such as gold and silver nanoparticles which helps to improve the photocatalytic performance of g-C_3N_4 was effectively studied and investigated. Surface plasmon resonance (SPR) effect has its source ascribed to the aggregate oscillation of the available conduction electrons on the surface of metal nanoparticles, driven by an interacting electromagnetic field [26, 27]. Nanoparticles of noble and alkali metals such as gold, silver, copper display good optical properties by having broad absorption in the visible region due to this effect [27].

The influence of irradiation time, catalyst concentration, dopant concentration on the graphitic carbon nitride was also investigated.

The objective of the research work was to synthesis graphitic carbon nitride based nano structured composites like g-C_3N_4/WO_3, g-C_3N_4/Ag/Au, etc. The g-C_3N_4/Ag/Au composite was doped by silver and gold nanoparticles through photodeposition technique, while the g-C_3N_4/WO_3 composite was synthesized using facile preparation method. Structural and microstructural characterization was performed and investigated using High Resolution Transmission Electron Microscope (HRTEM) and Field Emission Scanning Electron Microscope (FESEM) characterization techniques respectively, while X-ray Photoelectron Spectroscopy (XPS) for chemical analysis (surface composition), and UV-VIS spectrophotometry (reflectance, transmittance) for optical study. X-ray Diffraction (XRD) and Grazing Angle X-ray Diffraction (GAXRD) were applied in examining the mineralogical properties of the materials. We investigated photocatalysis experiment with different light sources, i.e. (i) sunlight, (ii) visible light using xenon lamp (having different light filters).

The synthesized materials were applied to investigate the degradation of rhodamine B. Rhodamine B (Rh B) is a nitrogen-containing organic pollutant (as shown in the fig 1.3 below), which can be found in the effluent of industries such as textile, cosmetic etc. Rhodamine B is not responsive to direct photolysis and biodegradation; and also it undergoes anaerobic degradation to produce latently carcinogenic aromatic amines [3]. Several conventional treatment method such as flocculation, filtration etc. have been used but they are ineffective and not environmentally friendly [5]; hence the application of advanced oxidation process.

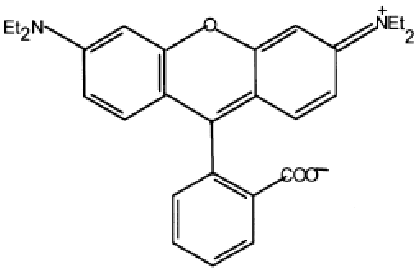

Figure 1.3 Rhodamine B structure

The effect of different catalys and dopant composition were analytically and properly studied. It was observed that under the given experimental conditions, the rhodamine B degradation followed a pseudo first order kinetics.

1.1 Overview of Dissertation

This dissertation consists of four chapters.

This chapter introduces the advanced oxidation process. It also introduces the application of several semiconductor catalysts for this process. Their different synthesis methods were also discussed.

The following chapter (chapter two) deals with literature review of various syntheses of different catalysts and their application. Also, the various application of graphitic carbon nitride was also reviewed.

The third chapter deals with the experimental methods used to synthesize different catalysts, and various characterization techniques for analysis. It also contains details about the application procedure used to evaluate the performances of the catalysts.

In chapter four, details about the synthesis, characterization and application of the various composites prepared were fully discussed.

1.2 Objectives

The major objective of the proposed study is to study graphitic carbon nitride semiconductors, and to improve their efficiency by combination with another suitable semiconductor or through doping of metals and nonmetals. However specific objectives are as follows:

I. Synthesis of g-C_3N_4 based nano structured composites doped in different portions by various methods such as hydrothermal, pyrolysis, photodeposition and sol-gel methods.

II. Characterization and morphological studies of synthesized photocatalysts using Fourier Transform Infra-red (FTIR), High Resolution Transmission Electron Microscope (HRTEM), Field Emission scanning electron microscopy (FESEM), x-ray diffraction (XRD), UV-VIS spectrophotometry (reflectance, transmission) and X-ray spectroscopy (XPS).

III. Development of an experimental setup to evaluate the performance of the prepared catalysts i.e. (i) using visible light source (xenon lamp and natural sunlight) and (ii) with laser light; for removal of pollutants from water.

Absorbance of the standard solutions will be measured before irradiation with catalyst and reflectance of different light filters using UV-spectrophotometer.

CHAPTER 2

LITERATURE REVIEW

2.1 Heterogeneous Catalysts

Environmental friendly waste water treatment method is an important process to conserve water, to save human and aquatic life from toxic organic and inorganic content in industrial and municipal water, with a technique that does not in turn pollute the air. In the past, methods that have been used include activated carbon adsorption, chemical oxidation and biological digestion. Advanced oxidation process with TiO_2/UV light [2] edges the former techniques with advantages like lack of mass transfer limitations when nanophotocatalyst is involved, process been carried out at ambient temperature, and the potential use of available and cheap solar power [5].

Titanium dioxide, TiO_2 under irradiation by ultraviolet rays of natural or artificial lighting, has been found effective in adavanced oxidation technology with advantages like high oxidizing power, availability, non-toxicity and stability. Drawback of TiO_2 includes low catalytic efficiency due to faster rate of recombination process of e^- and h^+, which has limited its use and demanded of researchers a way to incorporate other materials by doping to complement its properties or discover better and tunable visible light driven photocatalyst. Irradiation of TiO_2 photocatalyst with light of energy equal to or greater than its band gap energy generates positive holes in the valence band and excites the electrons to the conduction band. Photogenerated positive holes can react with adsorbed H_2O to form hydroxyl radicals while the electrons react with O_2 to form superoxide radicals. Highly reactive hydroxyl and superoxide radicals can oxidize the pollutants in solution or react with adsorbed pollutants. Otherwise, the electron and hole pairs can recombine. In order to overcome the limitations of TiO_2 (high band gap energy (3.2 eV) and high recombination rate of e^- and h^+), many attempts have been made to prepare different modification of TiO_2 by depositing of noble metals and incorporating metal oxides to improve the separation between free charge carriers.

Exploitation of photocatalyst response to visible light can take two different approaches. Firstly, UV-active oxides like TiO_2 and $InTaO_4$ can be doped with metals and non-metals species to become visible light sensitive by impregnation method. Zhenfeng Bian et al. reported a strong photochemical response in the visible region due to surface plamonic resonance of TiO_2 doped with gold nanoparticles (NPS) [26]. Sammy W. Verbruggen et al. also reported spatial organization of the metal nanoparticles in contact with $TiO_2/Au_xAg_{(1-x)}$ alloy nanoparticles displaying a strong composition-dependent surface plasmon resonance in the visible light region of the spectrum [28-31].

Second approach that has been investigated is the synthesis of different visible light sensitive metal oxide composites by hydrothermal or sol-gel methods [32], such as nano structured WO_3 [33], $Bi_2WO_6/BiVO_4$ [34], $BiOCl/Bi_2O_3$ [35], and BiOCl/BiOBr [36]. The improved photocatalytic activity in the above composites is due to the synergy effect and heterojunction formed between different oxides reacted together.

2.2 Graphitic Carbon Nitride as a Visible Light Driven Catalyst

Recently, g-C_3N_4 has emerged an intriguing choice as photocatalyst, although a polymeric imitative was initially synthesized by Berzelius and termed by Liebig in 1834 as “melon” to be one of the oldest synthesized polymers [37].

G-C_3N_4 possess the highest stability of all the allotropes of carbon nitride, and it is a polymeric semiconductor majorly comprising carbon and nitrogen, for which organic reactions can be applied in altering its reactivity without having much of its composition changed [37]. The skeleton topology initially identified in g-C_3N_4 is in fact hypothetically a defect-rich, N-bridged “poly(tri-s-triazine)” [38]. With the s-triazine ring (C_3N_3) being aromatic, it is anticipated that a two-dimensional, conjugated polymer of s-triazine would incline to form a p-conjugated planar layers resembling the type like graphite, which has been confirmed by wide-angle X-ray diffraction (XRD) patterns, SEM and TEM investigations [38]. The tri-s-triazine ring framework (shown in fig 2.1) possessing a high condensation rate allows the polymer a high degree of stability thermally (up to 600˚C in air) and chemically (e.g. acid, base, and organic solvents) and a suitable electronic structure, having an indirect semiconductor medium-bandgap [38]. This in turn permits its application directly in sustainable chemistry as a versatile and all-purpose heterogeneous metal-free visible light driven catalyst, for example in oxidative degradation of organic pollutants [20, 39, 40] or hydrogen production from water splitting [25].

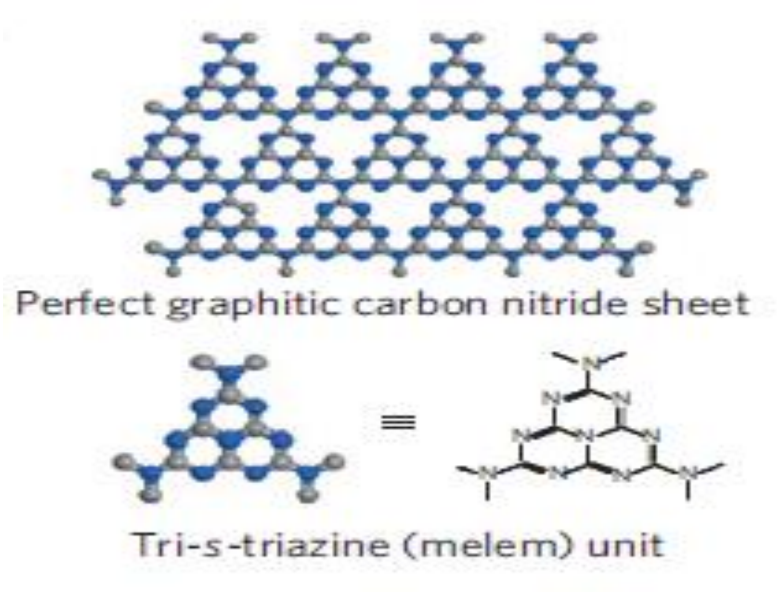

Figure 2.1 Melem structure and interlayer structure of g-C_3N_4

In 2009, Wang et al. first reported the synthesis of novel molecular photocatalyst of polymeric graphitic carbon nitride (g-C_3N_4) used in application for H_2 production [25]. Quickly thereafter, relevant investigations were conducted owing to its advantages such as nontoxicity, high photostability in pH range (0–14), ease to be prepared and narrow band gap (2.7eV). However, it has disadvantage such as high recombination rate of the photogenerated charge carriers. Incorporating other appropriate semiconductor materials to form a heterojunction structure is a novel and efficient route to improve its photoactivity. Composites that exhibit heterojunction properties with graphitic nitride has been reported such as, WO_3/g-C_3N_4 [20], Bi_2WO_6/g-C_3N_4 [41], g-C_3N_4/$BiOCl_xBr_{1-x}$ [40], g-C_3N_4/Ag_3PO_4 [18], Ag/AgBr/g-C_3N_4 [8], g-C_3N_4/ZnO [42], g-C_3N_4 /Cu_2O [43], g-C_3N_4–TiO_2 [44, 45], Co_3O_4-g-C_3N_4 [46], In_2O_3/g-C_3N_4 [47], g-C_3N_4/Ag_3VO_4 [48], g-C_3N_4/MoO_3 [49], g-C_3N_4/$SmVO_4$ [50], MWNTs/g-C_3N_4 [51], Fe_3O_4/g-C_3N_4 [52].

Guohui Dong et al also recently prepared by facile method, a porous graphene like carbon nitride, which was then successfully applied in the removal of Nitrogen oxide (NO) through photocatalytic method [53]. Sulphur doped graphitic carbon nitride was also synthesized from thiourea calcination and then used for carbon dioxide reduction by Ke Wang and group [54]. High efficiency was also reported by Yiming He et al to be achieved in the conversion of carbon dioxide into fuel through the application of ZnO/g-C_3N_4 [55].

Also, several nanoparticles of noble metals have been incorporated as dopants on graphitic carbon nitride to reduce the electron-hole recombination effect through surface plasmon resonance. Surface plasmon resonance effect of noble metal nanoparticles can be ascribed to the accumulative oscillation of free conducting electrons which are energized by interacting electromagnetic field [27]; and the hot electrons have been reported to be injected onto the conduction band of the photocatalyst over schottky barrier (metal-semiconductor junction) [26]. These noble metal nanoparticles can effectively absorb visible light due to their surface plasmon resonance (SPR), which can be tailored and controlled by their shape, particle size and environment. Several metal nanoparticles have been applied to improve graphitic carbon nitride through surface plasmon resonance effect [27]. Yuanguo Xu et al designed and fabricated plasmonic Ag/AgBr/g-C_3N_4 catalyst through solvothermal method, which displays enhanced photocatalytic performance on g-C_3N_4 owing to the high dispersion of Ag/AgBr on the surface of it [7]. Lichan Chen et al prepared gold nanoparticle graphite-like C_3N_4 nanosheet nanohybrid for application in electrochemiluminiscent immunosensor (ECL); and it was shown that there was highly stable and strong display of cathodic ECL reactivity in comparison to pure g-C_3N_4, owing to significant roles of Au nanoparticles trapping electrons from the conduction band of g-C_3N_4 as well as preventing rapid recombination of elctrons [56]. Shouwei Zhang et al synthesized plasmonic

Ag/AgCl/g-C_3N_4 photocatalyst by an ion exchange approach on g-C_3N_4 sheet; and an enhanced performance under visible light was reported on rhodamine B degradation due to integration of synergetic effect of suitable size plasmonic Ag/AgCl and strong coupling effect between Ag/AgCl and g-C_3N_4 sheet [57]. Subhajyoti Samantha et al deposited gold nanoparticles on g-C_3N_4 sheet by facial deposition forming a plasmon photocatalyst, and reported enhanced photoactivity of the polymer by application on hydrogen production under visible light irradiation [58]. Yuyu Bu et al applied electrochemical methods in investigating photoconvertion of plasmonic Ag/ mg-C_3N_4 (mesoporous g-C_3N_4) [59]. Other applications of plasmon catalyst were reported such as g-C_3N_4/Ag/TiO_2 [60], Pt/g-C_3N_4 [61], and g-C_3N_4/Ag_2O [62].

In countries with quite a large amount of sunlight like Saudi Arabia, photocatalytic method to solve environmental issue in degrading organic pollutant from wastewater, should be invested in and properly exploited. In this study, the different approaches of preparing and synthesizing graphitic carbon nitride (g-C_3N_4) based nano structured composites discussed above will be properly probed and investigated.

CHAPTER 3

EXPERIMENTAL METHODS, CHARACTERIZATION TECHNIQUES AND APPLICATION PROCEDURE

In this chapter, all experimental details as regards synthesis of different catalysts through different methods such as facile preparation, hydrothermal and photodeposition are discussed. Furthermore, characterization techniques to analyse the identities of synthesized catalysts are discussed; and application procedure (photodegradation) to evaluate their efficiencies is properly explained in details.

3.1 Synthesis of Composite Catalysts

3.1.1 Synthesis of g-C_3N_4

Fig 3.1 displays graphitic nitride, which is an attractive earth-rich visible light photocatalyst, with a distinct 2-dimensional structure, with high chemical and thermal stability and tunable electronic and optical properties [63]. It can be synthesized in a single step polymerization and direct condensation of economical organic nitrogen-rich precursors such as cyanamide, dicyandiamide, melamine, thiourea, urea; mostly with surface area less than 10 m^2/g [63].

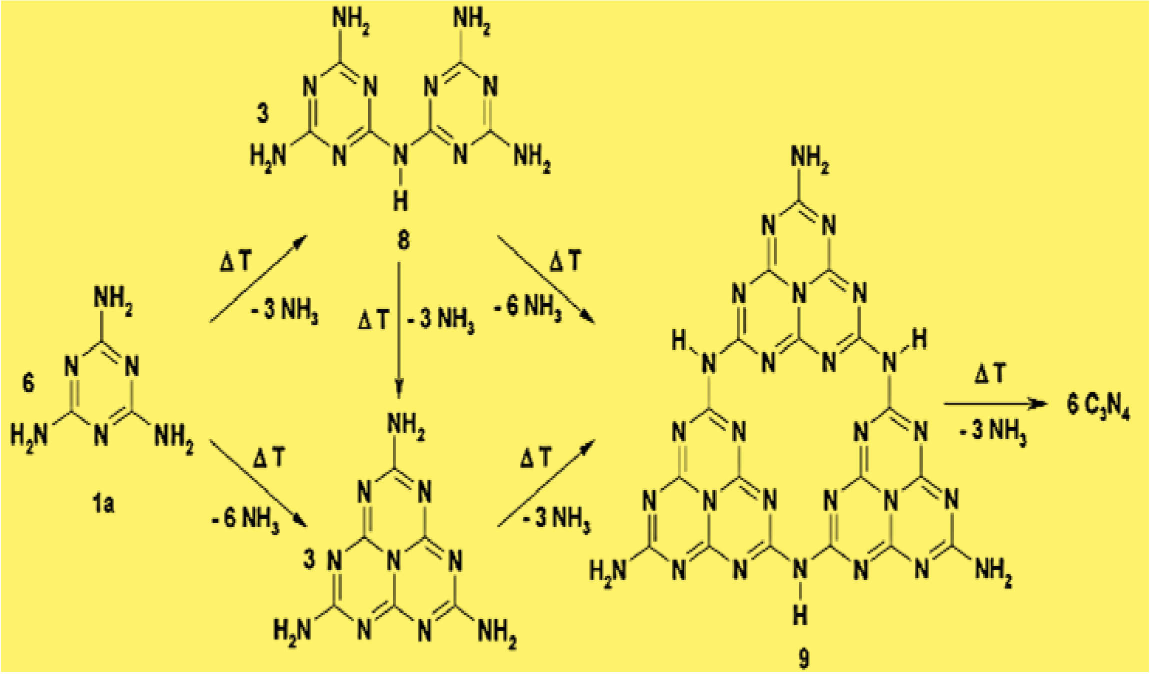

Fig 3.1 Reaction route from melamine to graphitic carbon nitrtide

In this research, melamine was chosen as precursor to directly synthesize graphitic carbon nitride by pyrolysis. Melamine is a three triazine heterocyclic organic compound, which displays a white monoclinic crystal at room temperature with no unique odour among other properties [64]. Hence, graphitic carbon nitride consists of several melem units stacked in an interlayered structure as displayed in fig 3.1.

Pyrolysis of melamine for two hours at 500˚C and further deamination for 2hrs at 550 ˚C at heating rate of 2.2 ◦C min^{-1} yields g-C_3N_4 according to the reaction route displayed in fig. 3.1.

3.1.2 Synthesis of $WO_3/g\text{-}C_3N_4$

The pure $g\text{-}C_3N_4$ was prepared by directly pyrolysis of melamine at 500˚C for 2 h, and further deamination treatment was carried out at 550 ˚C for 2 h [25, 26] as illustrated in the flowchart in fig 3.2. A series of $WO_{3(x)}/g\text{-}C_3N_{4(1\text{-}x)}$ composite photocatalysts (‘‘x’’ denotes the mass ratio of WO_3 in the corresponding composite) were prepared through direct heating of $H_2WO_4/g\text{-}C_3N_4$ composites (prepared by grinding for 5 min) at 300˚C.

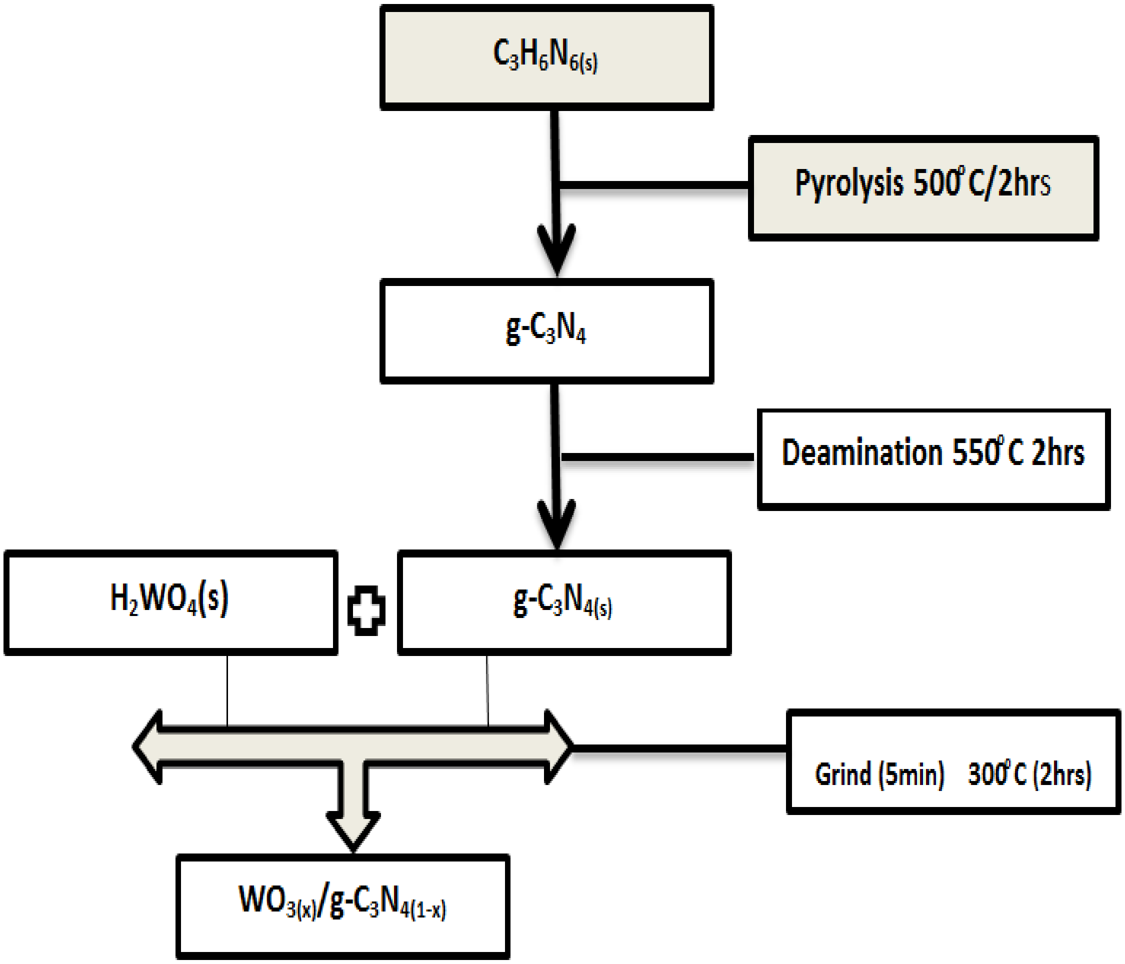

Figure 3.2 Schematic flowchart displaying synthesis steps for as-prepared composite $WO_3(x)/g\text{-}C_3N_4(1\text{-}x)$

X(WO_3) %	**Samples**
0	**g-C_3N_4**
10	**WO_3(0.1) /g-C_3N_4(0.9)**
20	**WO_3(0.2) /g-C_3N_4(0.8)**
50	**WO_3(0.5) /g-C_3N_4(0.5)**
80	**WO_3(0.8) /g-C_3N_4(0.2)**
90	**WO_3(0.9) /g-C_3N_4(0.1)**
100	**WO_3**

Table 1 Different mass ratios of WO_3(x)/g-C_3N_4(1-x) as-prepared composite

3.1.3 Synthesis of Au/Ag/g-C_3N_4

As detailed below in fig 3.3, the modified Turkevich method was adopted for depositing different compositions of Au-Ag alloy NPs at the surface of g-C_3N_4 [28]. In Au-Ag alloy loaded g-C_3N_4 photocatalysts, and the proportion of Ag was fixed at 1%, whereas the amount of Au was varied as 0.5%, 1% and 3% with respect to the weight of g-C_3N_4. The required amounts of 0.01M $HAuCl_4.3H_2O$ and 0.01M $AgNO_3$ precursor solutions were mixed and boiled under vigorous stirring (400-600 rmp). Then 1 ml of freshly prepared sodium citrate was added and boiled for 30 min which lead to the formation of the Au-Ag colloidal NPs solution. The appropriate amount of g-C_3N_4 was dispersed in colloidal Au-Ag NPs solution ultrasonically. The dispersion of Au-Ag NPs and g-C_3N_4 was subjected to UV light exposure for photo-impregnation process under vigorous stirring for 30 min. A 450 W Xenon arc lamp equipped with UV band pass filter, Oriel, USA was used as the UV source. The slurry was filtered, washed and dried overnight at 110ºC under vacuum. The same protocol was adopted for the synthesis of 1%Ag and 1%Au loaded g-C_3N_4.

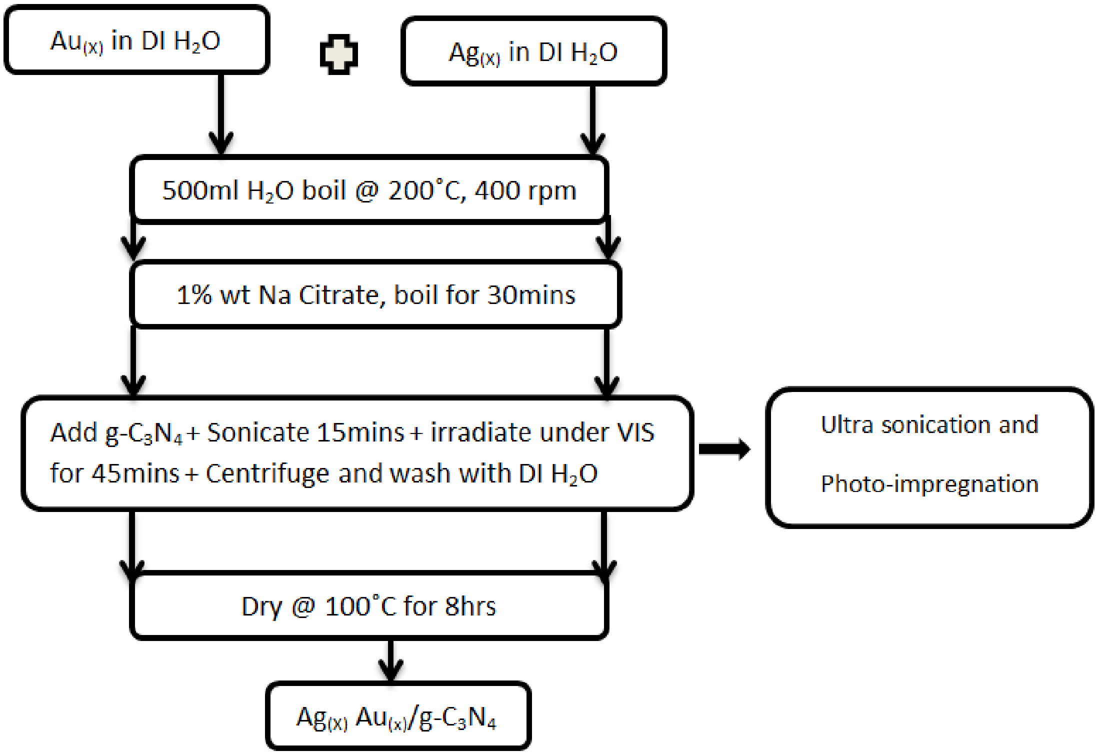

Figure 3.3 Schematic flowchart displaying synthesis steps for as-prepared composite Au/Ag/g-C_3N_4

3.2 Characterization techniques

3.2.1 X-Ray Diffraction Analysis

The crystal structure of synthesized catalysts was investigated and studied with wide angle X-ray diffractometer (Bruker Advance D8, Philips X’ Pert PRO 3040/60) equipped with Cu-Kα radiation source within the range of $2\theta = 10^{\circ}$ to $2\theta = 90^{\circ}$ range.

3.2.2 Field Emission Scanning Electron Microscope (FESEM)

FESEM is a characterization technique applied to probe the microstructural properties of materials. The fundamental steps for imaging of a sample include formation of an electron beam, interaction between sample and beam, gathering information of the sample and formation of an image. The incident electron beam (about 20KV) hits the surface of the sample and strikes on it, which then yields various photons and electron signals generated after the interaction.

The microstructure and morphology of prepared samples were examined with Field emission scanning electron microscopy (FESEM, Tescan Lyra-3).

3.2.3 High Resolution Transmission Electron Microscope (HR-TEM)

To analyze the fine structure of the synthesized powders, transmission electron microscopy (TEM), JEM2100F, JEOL at 200KV was applied. The steps highlighted above for FESEM are as well applicable here but on a fine scale and at higher voltage of electron beam.

3.2.4 UV-Vis Spectrophotometry

A JASCO, V-670, UV-Vis-NIR spectrophotometer was used for recording the solid-state absorption and diffused reflectance spectra (DRS) of the synthesized catalysts using pure Barium Sulphate pellet as a reference. The measurements were carried out within the wavelength range (200-800) nm and under atmospheric conditions.

3.2.5 Photoluminiscence

The photoluminescence emission spectra were measured on a spectroflourometer (Horiba Jobin–Yvon) using the Xenon lamp as a source of excitation. All the samples were excited at 380 nm and the emission spectrum recorded in the range of 400–700 nm. This demonstrates and displays the electron emission intensity of the prepared materials.

3.2.6 X-Ray Photoelectron Spectroscopy (XPS)

This is a surface-specific characterization tool, which is applied to ascertain the chemical environment and elemental oxidation state of a material. The XPS profile of prepared samples was acquired by a wide survey scan using X-ray Photoelectron Spectrometer (PHI 5000 Versa Probe II, ULVAC-PHI Inc.). The binding energy was varied between 0 eV to 1100 eV. The oxidation states of the metallic components were evaluated by comparing the obtained binding energy values with that of standard values. Gaussian model was applied for curve fitting and the identification of the number and precise binding energy of each state.

3.2.7 Total Organic Carbon

The mineralization progress was monitored by measuring the total organic carbon (TOC) of the samples by using TOC-VCPH total carbon analyzer supplied by Shimadzu Corporation, Japan. The experiments were performed at 25 ±1°C.

3.3 Photocatalytic Experiments

The photocatalytic performance of the synthesized photocatalysts was evaluated for the degradation (decolorization/mineralization) of Rhodamine B (10 ppm) in 200ml cylindrical glass reactor made up of Pyrex® glass. A 450-W Xe arc lamp (Oriel, USA) equipped with UV cut off filter was used as excitation source. The experiments were performed in batches. Prior to photocatalytic studies, the dark experiments were performed to establish the adsorption-desorption equilibrium between the dye and catalysts. In a typical photocatalytic experiment in visible light exposure, 100 ml of dye/catalyst suspension containing, 100 mg of the respective catalyst, was exposed to visible light (420-800nm) for 240 min under stirring. The samples (5 ml each) were drawn from the reactor after every 15 min in the initial 60 min, after every 30 min in the next hour and after 60 min in the final 120 min. After centrifuging at 4000 rpm for the removal of catalyst, the progress of the decolorization process was monitored using UV Visible spectroscopy. A JASCO 570 UV-Vis spectrophotometer was employed to record the absorption spectra of the exposed samples..

CHAPTER 4

RESULTS AND DISCUSSION

4.1 Preparation of WO_3/g-C_3N_4 composites and their enhanced photodegradation of contaminants in aqueous solution under visible light irradiation

4.1.1 Introduction

Sunlight power is natural, and quite simple energy that is tapped from the radiations of the sun. The sun is continuously radiating an enormous amount of solar energy.Various innovative ways have been developed by modern technologist to convert solar energy into electrical and chemical energies. Since its first report in 1972 [11], photocatalysis has become a promising technology to solve energy and environmental problems. TiO_2 has been widely used as a popular photocatalyst due to its various advantages such as unique optical and electronic properties, low cost, chemical stability, non-toxicity, and superior photocatalytic activity. However, its large band gap (3.2 eV) restricts efficient absorption of visible light, which is around 42 % of the total light spectrum of the solar radiations [65, 66]. The concept of ‘‘low-carbon and green life’’ as well as the pioneer achievements are inspiring a great enthusiasm to develop highly efficient photocatalysts to improve the quantum efficiency under visible light (380–780 nm). In the past 13 years, a great deal of effort have been put into the investigation of searching and developing novel photocatalysts which can be driven by visible light [67-73]. In early 2009, g-C_3N_4 was first reported as a visible-light response photocatalyst by Wang and co-workers, which was used for H_2 production from water splitting with triethanolamine as a sacrificial electron donor under visible light exposure [74].

Quickly thereafter, in order to overcome the disadvantages of g-C_3N_4 (such as the high recombination rate of the photogenerated charge carriers), numbers of g-C_3N_4 based composite photocatalysts have been extensively reported, such as g-C_3N_4/TiO_2 [44, 45], Ag_3PO_4/g-C_3N_4 [18], g-C_3N_4/SiO_2-HNb_3O_8 [75], g-C_3N_4/TaON [76], g-C_3N_4/ZnO [42], g-C_3N_4/$BiPO_4$ [77], Ag/Ag_3PO_4/g-C_3N_4[78], g-C_3N_4/Bi_2WO_6 [41] and BiOCl- g-C_3N_4 [40]. The present investigation deals with a facile preparation of a series of novel WO_3/g-C_3N_4 composite photocatalysts and their enhanced photoactivity driven by visible light. WO_3 has a narrow band gap (2.7–2.8 eV) and has been applied for photocatalysts due to its outstanding properties. It was found clearly that the photoactivity of WO_3 could be enhanced apparently through combining with g-C_3N_4 with lower photodegradation performance for methylene blue, acetaldehyde gas degradation, and O_2 evolution. [45, 49, 79]. This investigation provides the photocatalytic enhancement for RhB and methyl tert butyl ether (MTBE) degradation. The synergetic effect of the composite could be attributed to the heterojunction-like structure generated at the interface between g-C_3N_4 and WO_3.

Experimental

4.1.2 Chemicals and reagents

All chemicals used in this study were of reagent grade and applied without further purification. Deionized water was used in the present work. Melamine ($C_3H_6N_6$, CP) and tungstic acid (H_2WO_4, AR) was purchased from Tianjin China Chemical Reagent Ltd and Sigma-Aldrich, respectively. Typical contaminants of Rhodamine B and MTBE were purchased from LAMBDA PKYSIK and Fluka. Photocatalysts of TiO_2 (product name P25) was commercially supported by Degussa Corp, and Fe_2O_3 was prepared by the pyrolysis of $Fe(NO_3)_3$ (Sinopharm) at 500˚C for 2 h. Nitrogen doped TiO_2 nanoparticles was prepared through mixture with of TiO_2 powders with aqueous solution of organic nitrogen and stirred at room temperature [80].

4.1.3 Material preparation

The pure g-C_3N_4 was prepared by directly pyrolysis of melamine at 500˚C for 2 h, and further deamination treatment was carried out at 550˚C for 2 h [81, 82].

The composites, WO_3/g-C_3N_4, were prepared by a simple method by mixing of series of H_2WO_4 and g-C_3N_4 in a composite photocatalysts (‘‘x’’ denotes the mass ratio of WO_3 in the corresponding composite) by grinding certain amounts (depending on "X” value) for 5 min in a mortar. The homogenously mixed precursors was then subjected to direct heating at 300˚C for 2 hours.

4.1.4 Characterization and optical property

The crystal structure of the samples was investigated by X-ray diffraction analysis (XRD, Bruker Advance D8) with Cu Ka radiation. The UV–Vis diffused reflectance spectra (DRS) were measured on JASCO V-670 UV–Vis-NIR spectrophotometer and pure $BaSO_4$ pellet was employed as a reference. The photoluminescence emission spectra were measured on a spectroflourometer (Horiba Jobin–Yvon) using the Xenon lamp as a source of excitation. All the samples were excited at 380 nm and the emission spectrum recorded in the range of 400–700 nm.

4.1.5 Photocatalytic experiments

The photodegradation performance of different model compounds onto assynthesized WO_3/g-C_3N_4 composite photocatalysts was conducted under a 500W Xenon lamp (Oriel, USA) equipped with visible light filter. In a typical photodegradation experiment, 50mg of photocatalyst was mixed with a contaminant solution with known initial concentration and volume. Under visible light exposure, the suspensions were collected and centrifuged (4,000 rpm, 2 min) to remove the photocatalyst particles at regular time intervals. The concentration of RhB and MTBE was detected by means of UV–Vis spectroscopy (JASCO V-670) and GC-FID analysis [83, 84].

4.1.6 Results and discussion

Fig 4.1 depicts the XRD patterns of the synthesized WO_3/g-C_3N_4 composite photocatalysts with different mass ratios of WO_3 to g-C_3N_4. All the apparent diffraction peaks can be indexed as cubic phase of WO_3 and the diffraction data are in good agreement with JCPDS files #41-0905. Moreover, the second minor phase in the XRD patterns, a diffraction peak with low intensity at around 27.4˚ in the XRD patterns, can be attributed to the 002 plane in g-C_3N_4. When the combination ratio of WO_3 to g-C_3N_4 is more than 0.5, it was observed that the (002) diffraction peaks of g-C_3N_4 particles were masked in the patterns of WO_3/g-C_3N_4 due to its strong interference with the WO_3 diffraction signals.

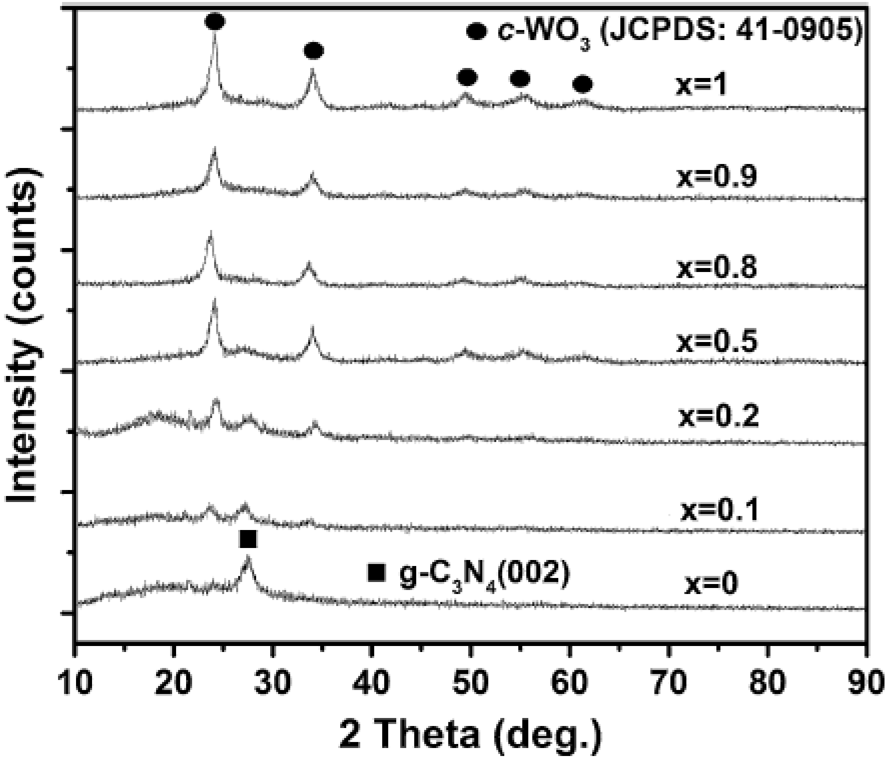

Figure 4.1 XRD patterns of the as-prepared $WO_3(x)/g\text{-}C_3N_4(1\text{-}x)$ (x=0-1) samples

Diffuse reflection spectroscopy was employed to investigate the optical absorption of the synthesized $WO_3/g\text{-}C_3N_4$ composite photocatalysts (as depicted in Fig.4.2a). The optical absorption near the band edge for a crystalline semiconductor can be described by the following equation,

$ahv = K (hv - Eg)^n$

where a, h, v, K and Eg are absorption coefficient, Plank constant, light frequency, proportionality constant, and band gap, respectively. The exponent n depends on the nature of transition: n = 0.5, for allowed direct transitions (k = 0); n = 1.5, for forbidden direct transitions (k = 0); n = 2, for allowed indirect transitions; and n = 3, for forbidden indirect transitions. The values of n was determined by plotting log(ahv) versus log(hv - Eg), and then using the approximate Eg values of 2.6 eV(WO_3) and 2.7 eV($g\text{-}C_3N_4$), followed by determining the slope of the straightest line near the band edge. As depicted in Fig.4.2b, the values of n for WO_3 and g-C_3N_4 are found at 0.5 and 2, and these indicate the allowed direct transition and allowed indirect transition in WO_3 and g-C_3N_4, respectively. A classical Tauc's approach is employed to evaluate the band gap values of synthesized WO_3 and g-C_3N_4, as given in Fig. 4.2c and Fig. 4.2d respectively. The extrapolated absorption edge energies values were at 2.5 and 2.8 eV corresponding to WO_3 and g-C_3N_4, respectively [49, 79].

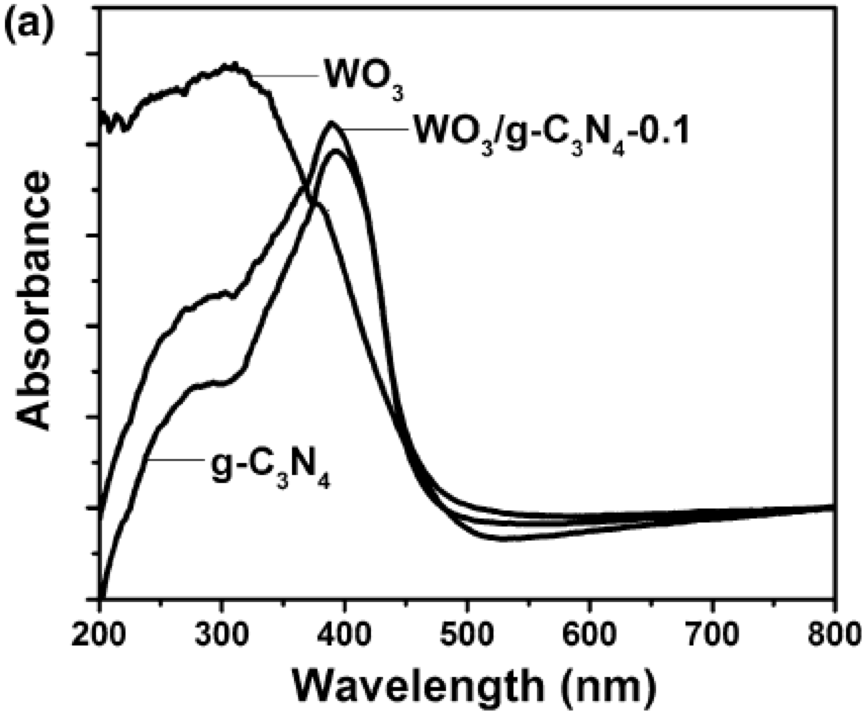

Figure 4.2 (a) UV-Vis absorption spectra of WO_3, g-C_3N_4 and WO_3/g-C_3N_4-0.1

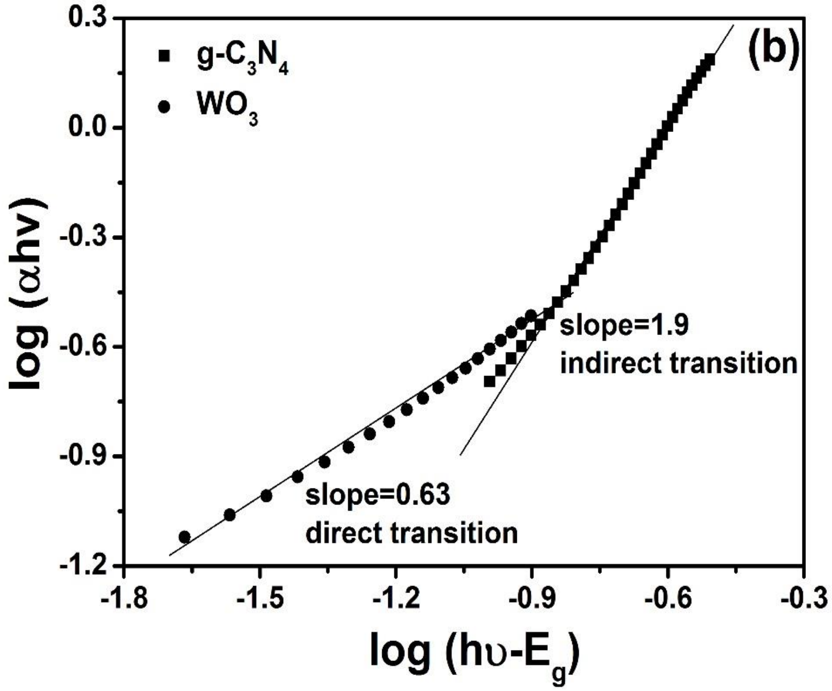

Figure 4.2 (b) optical transition type determination of WO_3 and g-C_3N_4

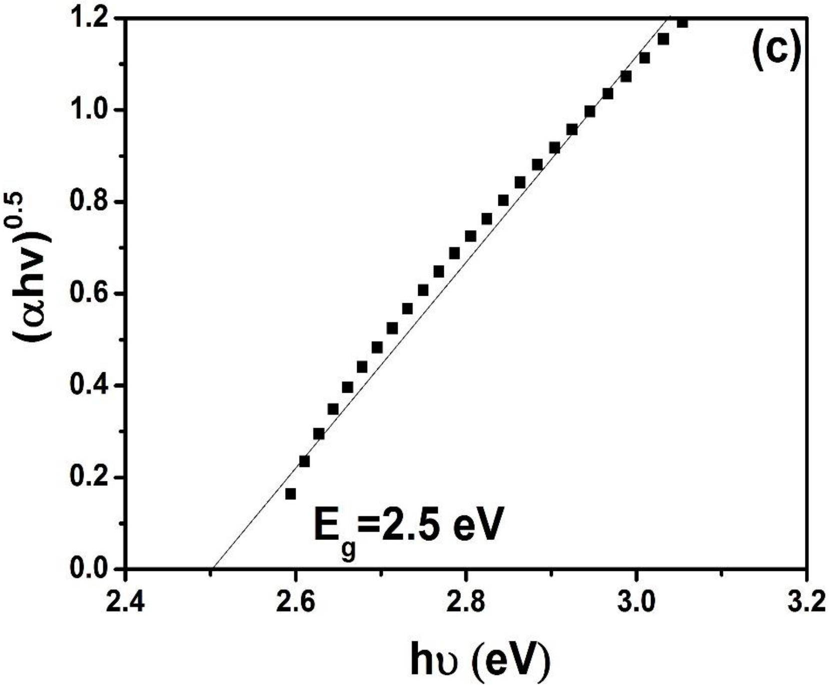

Figure 4.2 (c) band gap determination of WO_3 by Tauc's approach

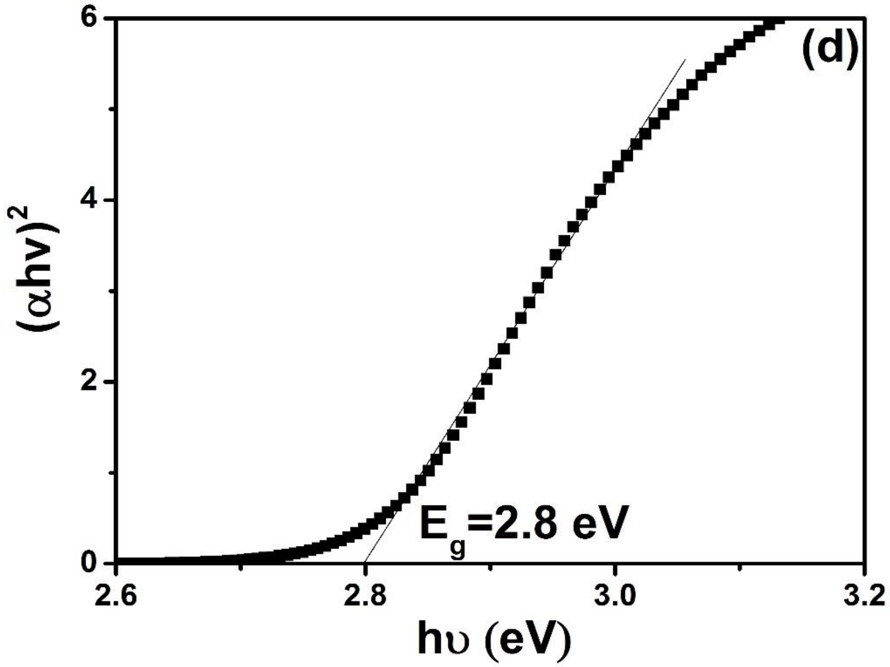

Figure 4.2 (d) band gap determination of g-C_3N_4 by Tauc's approach

No apparent visible light absorption improvement was observed in WO_3/g-C_3N_4 composite because of almost similar band gap values of both components. However, it was found that such coupling could remarkably affect the transfer and lifetime of the photogenerated charge carriers in g-C_3N_4. As depicted in Fig.4.3, a strong emission band centered at 450 nm in g-C_3N_4 can be assigned to the band–band emission of g-C_3N_4 as the energy of the emitted light is identical to its band gap energy. However, the PL emission intensity decreases by *30 % as compared with the pure g-C_3N_4 after coupling with 10 % of WO_3, which is attributed to the transfer of the photogenerated carriers at the interface between WO_3 and g-C_3N_4.

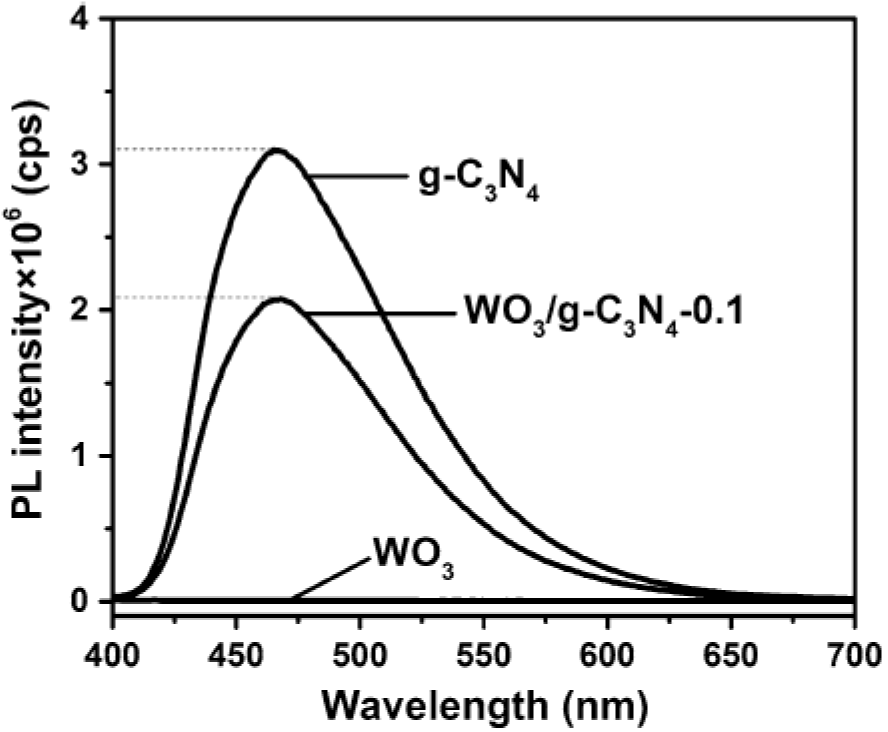

Figure 4.3 PL emission spectra of WO_3, g-C_3N_4 and WO_3/g-C_3N_4-0.1

The photodegradation improvement onto WO_3/g-C_3N_4 composites was evaluated under visible light exposure, using RhB as the model contaminant. Fig.4.4 shows the changes in RhB concentration onto g-C_3N_4, WO_3 and their composites with different mass ratios as a function of irradiation time. Photodegradation results showed fast degradation rate in the first 20 min and later it slowed down with a further increase in the irradiation time, which is typical reaction kinetics for photocatalytic process [85]. Almost all WO_3/g-C_3N_4 composite compositions exhibited higher photocatalytic activity than either pure WO_3 or g-C_3N_4. When the mass amount of WO_3 was 0.1g in the composite, the synthesized photocatalyst exhibited the highest photocatalytic activity and 62 % degradation of RhB was achieved in 90 min under visible light irradiation, while pristine WO_3 and g-C_3N_4 only showed 42 and 27 % degradations under the same conditions, respectively. The photocatalytic activity gradually reduced with the further increase in combination ratio of

WO_3 from 0.1 to 0.9. This could be due to the agglomeration of WO_3 particles on the pure g-C_3N_4. The agglomeration of WO_3 particles on the surface of the semiconductors could decrease the separation efficiency of photo-induced electron–hole pairs and thus affect the catalytic activity [86, 87].

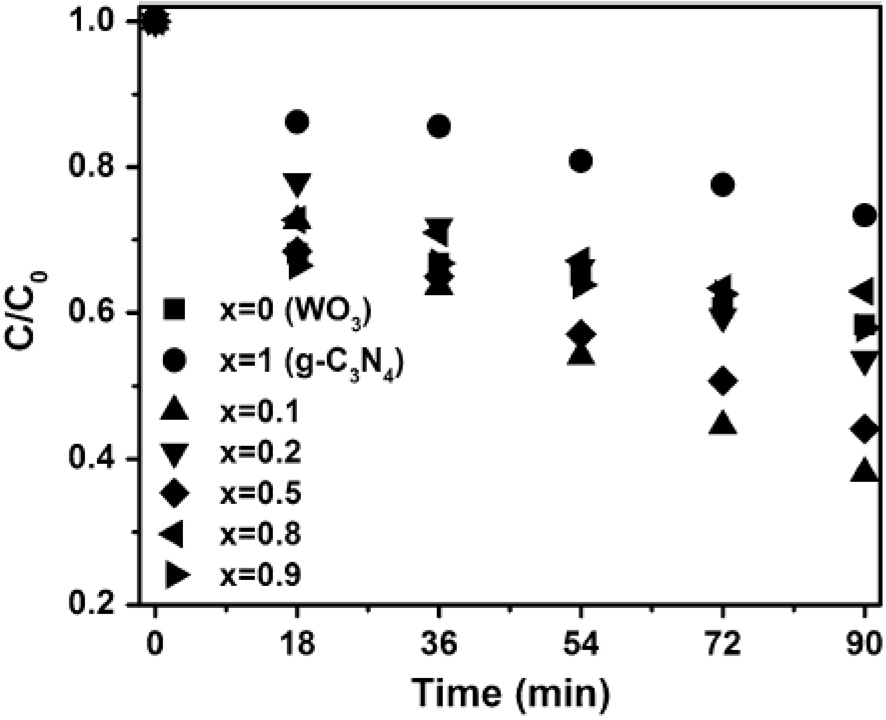

Figure 4.4 Changes of RhB concentration onto WO_3/g-C_3N_4-x (x = 0–1) composite photocatalysts under visible light irradiation as a function of irradiation time. Experimental conditions: catalyst dosage = 50 mg, volume of solution = 100 mL, initial concentration = 7 mg L^{-1}

Fig 4.5 shows the linear relationship between Ln(C/C0) and irradiation time during the photocatalytic reaction. The degradation of RhB over g-C_3N_4, WO_3 and WO_3/g-C_3N_4 composite showed apparent first order kinetics of the Langmuir Hinshelwood model [85]. The highest reaction rate constant (k) was found at 0.0108 min^{-1} for WO_3/g-C_3N_4-0.1, however, the k values for pure phase of g-C_3N_4 and WO_3 were only around 0.0032 and 0.0049 min^{-1}, respectively.

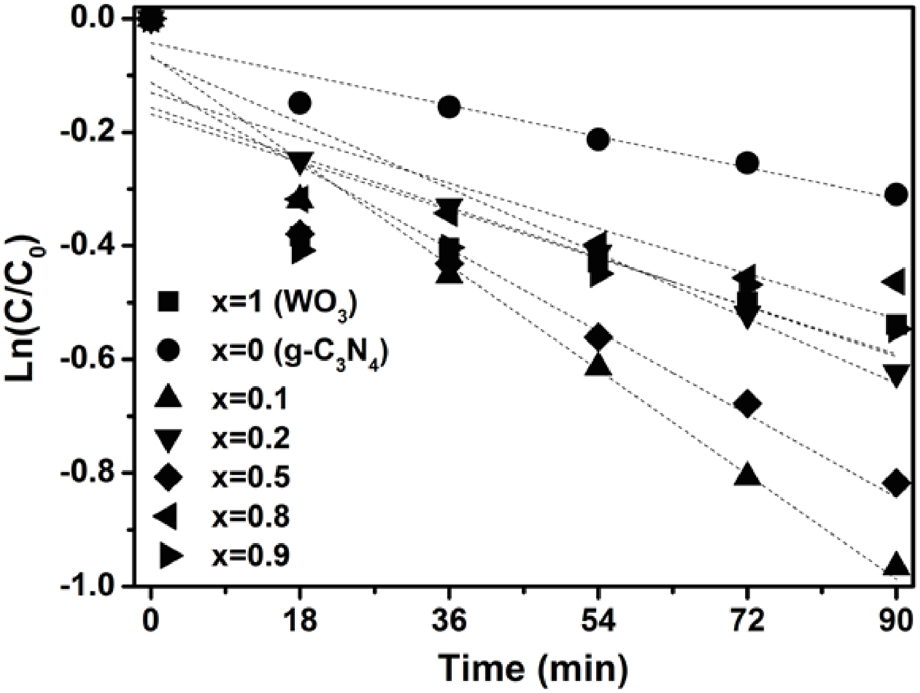

Figure 4.5. First-order plots for the photocatalytic degradation over WO_3/g-C_3N_4-x (x=0~1). Experimental conditions: catalyst dosage= 50 mg, volume of solution = 100 mL, initial concentration of RhB = 8.5 mg L^{-1}

The time-dependent UV–Vis spectral changes of RhB solution in the presence of WO_3, g-C_3N_4 and WO_3/g-C_3N_4-0.1 composite photocatalyst are depicted in Fig 4.6 (a-c). For all the composites, the absorbance of the characteristic peak decreased with time, and the wavelength of maximum absorption peak slightly blue shifted, which indicates the N deethylation (removal of nitrogen ethyl arm of RhB structure) mechanism in photochemical reaction[33, 88]. While no such blue shift was observed in maximum absorption peak of RhB when treated with either pristine g-C_3N_4 or WO_3. The possible mechanism in this case could be cleavage of the whole conjugated chromophore structure in RhB instead of N-deethylation mechanism. The maximum absorption peak of RhB solution was blue shifted from 554 to 548 nm after 90 min irradiation in the presence of WO_3/g-

C_3N_4-0.1 composite. However, with further increase in the WO_3 mass amount was not found to be beneficial for N-deethylation process [89].

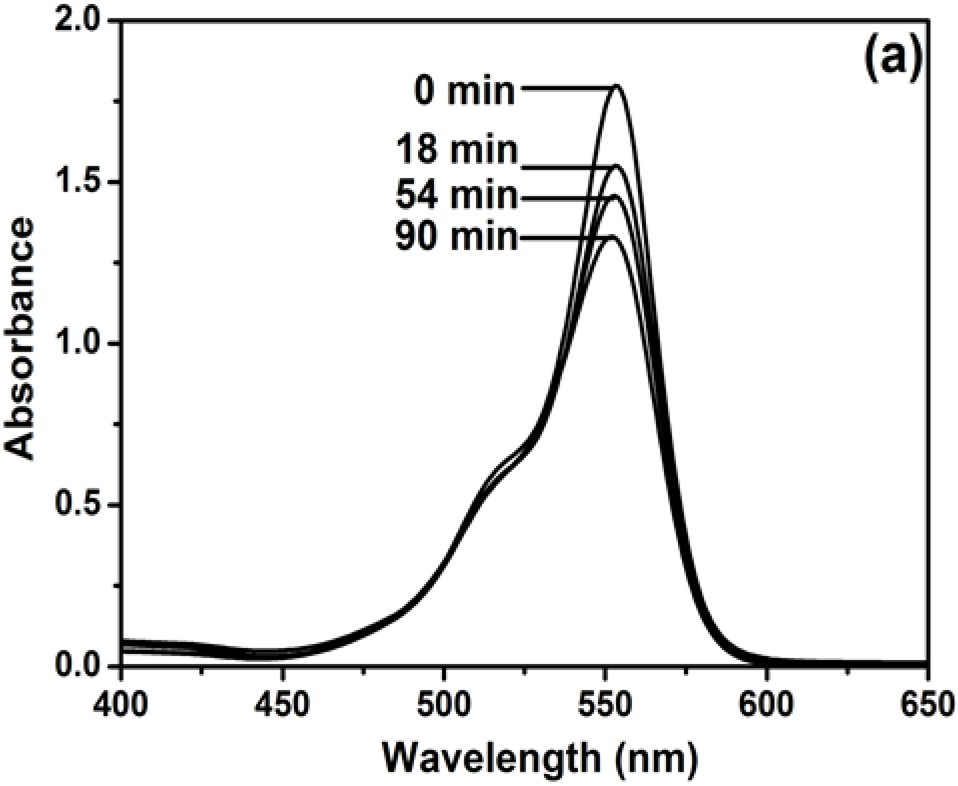

Figure 4.6. (a) Temporal UV-Vis absorption spectral changes of RhB during the photodegradation process by g-C_3N_4

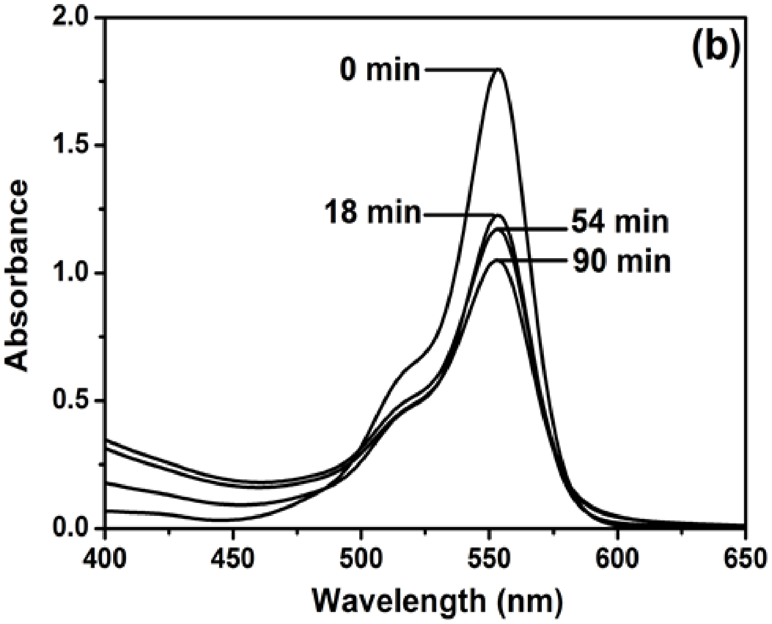

Figure 4.6.(b) Temporal UV-Vis absorption spectral changes of RhB during the photodegradation process by WO_3

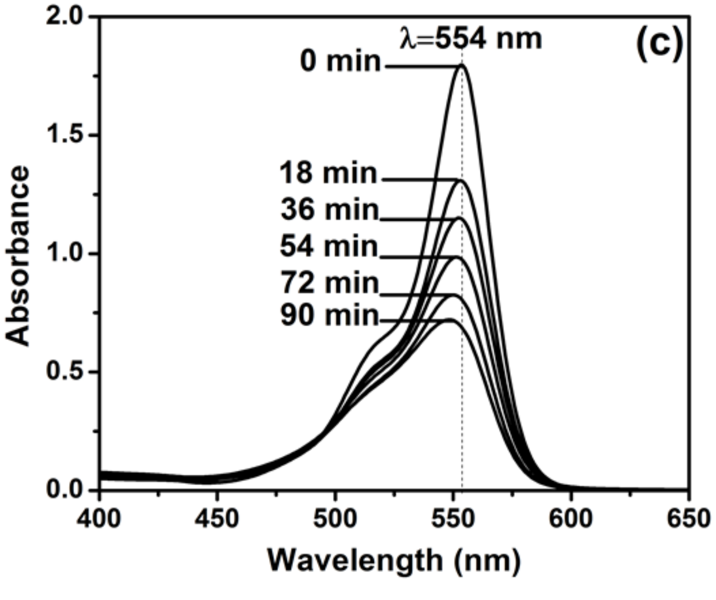

Figure 4.6. (c).Temporal UV-Vis absorption spectral changes of RhB during the photodegradation process by $WO_3/g\text{-}C_3N_4\text{-}0.1$

The changes in constant k and shifts in absorption peak of RhB as a function of mass combination of ‘‘x’’ in $WO_{3(x)}/g\text{-}C_3N_4(_1\text{-}x)$ composites are shown in Fig.4.7**.** The highest reaction rate constant (k = 0.0108 min-1) and the maximum blue shift in absorption peak of RhB solution (from 554nm to 548 nm) were achieved over $WO_{3(x)}/g\text{-}C_3N_4(_1\text{-}x)$ (x=0.1). This suggests the optimal combination ratio of WO_3 to $g\text{-}C_3N_4$ is 0.1 (10 %) for maximum photocatalytic activity.

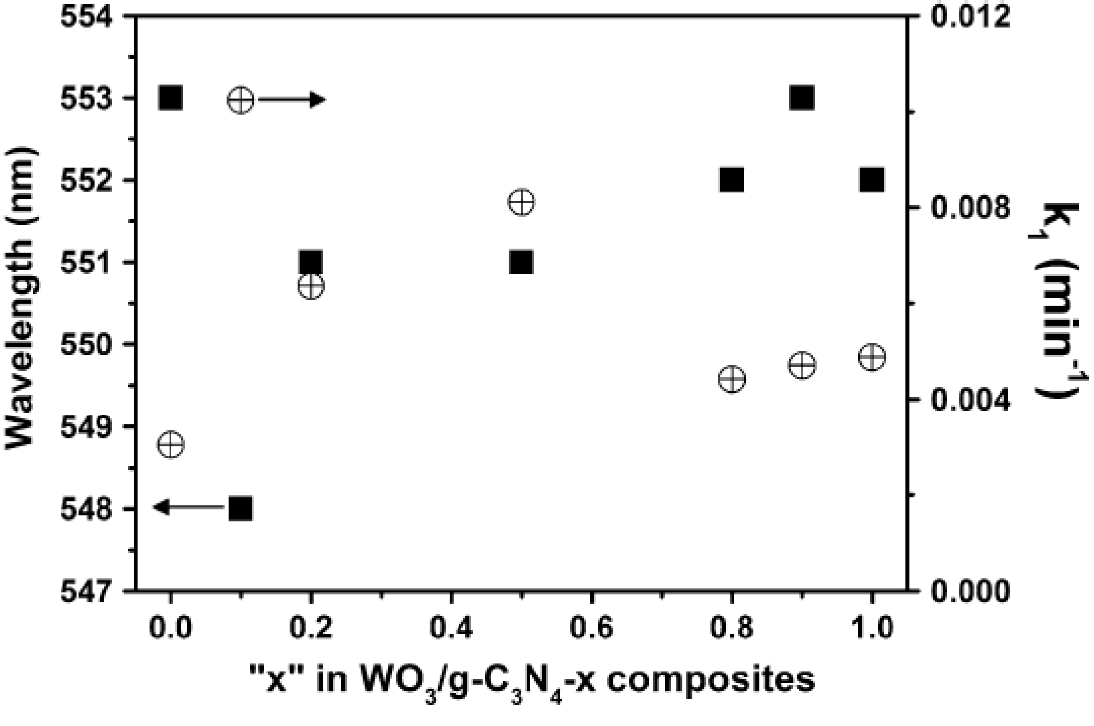

Figure 4.7 Effects of x value in $WO_3/g\text{-}C_3N_4\text{-}x$ composites on the first-order kinetics constants and adsorption peak of RhB solution

The photoactivity and photostability of synthesized $WO_3/g\text{-}C_3N_4\text{-}0.1$ composite after long-term use were also evaluated. As depicted in Fig.4.8, the average reaction rate (ARR) in the first run was 0.21 mg min^{-1} g^{-1}, while after the fifth cycle; it was 0.131 mg min^{-1} g^{-1}. Around 37.6 % decline in ARR was found after five runs, possibly due to the effect of catalyst fouling. However, XRD results showed that the crystal phase of the composite photocatalyst was well retained even after 5 runs, as shown in the inset of Fig 4.8. This retainability in crystal structure demonstrates the stability of the catalyst for photodegradation process.

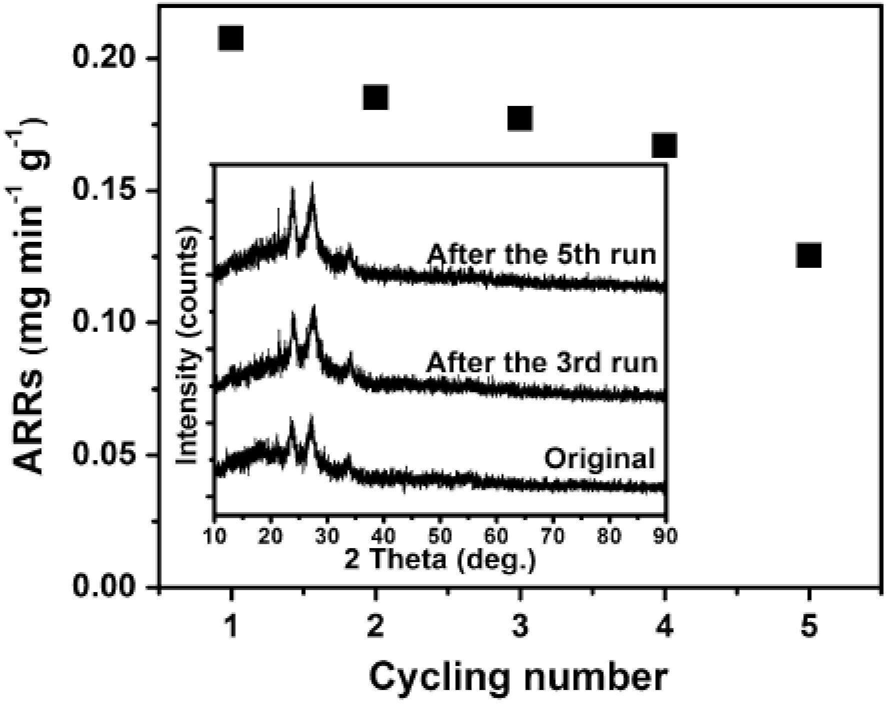

Figure 4.8 Changes of ARRs of RhB decomposition on WO_3/g-C_3N_4-0.1 over five successive photodegradation cycles. Inset figure shows the XRD patterns of WO_3/g-C_3N_4-0.1 before and after the 3rd and 5th cycling photocatalytic experiments. Experimental conditions: catalyst dosage = 50 mg, volume of solution = 100 mL, initial concentration of RhB = 8.5 mg L-1, reaction time for each cycling = 20 min

Compared to various popular photocatalysis systems, the synthesized $WO_{3(x)}$/g-$C_3N_4(_1$-x) (x=0.1) composite photocatalyst exhibits superior performance. A comparison in average reaction rates (ARRs) of synthesized on $WO_{3(x)}$/g-$C_3N_4(_1$-x) (x=0.1) and various popular photocatalytic systems is shown in Fig 4.9 (a). WO_3/g-C_3N_4-0.1 showed maximum ARR of 0.44 mg min^{-1} g^{-1} within 54 min, while the observed ARR values for P25 (standard titanium oxide), Fe_2O_3, g-C_3N_4, TiON and WO_3 were around 0.04, 0.04, 0.13, 0.15 and 0.34 mg min^{-1} g^{-1}. The visible light induced photodegradation of RhB on TiO_2 (or P25) with wide band gap could be attributed to the photosensitization process [78, 90]. Furthermore, the much higher density of synthesized hybrid photocatalyst makes it more convenient to separate from aqueous phase for further regeneration and reuse, compared with the commercialized photocatalyst of P25. The photodegradation of various dyes on WO_3/g-C_3N_4-0.1 was also investigated under visible light irradiations, and the results are shown in Fig.4.9 (b). It was noticed that all the Rhodamine dyes were decomposed to different extent, and higher photodegradation performance was observed with anionic dye (Methylene blue) on the synthesized $WO_{3(x)}$/g-C_3N_4($_1$-x) (x=0.1) composite.

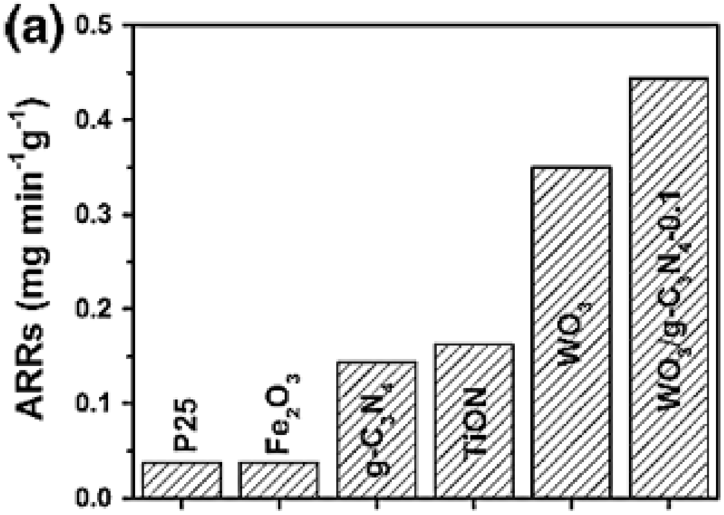

Figure 4.9(a) Comparison of photodegradation of RhB onto various photocatalysts. Experimental conditions: catalyst dosage = 50 mg, volume of solution = 100 mL, initial concentration of dye of 8.5 mg L^{-1} in a and 0.02 mmol L^{-1} in b, reaction time of 54 min in a and 20 min in b

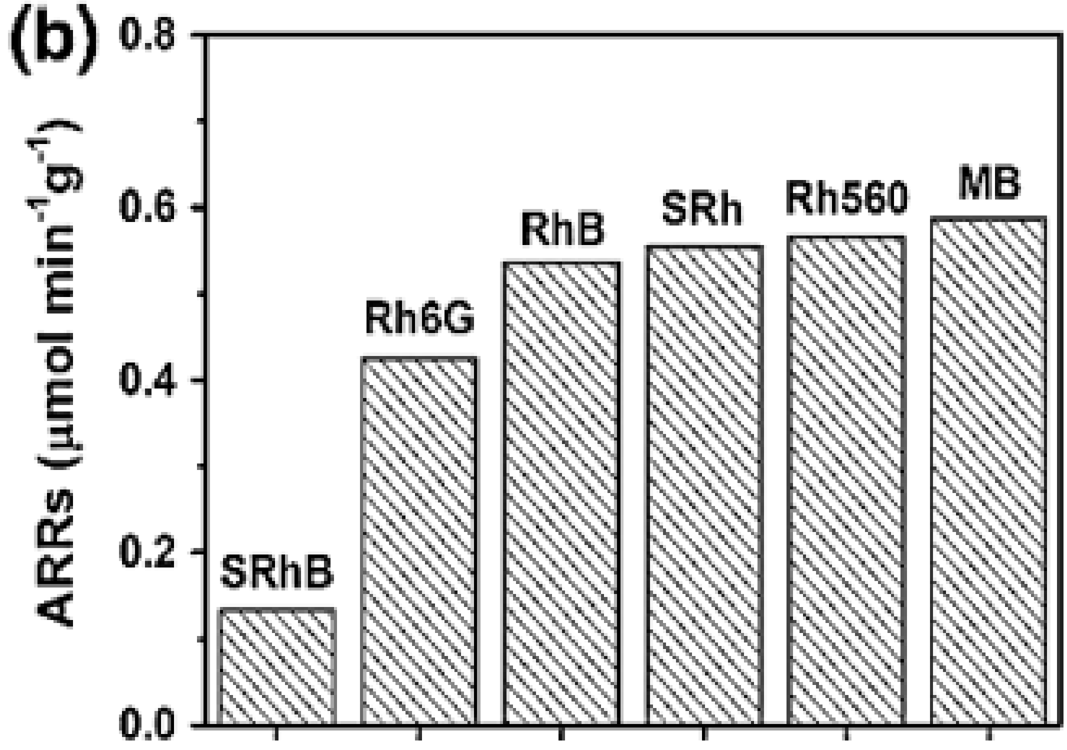

Figure 4.9(b) photodegradation of various dye contaminants over WO_3/g-C_3N_4-0.1 composite photocatalyst. Experimental conditions: catalyst dosage = 50 mg, volume of solution = 100 mL, initial concentration of dye of 8.5 mg L^{-1} in a and 0.02 mmol L^{-1} in b, reaction time of 54 min in a and 20 min in b

In order to further demonstrate the enhanced photoactivity onto WO_3/g-C_3N_4 composites, colorless MTBE solution which cannot be excited by visible or even UV light was adopted as a model compound. Fig 4.10 depicts the effect of x value in WO_3/g-C_3N_4-x composites on the photodegradation efficiency of MTBE. The highest degradation efficiency can be obtained at 96.7 % for WO_3/g-C_3N_4-0.2. However, under identical operation conditions, only 65.9 and 45.3 % of degradation efficiency can be achieved on pure phase of WO_3 and g-C_3N_4, respectively.

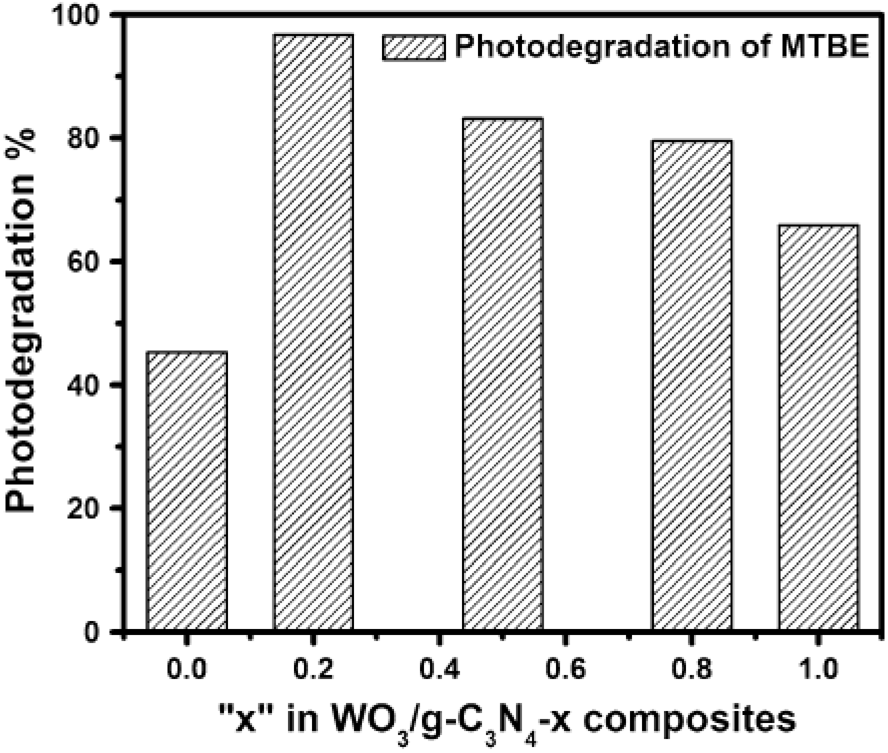

Figure 4.10 Effect of "x" value in WO$_3$/g-C$_3$N$_4$-x composites on the photodegradation efficiency of MTBE (initial concentration of MTBE = 60 mg L-1, volume = 100 mL, dosage = 0.1 g)

The photoactivity improvement can only be explained by the formation of a unique heterojunction-like interfacial structure between g-C$_3$N$_4$ and WO$_3$ semiconductors (as illustrated in Fig 4.11). Under visible light exposure, both g-C$_3$N$_4$ and WO$_3$ can be excited because the band gaps of both lies within visible region. It is reported that the conduction band edges of g-C$_3$N$_4$ and WO$_3$ are at around -1.1 and 0.5 eV (vs. NHE) [49, 79], respectively. Thus photo-excited electrons from the conduction band (CB) of g-C$_3$N$_4$ would inject into CB of WO$_3$ due to the favoring over potential between the CB edges of g-C$_3$N$_4$ and WO$_3$ as portrayed in Fig 4.11**.**

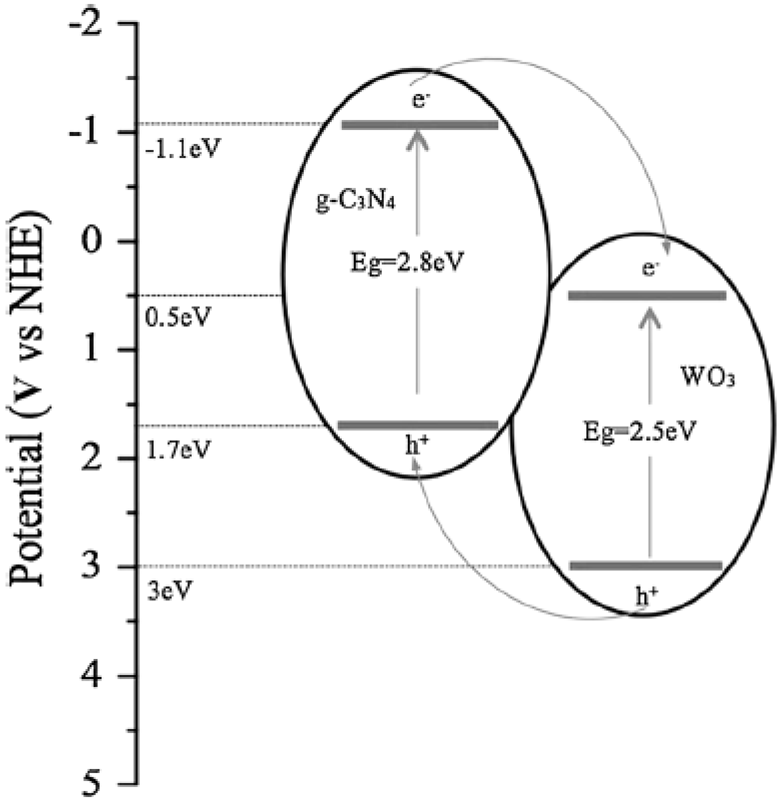

Figure 4.11 Possible mechanism of photoactivity enhancement onto WO_3/g-C_3N_4 composite photocatalyst by improved separation of carriers

On the contrary, the photogenerated holes move from the valance band (VB) of WO_3 towards the VB of g-C_3N_4 because of the more positive VB edge of WO_3 (3.0 eV, vs. NHE) than that of g-C_3N_4 (1.7 eV, vs. NHE). The redistribution of electrons on one side of the junction (WO_3) and holes on the opposite side (g-C_3N_4) greatly reduces the electron–hole recombination, which promote the photocatalytic reactions to decompose RhB. As a result, the activity of WO_3/ g-C_3N_4 composites was much higher than that of WO_3 and the pure g-C_3N_4. Thus, the enhanced photocatalytic activity was mainly related to the heterojunction structure and the synergetic effect at the interface between g-C_3N_4 and WO_3.

4.1.7 Conclusions

In a nutshell, the presented work deals with the enhanced photodegradation over photostable WO_3/g-C_3N_4 composite. As expected, the synthesized hybrid photocatalyst has exhibited an improved photodegradation performance because of synergetic effect, where the photo excited electrons from g-C_3N_4 are efficiently separated, and are injected to the CB of WO_3. The highest photoactivity has been achieved for the optimum amount of WO_3 (10 %) combined with g-C_3N_4. The hybrid catalyst has also shown excellent stability and efficiency even after 5 runs of photodegradation process.

4.2 Synthesis, characterization and surface plasmon resonance (SPR) enhanced photocatalytic activity of Au-Ag alloy nanoparticles dispersed on g-C_3N_4

4.2.1 Introduction

Development of sustainable and renewable technologies has been strongly driven by depleting fossil fuel sources, energy growth demand, as well as concern over climate change. Several ground-breaking methodologies have been developed for conversion of solar energy into electrical and chemical energies. In 1972 [11], Fujishima and group applied titanium oxide for hydrogen production from water splitting under light irradiations, and since then photo-catalysis has become likely approach for addressing energy and environmental issues. It is an environmentally friendly technique of reducing organic pollution and subsequently rejuvenating our living environment in a sustainable manner. Semiconductor based photocatalysts have received great attention because of high oxidative and reductive power of generated carriers that catalyze the different reactions. TiO_2 is a popular semiconductor photocatalyst due to its distinctive electronic and optical features, lower cost, chemical stability and non-toxicity. However, its large band gap (3.2 eV) restricts effective absorption of visible light, which is around 42 % of the total light spectrum of the solar radiations [91-94].

In early 2009, g-C_3N_4 was first reported as a metal free visible-light driven organic photocatalyst by Wang et-al., and it was applied for water splitting under visible light exposure with triethanolamine as a sacrificial electron donor[74]. Subsequently, in order to overcome the inherent constrains of g-C_3N_4 -such as the high recombination rate of the photogenerated charge carriers- numerous g-C_3N_4 based composites have been reported [95-103]. To enhance the activity by surpassing the limitation associated with g-C_3N_4, some other modifications such as adjusting textural porosity [104] and doping with other materials have been stretched out [105].

Nanoparticles (NPs) of noble metals can efficiently absorb visible light because of their surface plasmon resonance (SPR), which can be tailored by their size, environment and shape. Recently, to activate g-C_3N_4 in broader visible light spectrum and to reduce the recombination of photogenerated carriers, noble metals loaded g-C_3N_4 catalysts have been reported such as gold nanoparticles supported on carbon nitride [18], Au/g-C_3N_4 nanocomposite [19], Ag-modified mesoporous g-C_3N_4 [106], hetrostructured g-C_3N_4/Ag/TiO_2[107], Ag@C_3N_4 core‑shell plasmonic composite [108] and g-C_3N_4/Ag_2O [109].

The current study is a step forward in extending the spectral response to broader visible light spectrum and enhancing the photocatalytic activity of g-C_3N_4 in the visible region where we deposited well-dispersed Au-Ag alloy nanoparticles with a user friendly technique. Moreover, after characterizing the synthesized materials, we investigated the photocatalytic performance of synthesized catalysts under sunlight illumination, and under pure visible light (400-800nm) irradiations provided by lamp for the degradation of Rhodamine B (RhB) as model substrate. Being prone to SPR assisted charge generation and transfer process, the performance of the synthesized catalysts was evaluated in the exposure of low energy monochromatic light (532 nm, green) generated by the laser. The mineralization efficiency of the catalysts was monitored by Total organic carbon (TOC) removal measurements. Langmuir-Hinshelwood kinetic model was used to evaluate the kinetics of the degradation as well as mineralization data.

4.2.2 Experimental Details

All reagents and chemicals used in the current study were of reagent grade and applied without further purification. Melamine ($C_3H_6N_6$, CP) was purchased from Tianjin China Chemical Reagents Ltd. $AgNO_3$ (99%), $HAuCl_4.3H_2O$ (99.9%), Sodium citrate (dehydrated, 99%) were procured from Sigma-Aldrich, whereas Rhodamine B was purchased from LAMBDA PKYSIK.

Pure g-C_3N_4 was prepared by direct pyrolysis of melamine at 500ºC for 4 h at the heating rate of 10˚C/min, whereas the de-amination treatment was performed at 550˚C for 2 h as per procedure detailed in the literature [110]. As detailed below, the modified Turkevich method was adopted for depositing different compositions of Au-Ag alloy NPs at the surface of g-C_3N_4 [28, 111]. In Au-Ag alloy loaded g-C_3N_4 photocatalysts, the proportion of Ag was fixed at 1%, whereas the amount of Au was varied as 0.5%, 1% and 3% with respect to the weight of g-C_3N_4. The required amounts of 0.01M $HAuCl_4.3H_2O$ and 0.01M $AgNO_3$ precursor solutions were mixed and boiled under vigorous stirring (400-600 rmp). 1 ml of freshly prepared sodium citrate was added and re-boiled for 30 min which resulted in Au-Ag colloidal NPs solution. The appropriate amount of g-C_3N_4 was dispersed in colloidal Au-Ag NPs solution ultrasonically. The dispersion of Au-Ag NPs and g-C_3N_4 was subjected to UV light exposure for photo-impregnation process under vigorous stirring for 30 min. A 450 W Xenon arc lamp equipped with UV band pass filter, Oriel, USA was used as the UV source. The slurry was filtered, washed and dried overnight at 110ºC under vacuum. The same protocol was adopted for the synthesis of 1% Ag and 1% Au loaded g-C_3N_4.

The crystal structure of synthesized catalysts was analyzed with wide angle X-ray diffractometer (Philips X'Pert PRO 3040/60) equipped with Cu-Kα radiation source with range 2θ = 10º to 2θ = 90º. The microstructure and morphology of prepared samples were examined with Field emission scanning electron microscopy (FESEM, Tescan Lyra-3). The fine structure analysis of synthesized powders was carried out by transmission electron microscopy (TEM), JEM2100F, JEOL at 200KV. A JASCO, V-670, UV-vis-NIR spectrophotometer was used for recording the solid-state absorption and diffused reflectance spectra (DRS) of the synthesized catalysts using $BaSO_4$ pellet as a reference. The photoluminescence emission spectra were acquired by spectro-flourometer (Horiba Jobin Yvon), using the Xenon lamp as excitation source. All the samples were excited at 365 nm, and the emission spectra were recorded in 400 to 700 nm range. The XPS profile of 3% Au-Ag/g-C_3N_4 sample was acquired by a wide survey scan using X-ray Photoelectron Spectrometer (PHI 5000 Versa Probe II, ULVAC-PHI Inc.). The binding energy was varied between 0 eV to 1100 eV. The oxidation states of the metallic components were evaluated by comparing the obtained binding energy values with that of standard values. Gaussian model was applied for curve fitting and the identification of the number and precise binding energy of each state.

The photocatalytic performance of the synthesized catalysts (g-C_3N_4, Ag/g-C_3N_4, Au/g-C_3N_4 and (0.5%, 1%, 3%) Au-Ag/g-C_3N_4) was evaluated for the degradation (decolorization/mineralization) of Rhodamine B (10 ppm) in 200ml cylindrical glass reactor made up of Pyrex® glass. A 450-W Xe arc lamp (Oriel, USA) equipped with UV cut off filter was used as excitation source. The experiments were performed in batches. Prior to photocatalytic studies, the dark experiments were performed to establish the adsorption-desorption equilibrium between the dye and the catalysts. In a typical photocatalytic experiment, with visible light source, 100 ml of dye/catalyst suspension containing, 100 mg of the respective catalyst, was exposed to visible light (420-800nm) for 240 min under stirring. The samples (5 ml each) were drawn from the reactor after every 15 min in the initial 60 min, after every 30 min in the next hour and after 60 min in the final 120 min. After centrifugation at 4000 rpm for the removal of catalyst, the progress of the decolorization process was monitored by UV visible spectroscopy. A JASCO 570 UV-Vis spectrophotometer was employed to record the absorption spectra of the exposed samples. The mineralization progress was monitored by measuring the total organic carbon (TOC) of the samples by using TOC-VCPH total carbon analyzer supplied by Shimadzu Corporation, Japan. The experiments were performed at 25 ±1ºC. The performance of the synthesized catalysts in a complete spectrum of 450 W medium pressure mercury lamp was also evaluated. The experimental conditions, collection and analysis of the samples were similar to that of the experiments in the visible light exposure. The role of SPR in the photocatalytic process was evaluated by exposing the 100 ml of the catalyst/dye suspension of the same composition, as used for visible or sunlight experiments, to low energy (30 mJ) 532 nm laser light in a Pyrex® glass reactor fitted with quartz window under stirring. The 3%Au-Ag/g-C_3N_4 catalyst with the maximum intensity SPR band, evaluated by solid state absorption spectra, was used for the study. The details of the reactor used are mentioned elsewhere [112-115]. For better exposure the beam diameter was expanded to 5 mm. The blank experiment, i.e. without catalyst, was performed to evaluate the possible role of direct photolysis in the degradation experiments.

4.2.3 Results and Discussion

The comparison of the solid-state absorption spectra of pure, Ag, Au and Au-Ag alloy (0.5% Au, 1% Au, 3% Au) loaded g-C_3N_4 is presented Fig 4.12. A broad absorption band in 500-600 nm range was observable for the samples loaded either with pure Au or Au-Ag alloy nanoparticles whereas no distinct absorption band was observed for pure or Ag loaded g-C_3N_4 rather an enhanced absorption of Ag/g-C_3N_4 was noticed in 400-500 nm range. Although silver (Ag) nanoparticles exhibit strong SPR in the visible region, however, owing to the sensitivity to oxidation under mild conditions the surface of Ag NPs is converted to Ag_2O that results in the suppression of distinct SPR band rather enhanced absorption were witnessed. Au NPs are inert in nature; therefore, exhibit a strong SPR band in the visible region even in the oxidizing environment. The exploded view of the absorption spectra in 450-650 nm rage is presented in the inset of Fig 4.12 where the SPR band for 3% Au-Ag/g-C_3N_4 appeared at ~536 nm. The mild shifting in the position of the SPR towards longer wavelengths with the decreasing Au concentration depicted that the SPR band tuning can be accomplished by controlling the Au loading [116]. The mild variation in the observed value compared to the literature value of ~525 nm for the free Au nanoparticles in solution [117] was probably due the immobilization of NPs at the surface of g-C_3N_4, matrix effect, Au-Ag alloy formation and the measurements in the solid-state. The graphical evaluation of the bandgaps, obtained by plotting (F(R) x h ν)1/2 versus the photon energy (h ν), of g-C_3N_4, Ag/g-C_3N_4, Au/g-C_3N_4, 0.5% Au-Ag/g-C_3N_4, 1% Au-Ag/g-C_3N_4 and 3% Au-Ag/g-C_3N_4 is presented in the Fig 4.13-4.18.

The bandgaps of all the catalysts appeared in 2.7-2.8 nm range. The bandgap value of ~2.75 eV for g-C_3N_4 was in accordance with the literature [118-120].

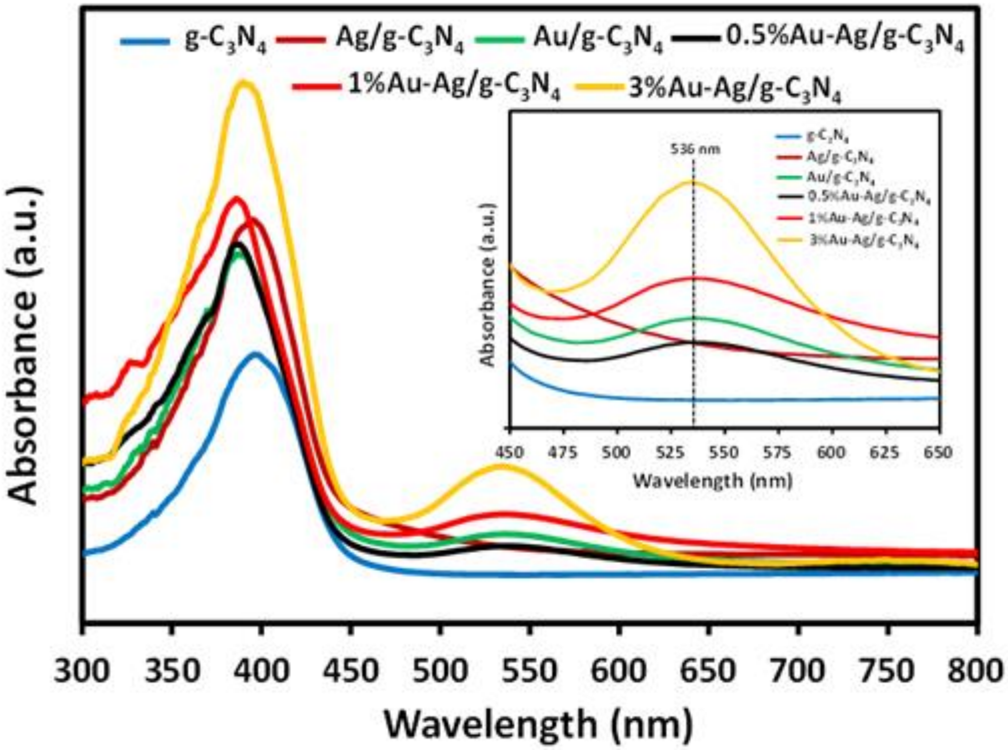

Figure 4.12 Comparison of the absorption spectra of g-C_3N_4, Ag/g-C_3N_4, Au/g-C_3N_4, 0.5%Au-Ag/g-C_3N_4, 1%Au-Ag/g-C_3N_4 and 3%Au-Ag/ g-C_3N_4. The inset shows the exploded view of the absorption spectra to elucidate the SPR resonance band

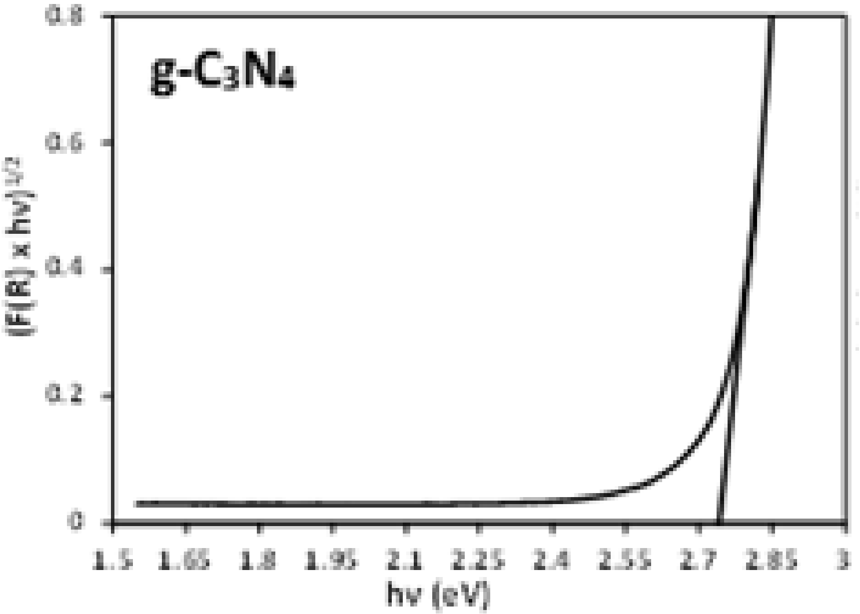

Figure 4.13 The graphical evaluation of the bandgaps obtained by plotting (F(R) x hv)$^{1/2}$ versus the photon energy (hv) of g-C_3N_4

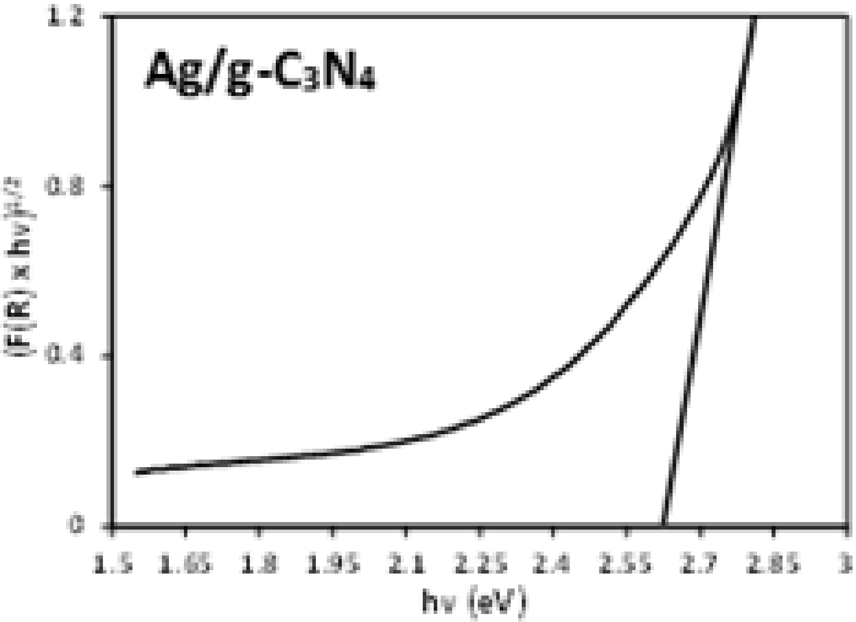

Figure 4.14 The graphical evaluation of the bandgaps obtained by plotting (F(R) x hv)$^{1/2}$ versus the photon energy (hv) of Ag/g-C_3N_4

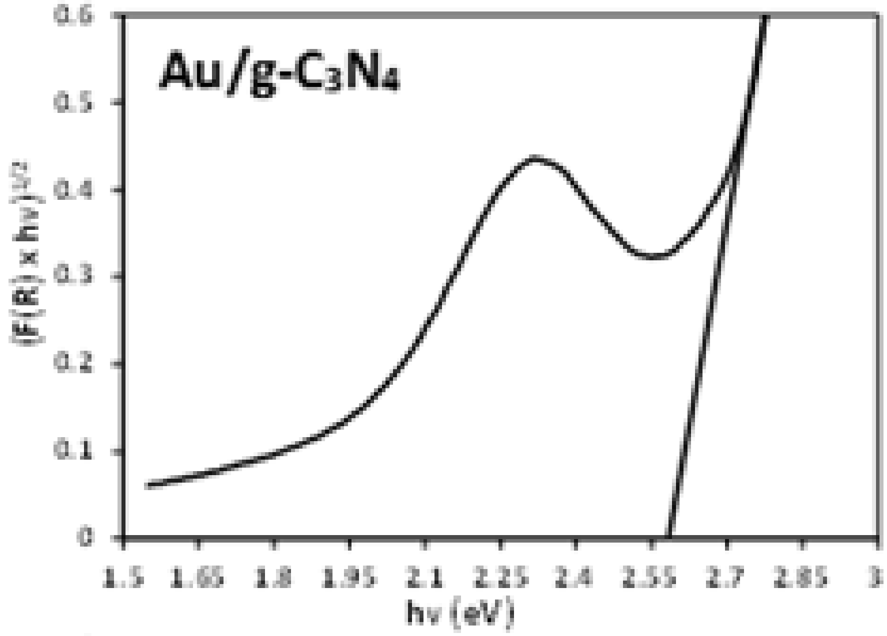

Figure 4.15 The graphical evaluation of the bandgaps obtained by plotting (F(R) x hv)$^{1/2}$ versus the photon energy (hv) of Au/g-C_3N_4

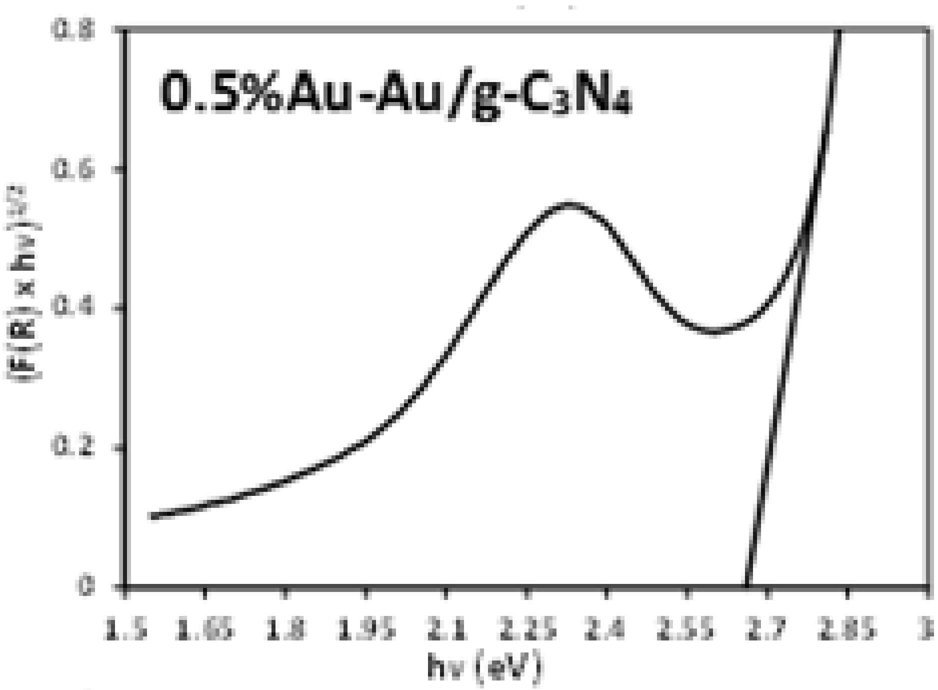

Figure 4.16 The graphical evaluation of the bandgaps obtained by plotting (F(R) x hv)$^{1/2}$ versus the photon energy (hv) of 0.5%Au-Ag/g-C_3N_4

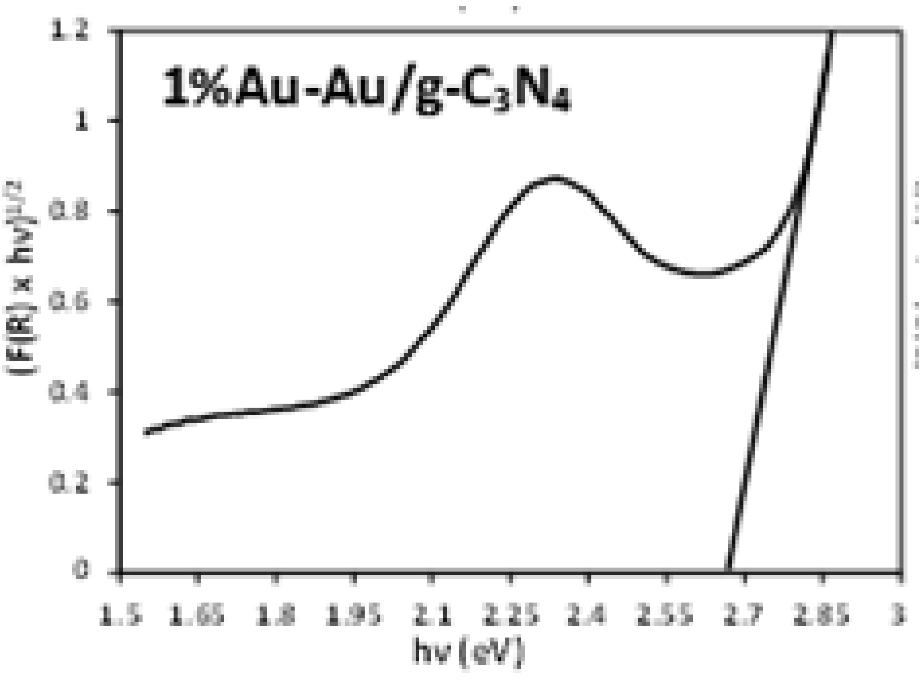

Figure 4.17 The graphical evaluation of the bandgaps obtained by plotting (F(R) x hv)$^{1/2}$ versus the photon energy (hv) of 1%Au-Ag/g-C_3N_4

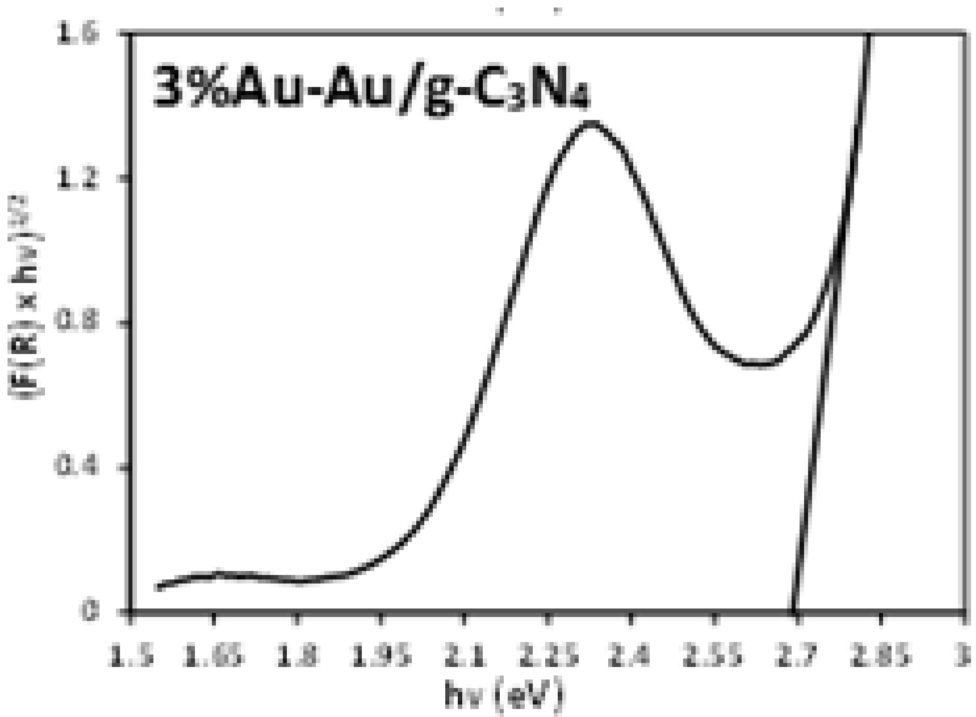

Figure 4.18 The graphical evaluation of the bandgaps obtained by plotting (F(R) x hv)$^{1/2}$ versus the photon energy (hv) of 3%Au-Ag/ g-C_3N_4

The PL spectra of g-C_3N_4, Ag/g-C_3N_4, Au/ g-C_3N_4, 0.5% Au-Ag/g-C_3N_4, 1% Au-Ag/g-C_3N_4 and 3% Au-Ag/g-C_3N_4 are compared in the Fig 4.19 Pure g-C_3N_4 is a luminescent material and the observed strong emission band centered at 460 nm, attributed to bandgap de-excitation, was in accordance with the literature [121]. A significant decrease in the intensity of the principal band (460 nm), to a varying extent, was ascribed to the excited electrons trapping ability of Ag, Au and Au-Ag alloy nanoparticles deposited at the surface of g-C_3N_4. The decreased intensity of the PL bands with the dispersed Ag, Au and Au-Ag alloy NPs indicated the decreased recombination extent of charge carriers. For Au-Ag alloy deposition the quenching of the deexcitation process was enhanced with the increasing Au contents. The comparison of PL spectra of Ag g-C_3N_4 and

Au/ g-C_3N_4 revealed better quenching ability of Au compared to Ag, whereas the performance of Au-Ag alloy was even better than Au/g-C_3N_4.

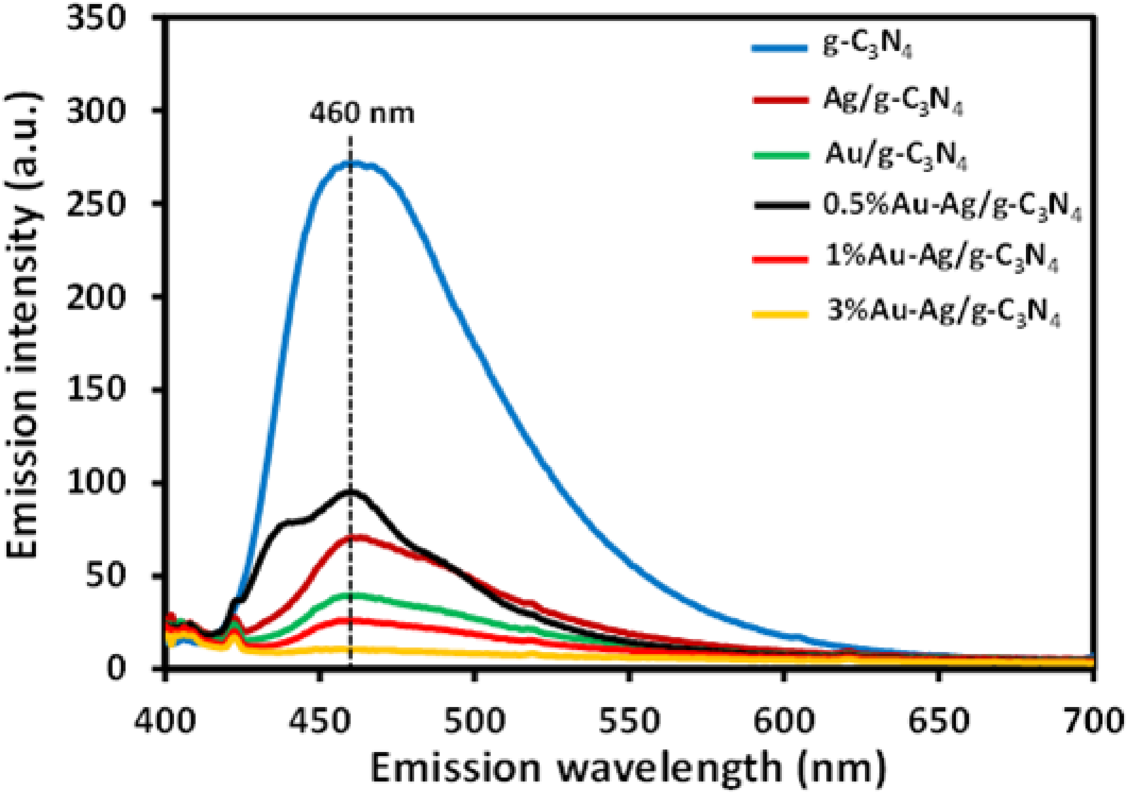

Figure 4.19 Comparison of the PL spectra of g-C_3N_4, Ag/g-C_3N_4, Au/g-C_3N_4, 0.5%Au-Ag/g-C_3N_4, 1%Au-Ag/g-C_3N_4 and 3%Au-Ag/ g-C_3N_4 photocatalysts excited at 350 nm

The XRD patterns for g-C_3N_4, Ag/g-C_3N_4, Au/g-C_3N_4, and the series of Au-Ag alloys deposited on g-C_3N_4 are compared in Fig 4.20. The reflection at $2\theta = 13.3^\circ$ and $2\theta = 27.5^\circ$ were attributed to (100) and (002) crystal planes of tris-s-triazine units and interlayer stacking of aromatic segments of g-C_3N_4, respectively [122]. For Ag and Au nanoparticles dispersed g-C_3N_4 photocatalysts, the diffraction peaks at 38.3°, 44.5° and 64.6° were attributed to (111), (200) and (220) planes of Ag and Au, respectively. Interestingly, the XRD reflections due to Ag and Au appear almost at the same position, therefore, it was difficult to differentiate between the reflection of Au and Ag in the XRD patterns of Ag-Au alloy NPs deposited g-C_3N_4. The exploded view of the XRD pattern in the 2θ range of 35º to 50º is presented in the inset of Fig 4.20 where the growth of diffraction peaks at 38.3º (111) and 44.5º (200) with the increasing Au contents can be witnessed. The reflections of Au in the XRD patterns of Au/g-C_3N_4 and Au-Ag alloy deposited g-C_3N_4 were matched with JCPDS # 04-0784.

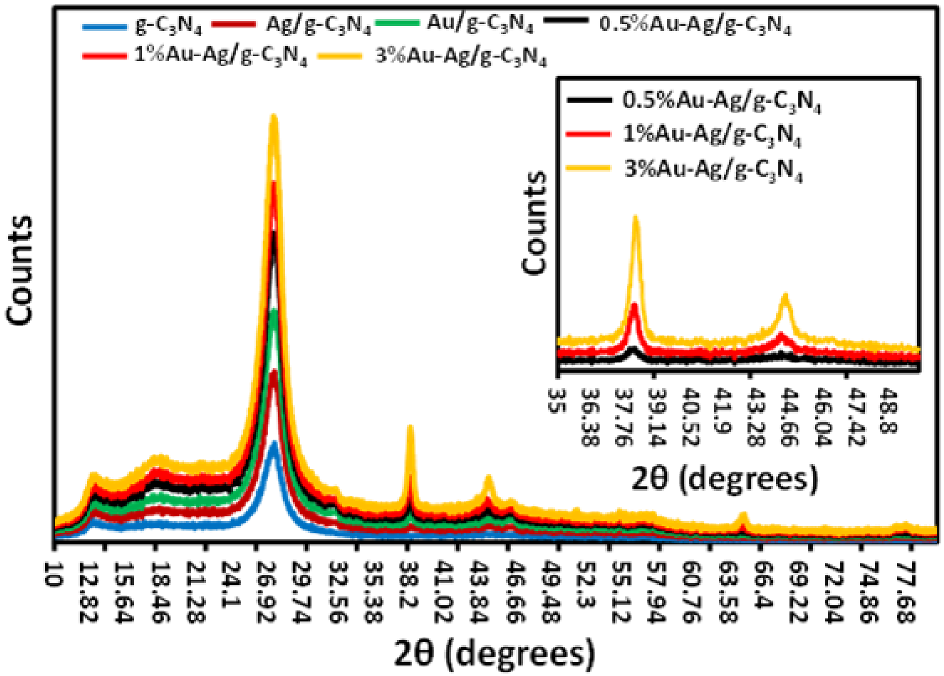

Figure 4.20 The comparison of the XRD patterns of g-C_3N_4, Ag/g-C_3N_4, Au/g-C_3N_4, 0.5%Au-Ag/g-C_3N_4, 1%Au-Ag/g-C_3N_4 and 3%Au-Ag/ g-C_3N_4 in the range $2\theta = 10^o$ to $2\theta = 80^o$. The inset shows the growth of Au (200) reflections with increasing Au contents in 35-50º range

The microstructure and morphology of the synthesized samples were examined by FESEM imaging. The same resolution (100kx) FESEM images of g-C_3N_4, Ag/g-C_3N_4, Au/g-C_3N_4, and 1% Au-Ag and 3% Au-Ag alloy deposited on g-C_3N_4 are presented in Fig 4.21**.** The 100 and 200kx images of pure g-C_3N_4 ((Fig 4.21 (a & b)) revealed the sheet-like composite structure composed of irregular crystals. In the backscattered micrograph (Figure 4.21(c)) of Ag/g-C_3N_4, the adhered spots of Ag NPs are prominent at the surface of g-C_3N_4. The interaction of the electron beam with the electron excessive Au, resulted in the brightening of the NPs in Au and Au-Ag deposited g-C_3N_4 samples, however, the homogeneously distributed Au and Au-Ag alloy particles are evidently observable on the surface of g-C_3N_4. The estimated particle size of Ag NPs ranged between 30 to 50 nm in Ag/g-C_3N_4, whereas the NPs in Au/g-C_3N_4 and Au-Ag alloy samples ranged between 10 and 30 nm. The results regarding the particle size measurements were consistent with the earlier observations [123], as the growth of Ag-Au alloy is initiated with formation of smaller gold NPs as nucleation centers, followed by the simultaneous deposition of both Ag and Au atoms. Therefore, higher concentration of Au in alloy results in more gold nuclei and reduces size of alloy particles, whereas the higher Ag concentration leads to larger alloy NPs.

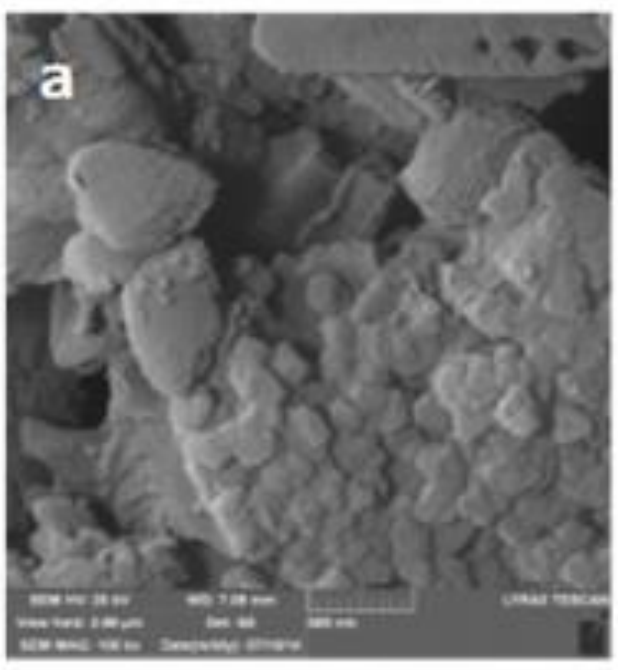

Figure 4.21(a) FESEM image of g-C_3N_4 at 100kx

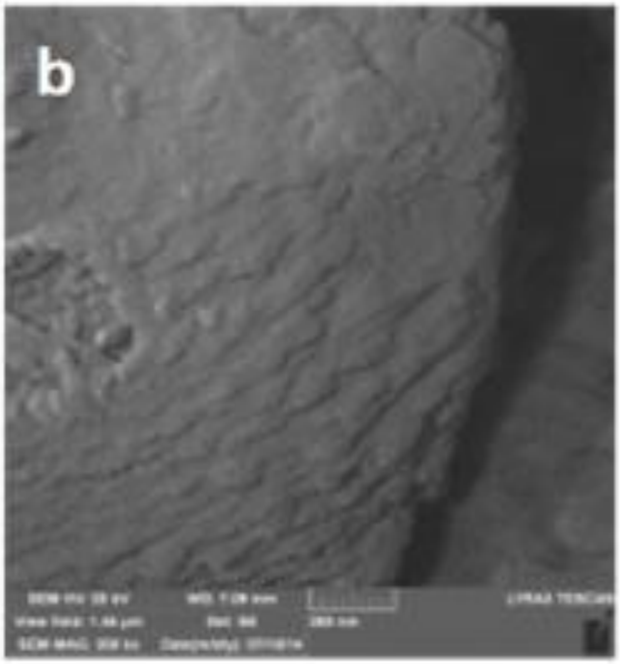

Figure 4.21(b) FESEM image of g-C_3N_4 at 200kx

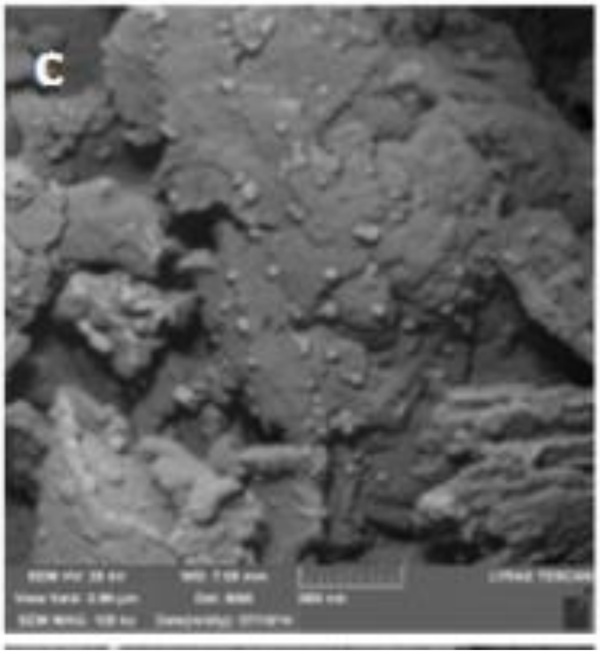

Figure 4.21(c) FESEM image of Ag/g-C_3N_4 at 100kx

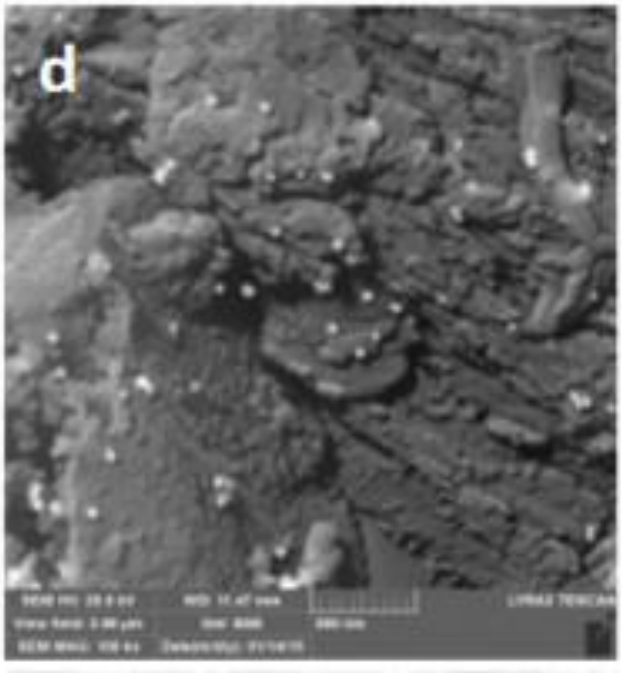

Figure 4.21(d) FESEM image of Au/g-C_3N_4 at 100kx

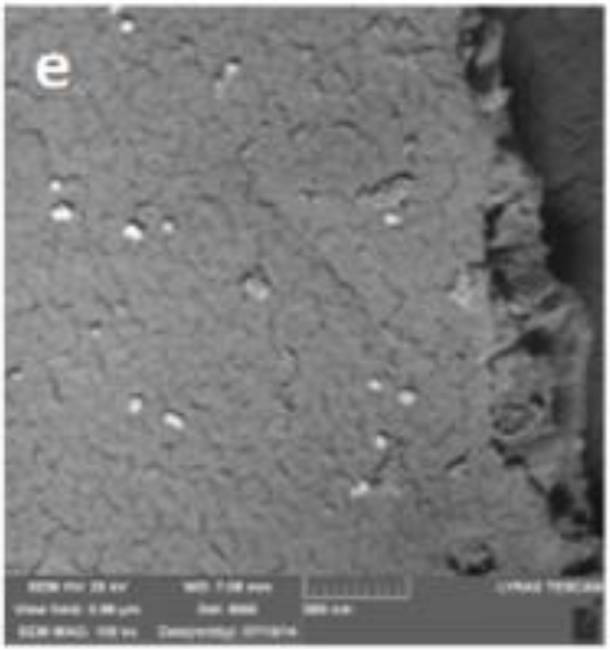

Figure 4.21(e) FESEM image of 1%Au-Ag/g-C_3N_4 at 100kx

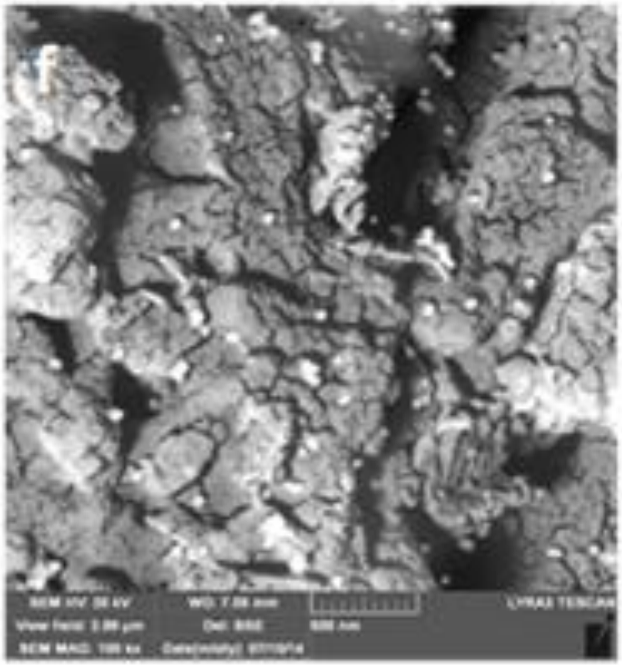

Figure 4.21(f) FESEM image of 3%Au-Ag/ g-C_3N_4 at 100kx

The fine morphology and even distribution of Au and Ag in Au-Ag alloy dispersed on g-C_3N_4 was further investigated by TEM analysis and the respective images of 1% and 3% Au-Ag/g-C_3N_4, as presented in Fig 4.22 (a-d**)**. For 1% Au-Ag dispersed samples having 1:1 proportion of the Au and Ag, the regular shaped spherical particles with an average size of ~25 nm of Au-Ag alloy particles were observed (Fig 4.22 (a)). Additionally, a uniform distribution of Au and Ag entities was witnessed in the alloy formation (Fig 4.22 (b)). The appearance of the particles revealed homogenous composition rather than individual Au/Ag particles or clusters. The increased Au contents, i.e. 3:1 (Au:Ag) resulted in the deformation of the shapes of the particle (Fig 4.22 (c)). Additionally, a relatively wider particle size distribution was noticed; however, the comparison of the fringes revealed that the homogeneity was independent of the particle size distribution of 10-30 nm range (Fig 4.22 (d)). The individual lattice planes are distinctly visible in this image. This investigation also confirmed the absence of lattice mismatch with the formation of alloy solid solution. The same was expected as Au and Ag have very close lattice constants of 0.408nm and 0.409 nm, respectively [124].

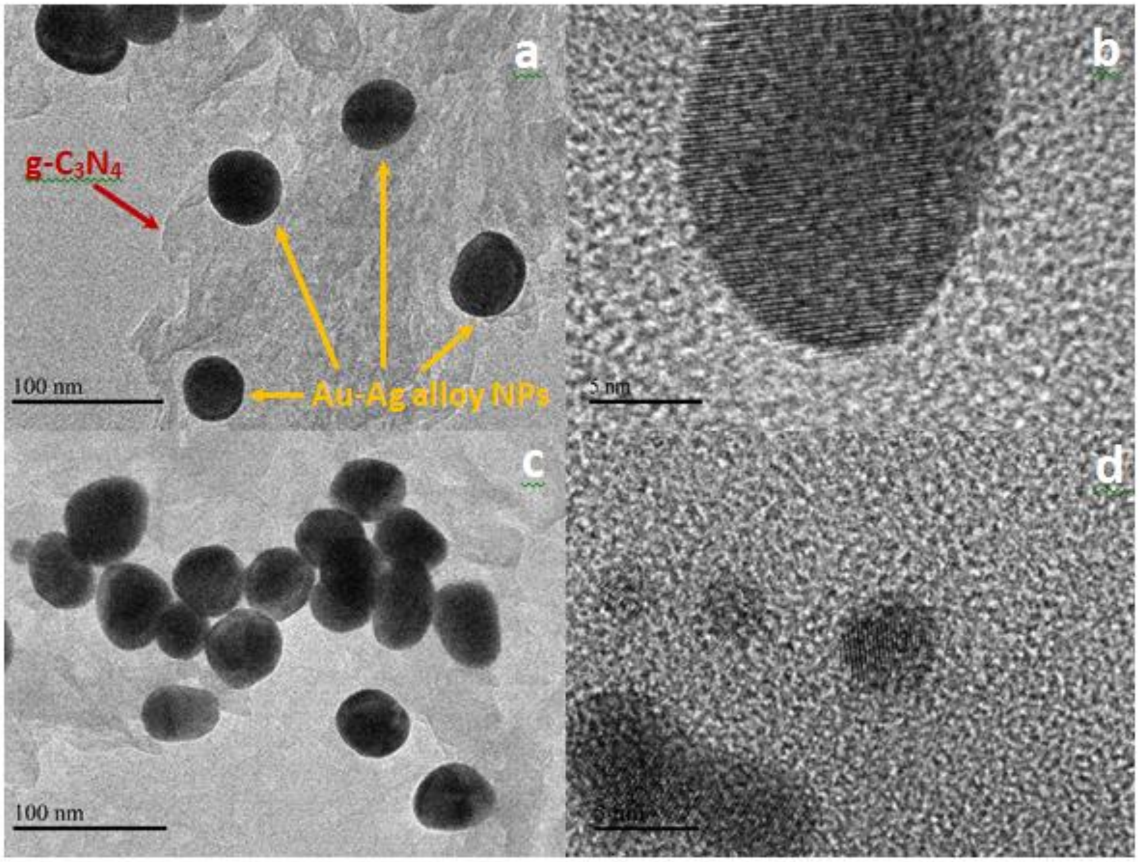

Figure 4.22 (a-d). The comparison of HRTEM images of 1% Au-Ag/g-C_3N_4 (a, b) and 3%Au-Ag/ g-C_3N_4 (c,d).

As presented in Fig 4.23, the estimation of the variations in the oxidation states of the metallic constituents involved i.e. Au and Ag, during the synthetic process were estimated by the XPS survey scan of 1% Au-Ag/g-C_3N_4 recorded in the binding energy range of 0 eV to 1100 eV. All the expected components, i.e. C, N, O, Ag and Au were observed in the survey scan. The intensities of the corresponding peaks were in accordance with the composition of each component. The precise peak maxima’s were identified by applying the Gaussian model for curve fitting on the individual and splitted peaks.

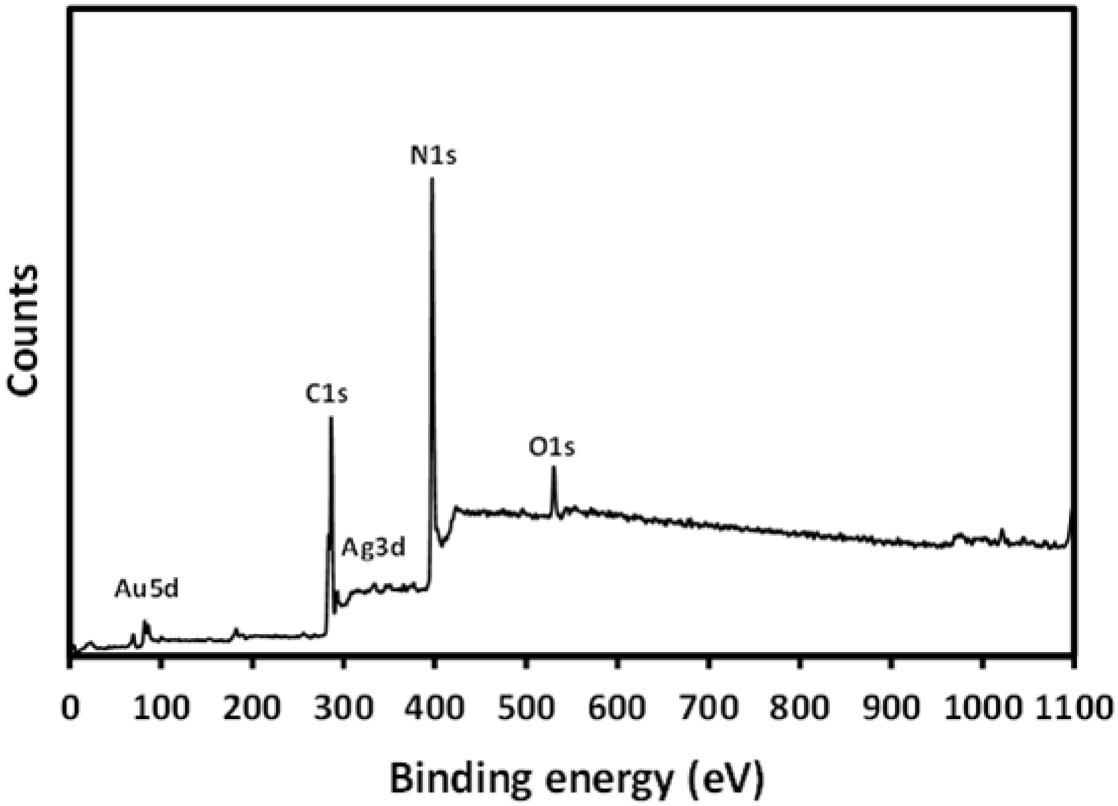

Figure 4.23 The XPS survey scan of 1%Au-Ag/g-C_3N_4.

The fitted peaks for the individual elements are presented in Fig 4.24. The evaluated binding energy value of 530.45 eV for Oxygen 1s shown in (Fig 4.24(a)) was in accordance with the literature [125]. The peaks at 283.2 eV and 286.4 eV were identified in the deconvolated Carbon 1s spectrum (Fig 4.24(b)) and were assigned to sp^2 hybridized carbon in C-C and NC=N bonds in the nitrogen containing aromatic rings respectively. As shown in Fig 4.24(c), the intense peak in N1s spectrum centered at 297.1 eV was assigned to sp^2 hybridized nitrogen of CN-C bond in triazine ring. Due to the dispersion of Au-Ag alloy at the surface of g-C_3N_4, the observed binding energy values of C1s and N1s were slightly lower than those mentioned in the literature for pure g-C_3N_4 [126]. The well-resolved spin-orbit splitted doublet of the Au 4f core (Fig 4.24(d)) levels corresponding to the Au4f7/2 and Au4f5/2 states, were observed at 83.1 eV and 86.9 eV respectively, confirmed the existence of Au in zero oxidation state. The minor deviation from the standard values and the asymmetry in the peak shapes was due to the alloy formation with Ag. The spectra of the splitted Ag 3d levels i.e. Ag3d5/2 and Ag3d3/2 are presented in Fig. 4.24(e) and (f) respectively. Interestingly, similar to that of Au4f splitted spectrum, due to the alloy formation, both the Ag peaks were asymmetric in shape. The separate deconvolution of the peaks revealed that the 3d3/2 peak of Ag at 373.8, whereas Ag3d5/2 was centered at 368.4 eV. The observed values confirmed the existence of Ag as elemental Ago rather the Ag_2O as Ag+ peak in the XPS analysis appear between 367.3 to 367.8 eV[127].

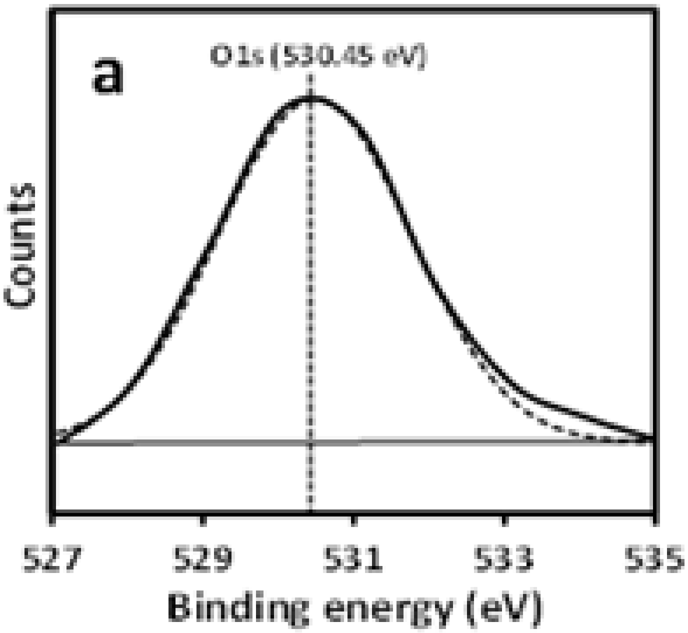

Figure 4.24(a) Curve fitted peak in the XPS analysis of 1%Au-Ag/g-C_3N_4 for O1s

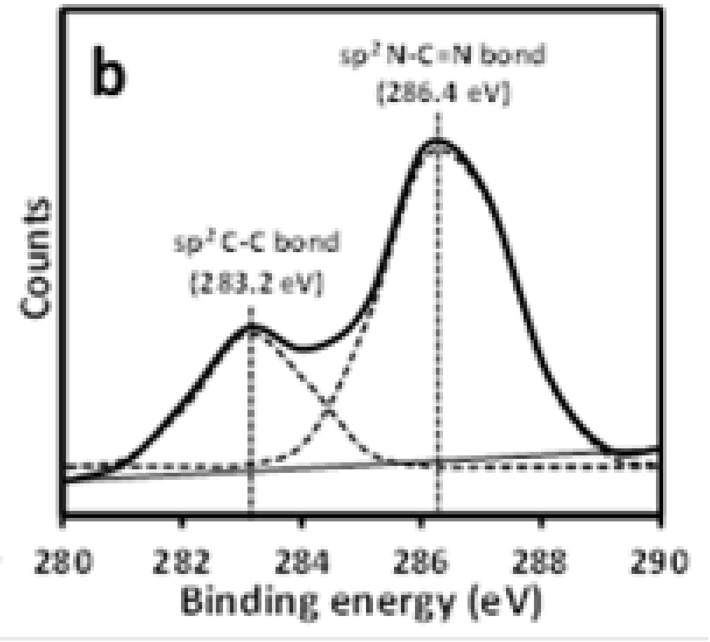

Figure 4.24(b) Curve fitted peak in the XPS analysis of 1%Au-Ag/g-C_3N_4 for C1s

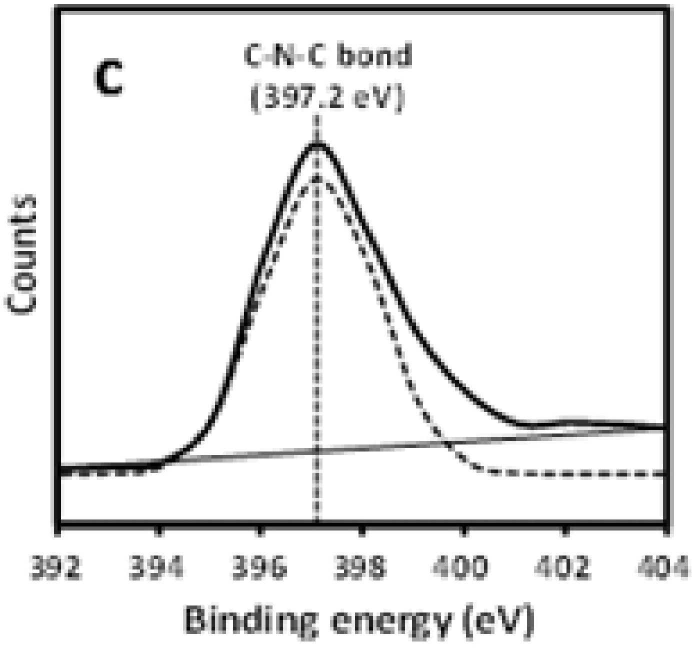

Figure 4.24(c) Curve fitted peak in the XPS analysis of 1%Au-Ag/g-C_3N_4 for N1s

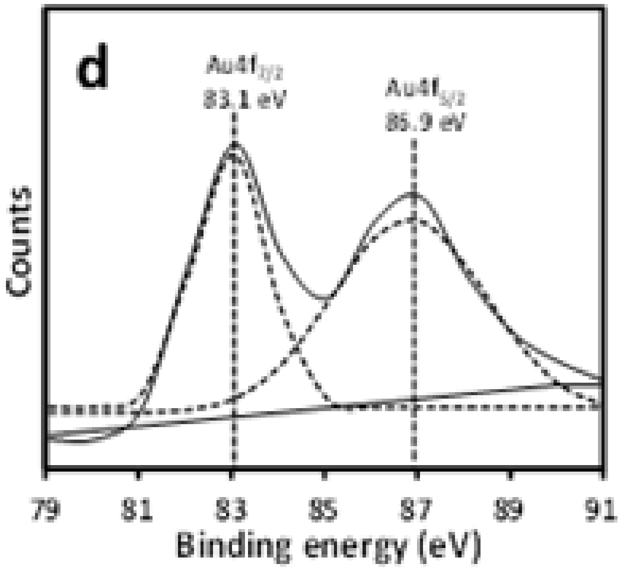

Figure 4.24(d) Curve fitted peak in the XPS analysis of 1%Au-Ag/g-C_3N_4 for Au5f

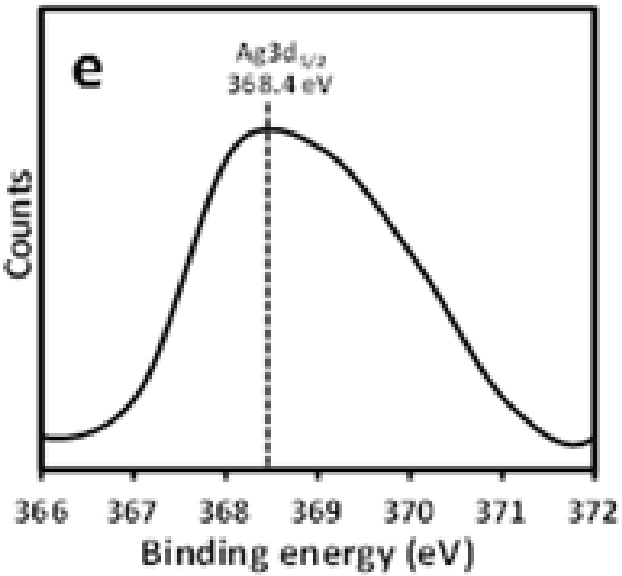

Figure 4.24(e) Curve fitted peak in the XPS analysis of 1%Au-Ag/g-C_3N_4 for Ag3d$_{5/2}$

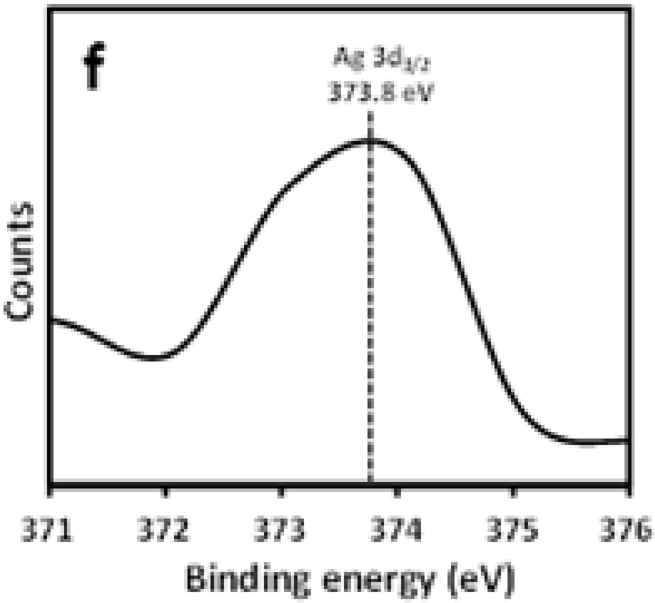

Figure 4.24(f) Curve fitted peak in the XPS analysis of 1%Au-Ag/g-C_3N_4 for Ag3$d_{3/2}$

4.2.4 Photocatalytic studies

The initiation of the photocatalytic process in the aqueous system is dependent on the energy of incident photons with the generation of pair of charge carries per adsorbed photon of energy equal or higher than the bandgap of semiconductor. The productive use of charge carriers is primarily dependent on their capture by the adsorbed species such as the adsorbed water and oxygen molecules or the traps placed at the surface of the catalyst before being wasted in nonprolific radiative processes. The transfer of the charge carriers to adsorbed oxygen/water molecules and their conversion to reactive radical species generally termed as reactive oxygen species (ROS) is electrochemically restricted process and requires the minimum potential of the valance and conduction band edges i.e. +1.23V for H_2O oxidation and -0.28V for O_2 reduction, respectively. The pH of the system and pHZPC of the semiconductor are the vital parameters that determine the life expectancy, population and the nature of the reactive species produced in the photocatalytic system under illumination. Besides the other short-lived ionic and radical species, in the photocatalytic processes, the hydroxyl (HO·) and superoxide ($O_2^{\cdot -}$) radicals are recognized as primary oxidants [128-131]. The formation of these radicals can be elaborated by Equation (1) and (2) below.

$$h^+ + H_2O \longrightarrow H^+ + OH^{\cdot}$$

$$\mathbf{O_2} + \mathbf{e_{cb}^-} \longrightarrow \mathbf{O_2^{\cdot -}}$$

The comparison of the percentage decolorization of RhB (10 ppm), as measured by the UV-visible absorption spectroscopy, as a function of the visible light (420-800 nm) exposure time in the presence of g-C_3N_4, Ag/g-C_3N_4, Au/g-C_3N_4, 0.5%, 1% and 3% Au-Ag alloy deposited on g-C_3N_4 is presented Fig. 4.25. A varying response of different catalysts was noticed, however, the decolorization of the dye on the Au and Ag loaded g-C_3N_4 either pure or in the alloy form, was higher than that of pure g-C_3N_4. In this context, compared to just ~4% degradation of dye for g-C_3N_4 in the initial 15 min of exposure, ~6%, ~8%, ~16%, ~20% and ~24% of the dye was decolorized in the same period over Ag/g-C_3N_4, Au/g-C_3N_4, and 1% Au-Ag and 3% Au-Ag alloy deposited on g-C_3N_4 catalysts, respectively. For Au-Ag alloy system, an increasing trend of decolorization of the dye was noticed with the increasing Au contents, and ~90% of the dye was decolorized in 240 min of visible light exposure which was significantly higher than ~21% for bare g-C_3N_4. As evaluated by plotting ln(Co/C) versus the exposure time, the decolorization of Rhodamine on all catalysts obeyed the Langmuir-Hinshelwood kinetic model for pseudo first order reaction with acceptable correlation. The graphical evaluation of the rate constants is presented in the inset of Fig 4.25. The evaluated rate constants for g-C_3N_4, Ag/ g-C_3N_4, Au/ g-C_3N_4, 0.5%, 1% and 3% Au-Ag alloy dispersed on g-C_3N_4 were 0.0011 min-1, 0.0036 min-1 and 0.0045 min-1, 0.0062 min-1 and 0.0072 min-1 and 0.0086 min-1 respectively, with the average correlation factor of ~0.96.

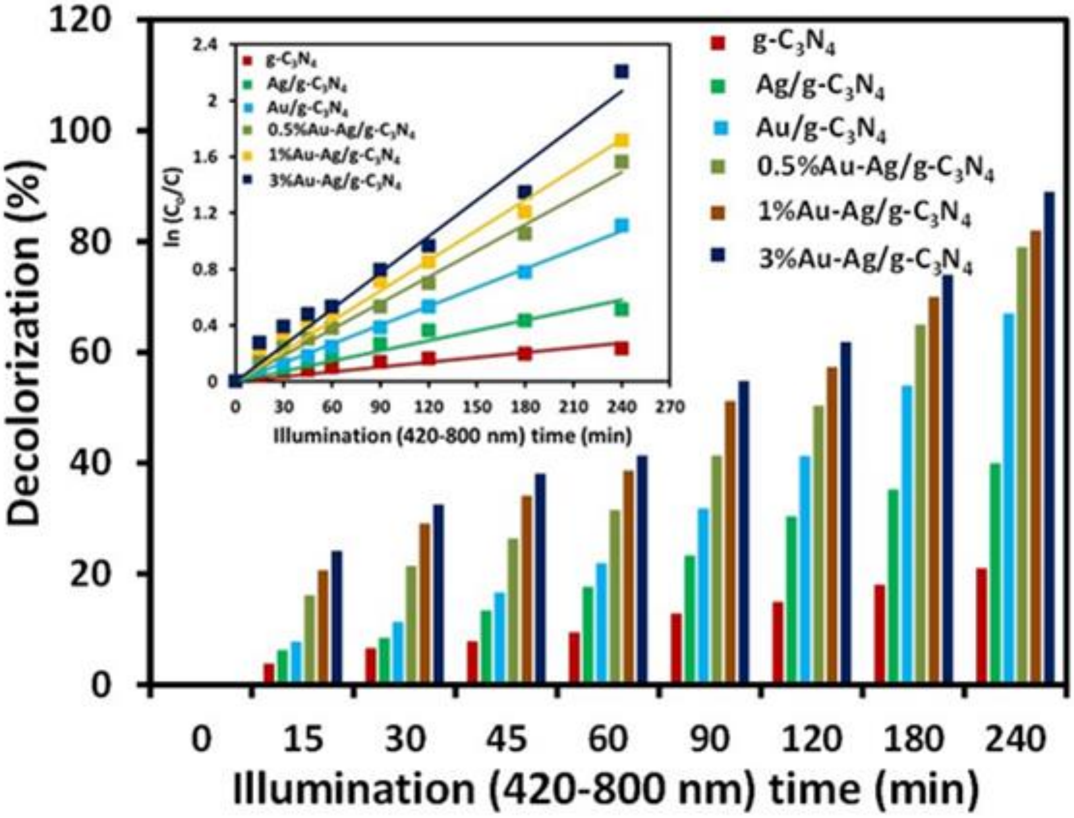

Figure 4.25 the comparison of the photocatalytic performance of $g-C_3N_4$, $Ag/g-C_3N_4$, $Au/g-C_3N_4$, $0.5\%Au-Ag/g-C_3N_4$, $1\%Au-Ag/g-C_3N_4$ and $3\%Au-Ag/ g-C_3N_4$ for the decolorization of Rhodamine B (10 ppm) in the visible light exposure. The inset shows the graphical evaluation of the rate constants.

The higher rate of degradation of dye decolorization in the visible region over Au-Ag alloy loaded $g-C_3N_4$ as compared to pure, mono metal NP (Au and Ag) loaded $g-C_3N_4$ predicted the supporting role of Au in enhancing the photocatalytic activity. No degradation of the dye was observable in the visible light exposure without the catalyst by plain irradiation of the pollutant i.e. direct photolysis.

The decolorization of Rhodamine B in the sunlight exposure (complete spectrum) on pure g-C_3N_4, Ag/g-C_3N_4, Au/g-C_3N_4, 0.5%, 1% and 3% Au-Ag alloy loaded g-C_3N_4 is presented in Fig. 4.26.

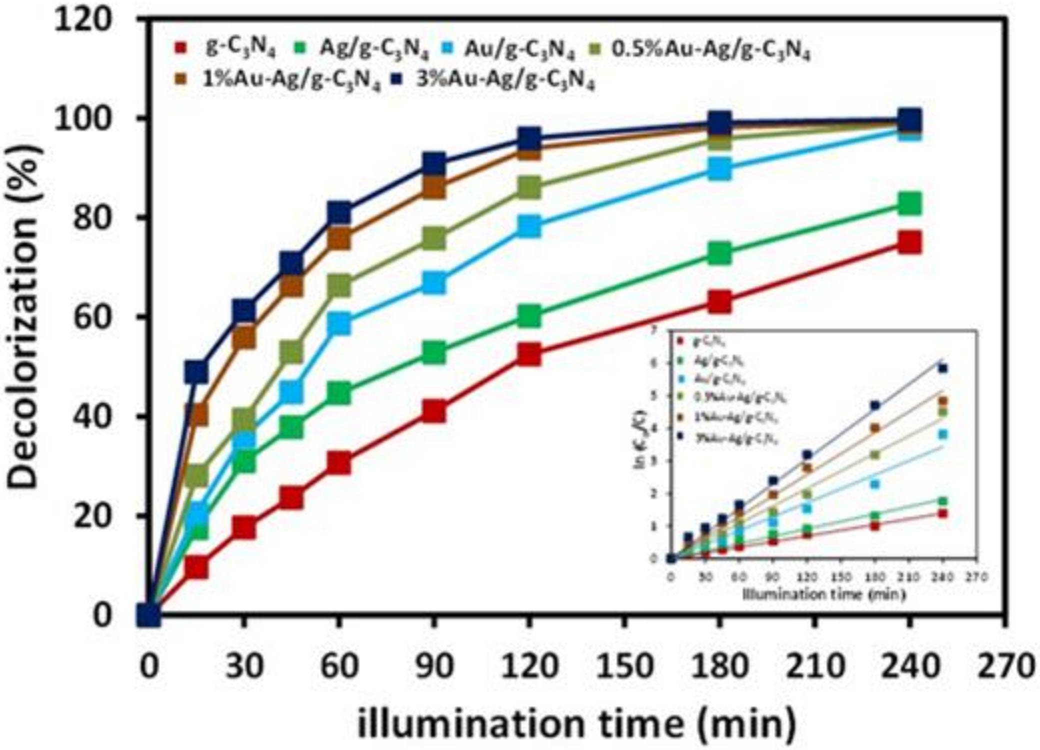

Figure 4.26 Comparison of the photocatalytic performance of g-C_3N_4, Ag/g-C_3N_4, Au/g-C_3N_4, 0.5%Au-Ag/g-C_3N_4, 1%Au-Ag/g-C_3N_4 and 3%Au-Ag/ g-C_3N_4 for the decolorization of Rhodamine B (10 ppm) in the sunlight exposure. The inset shows the graphical evaluation of the rate constants

With the involvement of UV radiations of the sunlight, a significantly higher activity, compared to the visible light exposure, was witnessed. The pure g-C_3N_4 managed to decolorize ~31% of the dye in the initial one hour of the sunlight that was significantly higher than that of ~9% in the visible region in the same span of time. The increased activity of g-C_3N_4 in sunlight exposure may be attributed to the fact that g-C_3N_4 with a bandgap of 2.79 eV can utilize only a minimal fraction of available photons when exposed to visible light whereas that fraction is substantially increased in the complete spectrum sunlight causing a significant increase in activity. The initially high activity proposed the facilitating role of dispersed Ag NPs in capturing and disbursing the excited electrons generated by the g-C_3N_4 base. Similar behavior was not witnessed for Au/g-C_3N_4 that predicts the resistance of Au against oxidation process. A consistent activity of Au-Ag loaded g-C_3N_4 catalysts indicated that the alloy formation protects Ag against oxidation. The Au-Ag alloy catalysts completely decolorized the dye in 240 min of sunlight exposure. The rates of degradation of the dye decolorization in sunlight exposure evaluated by plotting ln(Co/C) versus sunlight exposure, as presented in the inset of Fig 4.26, time were significantly higher than that of visible light.

CATALYSTS	**VISIBLE LIGHT**	**SUNLIGHT**
g-C_3N_4	**0.0011min^{-1}**	**0.0058min^{-1}**
Ag/g-C_3N_4	**0.0036min^{-1}**	**0.0076min^{-1}**
Au/g-C_3N_4	**0.0045min^{-1}**	**0.0143min^{-1}**
Au(0.5%)/Ag(1%)/g-C_3N_4	**0.0062min^{-1}**	**0.0179min^{-1}**
Au(1%)/Ag(1%)/g-C_3N_4	**0.0072min^{-1}**	**0.0215min^{-1}**
Au(3%)/Ag(1%)/g-C_3N_4	**0.0086min^{-1}**	**0.0255min^{-1}**

Table 2 Comparison of reaction rate constants of synthesized catalysts in visible light compared to sunlight exposure

The rate constants evaluated for g-C_3N_4, Ag/g-C_3N_4, Au/g-C_3N_4, 0.5%, 1% and 3% Au-Ag alloy dispersed on g-C_3N_4 were 0.0058 min-1, 0.0076 min-1 and 0.0143 min-1, 0.0179 min-1, 0.0215 min-1 and 0.0255 min-1 respectively, with the average correlation factor of ~0.98. In the blank experiments ~11% of the dye was degraded by direct photolysis.

The TOC removal (mineralization) of 10ppm of the Rhodamine B over g-C_3N_4, Ag/ g-C_3N_4, Au/g-C_3N_4, 0.5%, 1% and 3% Au-Ag alloy dispersed on g-C_3N_4 in artificial visible and natural sunlight exposure is presented in the Fig. 4.27(a) and (c), respectively. In the visible light exposure, as expected due to the bandgap restrictions, the TOC removal for pure g-C_3N_4 was almost negligible (≤ 5%) in 240 min of exposure, whereas, a significant enhancement in the TOC removal was noticed for Ag, Au, 0.5%, 1% and 3% Au-Ag alloy dispersed g-C_3N_4 where a TOC removal of ~27, ~41, ~38, ~47 and ~50% respectively, was witnessed in the same period of exposure. Due to the availability of sufficient number of photons with the extension of spectral range in the complete spectrum sunlight exposure the TOC removal efficiency of g-C_3N_4 was improved to ~40% in 240 min of exposure. Except for Ag/ g-C_3N_4 (~55%), the TOC removal for Au and Au-Ag alloy loaded g-C_3N_4 was higher than 65%. Interestingly, the performance of the Au- Ag alloy dispersed g-C_3N_4 was evidently better than Au/g-C_3N_4 where a TOC removal of ~79% was witnessed for 3% Au-Ag loaded g-C_3N_4 in 240 min of exposure. The evaluation of the kinetics of TOC removal extracted by plotting ln(Co/C) versus the exposure time (visible and sunlight) is presented in Fig 4.27 (b) and (d).

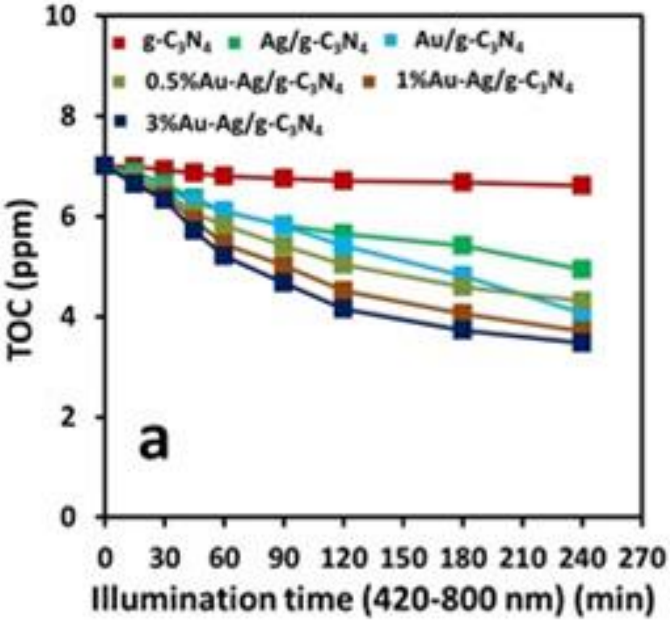

Figure 4.27(a) TOC removal over g-C_3N_4, Ag/g-C_3N_4, Au/g-C_3N_4, 0.5%Au-Ag/g-C_3N_4, 1%Au-Ag/g-C_3N_4 and 3%Au-Ag/ g-C_3N_4 for the mineralization of Rhodamine B (10 ppm) in visible light (420-800 nm) exposure.

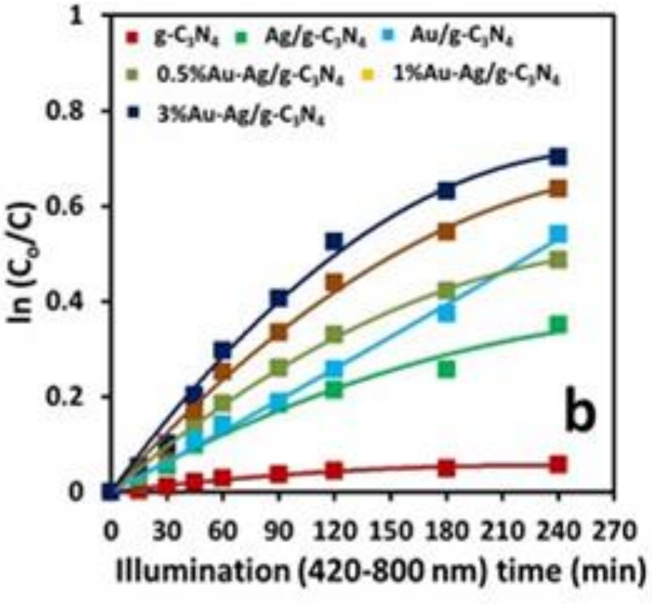

Figure 4.27(b) TOC removal plot of ln(C_o/C) versus illumination time over g-C_3N_4, Ag/g-C_3N_4, Au/g-C_3N_4, 0.5%Au-Ag/g-C_3N_4, 1%Au-Ag/g-C_3N_4 and 3%Au-Ag/ g-C_3N_4 for the mineralization of Rhodamine B (10 ppm) in visible light (420-800 nm) exposure.

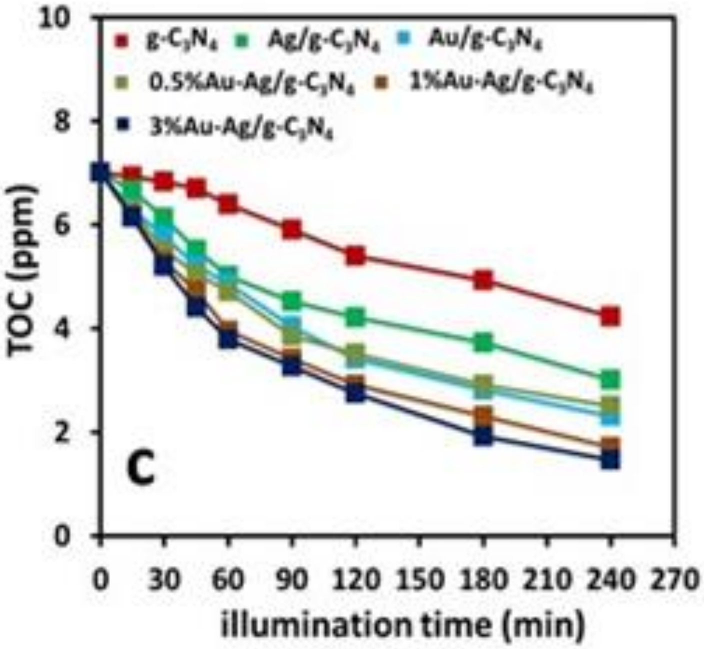

Figure 4.27(c) TOC removal over g-C_3N_4, Ag/g-C_3N_4, Au/g-C_3N_4, 0.5%Au-Ag/g-C_3N_4, 1%Au-Ag/g-C_3N_4 and 3%Au-Ag/ g-C_3N_4 for the mineralization of Rhodamine B (10 ppm) in complete spectrum (including UV portion)

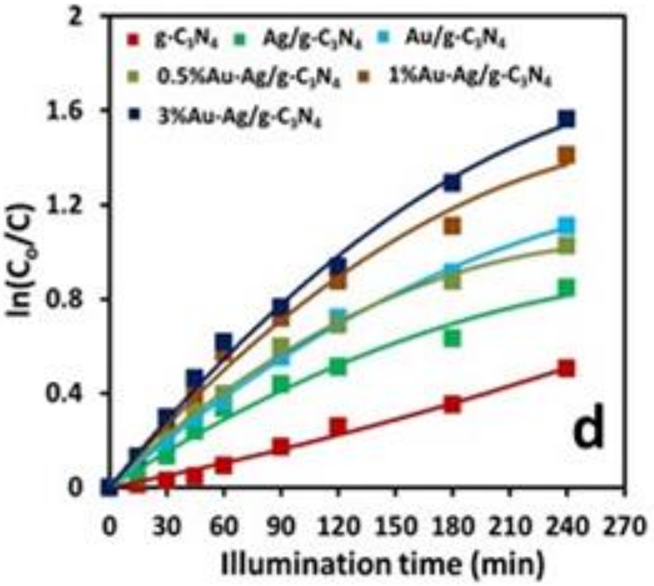

Figure 4.27(d) TOC removal plot of ln(C_o/C) versus illumination time over g-C_3N_4, Ag/g-C_3N_4, Au/g-C_3N_4, 0.5%Au-Ag/g-C_3N_4, 1%Au-Ag/g-C_3N_4 and 3%Au-Ag/ g-C_3N_4 for the mineralization of Rhodamine B (10 ppm) in complete spectrum (including UV portion) exposure.

Dyes are categorized by the presence of color generating centers (chromophores) and the stabilizing conjugated system. The interaction of the dyes with the reactive oxygen species in the photocatalytic system initially results in the decolorization, loss of color centers and conjugation, and the formation of intermediates. The further interaction of the ROS with the intermediates leads to the multistep mineralization process [132]. With the ability of absorbing a minimal fraction of the incident light in the visible region (420-800 nm), the low activity of pure g-C_3N_4 with the bandgap of 2.75 eV was expected, however, the significantly high degradation activity of the Ag, Au and Au-Ag alloy dispersed g-C_3N_4 compared to pure g-C_3N_4 revealed the prominent role of the metallic nanoparticles initially in the capture of the photo-excited electrons and finally, disbursement to the oxygen present in the system for the generation of superoxide radicals ($O_2^{\cdot -}$). The ability of the Ag, Au and Au-Ag alloy NPs for suppressing the recombination process is also verified by PL analysis (Fig. 4.19). The capture of electrons by the metallic NPs enhance the lifetime of the photogenerated holes, thus enhancing the yield of ROS other than superoxide anions. For Ag/g-C_3N_4, although the activity was higher as compared to pure g-C_3N_4 both in the visible light illumination as well as sunlight exposure, however, an initial sharp increase followed by the decrease in decolorization afterwards depicted the deactivation of the catalyst with time. As silver (Ag) is prone to oxidation under oxidizing environment, the formation of surface Ag_2O as a consequence of interaction with superoxide anion radicals and the other reactive oxygen species (ROS) resulted in the decreased activity. The sustained activity of Au/ g-C_3N_4 under both conditions of illumination depicted the resistance of Au to the photon induced oxidants. The enhanced and consistent activity of Au-Ag alloy dispersed g-C_3N_4 revealed the protection of Ag against oxidation in the blends by the Au contents. It is proposed that in a photocatalytic system the dyes are degraded either by direct or indirect photocatalysis mechanism [132]. The direct mechanism is based on the degradation of the dye by the interaction of the dye with the ROS generated by the direct absorption of photons by the semiconductor whereas the indirect mechanism operates by the injection of the energy, absorbed initially by the dye molecules, to the semiconductor. The indirect mechanism is more prevalent when the absorption maxima of the dye and the bandgap energy of the photocatalyst are close in energy, therefore, in the current case, the possibility of dye degradation by indirect mechanism is less likely, however cannot be negated completely.

In the complete spectrum sunlight exposure, with the upsurge in the fraction of the available photons to be absorbed, the enhanced activity of the pure as well as Au, Ag and Au-Ag alloy NPs loaded g-C_3N_4 was expected, however, the enhanced activity in the visible light exposure enlightened the critical role of some additional contributor in augmenting the photocatalytic degradation of Rhodamine B. The intense band centered at ~536 nm in the absorption spectra (Fig 4.28) of Au and Au-Ag alloy dispersed g-C_3N_4 predict the potential ability of the materials for the generation of SPR states as a result of photon absorption in the visible region. The assistance of the SPR in the photocatalytic degradation process is mainly governed by either direct injection of electrons from the excited plasmonic state to conduction band (CB) of semiconductor or the strong enhancement of the electromagnetic field in the close vicinity of the excited plasmonic NPs [133]. Another significant effect of SPR is the increased path length of the incident photons due to the scattering from metal NPs however, strongly dependent on the size compatibility of the incident photons and metallic NPs (quantum size effect). In the current case, due to the mismatch of the size of the incident photons with that of Ag, Au or Ag-Au alloy NPs, the contribution of the increased path length in enhancing the photocatalytic activity is less likely. Additionally, the contribution of electromagnetic near field mechanism requires a close correlation in the energies associated with SPR and the semiconductor with an effective overlap of SPR band and the incident light spectrum [134] which is not well defined in the current case. Therefore, it might be presumed that SPR contributes to the enhanced activity of the Ag, Au or Ag-Au alloy loaded catalysts by the direct electron injection (charge transfer) to the conduction band of the semiconductor as the Fermi levels of Au and Ag are located between the conduction and valence band of g-C_3N_4 [135, 136].

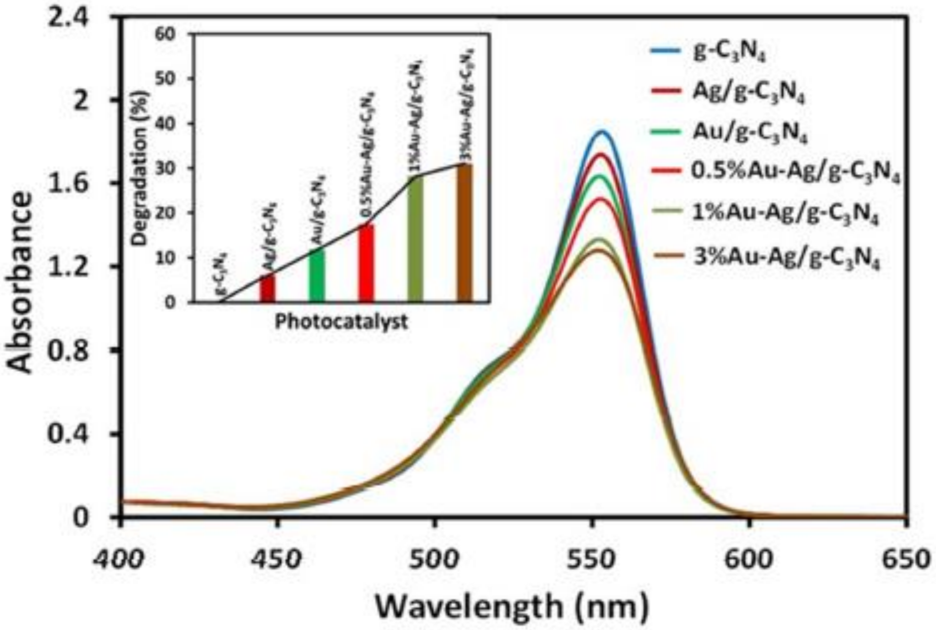

Figure 4.28 Comparison of the SPR assisted degradation of rhodamine B in the presence of g-C_3N_4, Ag/g-C_3N_4, Au/g-C_3N_4, 0.5%Au-Ag/g-C_3N_4, 1%Au-Ag/g-C_3N_4 and 3%Au-Ag/ g-C_3N_4 extravted by using 532nm (green) laser as SPR generated light source. The inset shows the percentage decrease in the concentration of rhodamine B for the respective catalysts.

Therefore, it can be inferred that the enhanced degradation of Rhodamine B both in the visible light and complete spectrum sunlight exposure is not accomplished by a single mechanism. The metallic NPs present at the surface of g-C_3N_4, either pure or alloy, contribute in the charge trapping and transfer of the photon generated charge carriers (electrons) in the conduction band of g-C_3N_4 at varying extent that results in the reduced electron-hole recombination and increased catalytic activity. The reduced emission intensities in the PL analysis of the metal NPs loaded catalysts compared to the pure g-C_3N_4 supports reduction in the recombination rate (mechanism I) as shown in fig 4.29. As Au and Ag are the electron rich elements, the capture of excited electrons and the provision of excessive energy from the plasmonic states may result in the localization of excessive negative charge and the shifting of the Fermi levels to more negative potential thus initiating the probability of the back donation of electrons to the conduction band of g-C_3N_4. Moreover, the noble metal NPs may also act directly as catalytic site for reduction reaction and formation of superoxide anion radicals (mechanism II) [137, 138] as displayed in fig 4.29. As this cycle propagates under illumination the absorption of the photons directly by the dye molecules and their contribution in the indirect photocatalytic degradation of the dye cannot be completely ignored. Although, the possibility of occurrence of a variety of reactions has been discussed above, however, the precise mechanism is still a subject of research. The pictorial explanation of the dominant mechanisms is presented in fig 4.29 below.

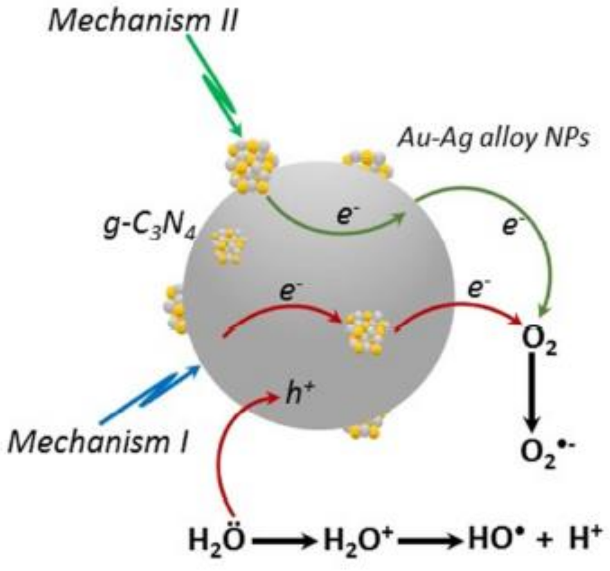

Figure 4.29 The plausible mechanisms of ROS generation involved in the degradation of Rhodamine B over Au-Ag alloy NP dispersed g-C_3N_4 in visible light and complete spectrum sunlight exposure.

Scheme 1: The plausible mechanisms of ROS generation involved in the degradation of Rhodamine B over Au-Ag alloy NP dispersed g-C_3N_4 in visible light and complete spectrum sunlight exposure.

The possible role of the SPR states in the degradation process of Rhodamine B was further investigated and verified by exposing the samples (Ag, Au and Au-Ag alloy) to the monochromatic light i.e. 532 nm laser for a fixed period. The degradation profile of 10 ppm Rhodamine B over various catalysts is presented in the Fig 4.28, whereas, the inset presents the comparative graphical evaluation of the percentage degradation of the dye over all the catalysts. As mentioned earlier, the Au-Ag alloys possess strong absorption bands in the visible region at ~536 nm. The choice of 532 nm monochromatic light was based on the excitation of metal or metal alloy NPs for the generation of SPR states. Compared to pure g-C_3N_4, the decrease in the concentration of dye, at varying extent, however, consistent with the increasing Au contents clearly demonstrated the role of SPR in the degradation process. Compared to ~6% decrease in dye concentration for Ag/ g-C_3N_4 (1% Ag), ~12% of the dye was degraded over Au/g-C_3N_4 (1%Au) whereas ~28% of the dye was removed by 1% Au-Ag alloy/g-C_3N_4composed of 1%Ag and 1% Au that showed the enhanced response of the metals in the alloy from rather than individual metal. It was also noticed that the increase in Au contents to 3%, the alloy failed to maintain the linear increase in the degradation. This effect is probably due to the loss in the synergy between Au and Ag for the mutual sharing of electrons. This observation highlights the importance of the components of the alloy (Au & Ag) for optimized SPR efficiency. The Au-Ag alloy dispersed g-C_3N_4 showed excellent stability in the repeated exposures.

4.2.5 Conclusions

The dispersion of Au-Ag alloy NPs at the surface of g-C_3N_4 resulted in the significantly sustained and higher activity as compared to that of Au or Ag loaded g-C_3N_4. In Au-Ag alloy loaded catalysts, the Au protects Ag against oxidation whereas Ag enhances the ability of Au for better electron capture and transfer. The existence of synergy between Au and Ag in alloys enhanced the magnitude of SPR that contributed significantly in enhancing the degradation process. The composition of the components is an important parameter for optimal activity of the alloy NPs.

CHAPTER 5

CONCLUSION AND FUTURE PROSPECTS

5.1 Conclusion

- Graphitic carbon nitride was successfully prepared as a visible light driven photocatalyst from melamine by pyrolysis method.
- Metal oxide (tungstic oxide) was incorporated on the graphitic carbon nitride sheet to successfully improve its photoefficiency.
- Also, using photoimpregnation method, gold and silver alloy nanoparticles were deposited as dopants on the surface of the graphitic cxarbon nitride to enhance its efficiency through surface plasmon resonance effect.

- The morphology of the synthesized composites were studied using XRD, FESEM and HRTEM.
- Chemical evaluation was examined by XPS analysis for alloy doped graphitic carbon nitride.
- Metal oxide (WO_3) and transition metals (Au, Ag) doped nanoparticles were homogenously dispersed with high purity possessing narrow size distribution ranging from 10-50 nm.
- UV-Visible spectrophotometry was used to measure the band gap of the different synthesized composites.
- On application of the metal oxide composite to the degradation of rhodamine B, a blue shift was observed which indicate de-alkylation of the dye structure.
- Comparison of performance on exposure to visible light as against complete spectrum in the sunlight, was carried out.
- The optimum combination ratio was establish by the degree of degradation of the dye.
- The trend of the photocatalytic performance for the $WO_3(x)/g\text{-}C_3N_4(1-x)$ on rhodamine B degradation is in the order: $WO_3(0.1)/g\text{-}C_3N_4(0.9) > WO_3 > g\text{-}C_3N_4$
- For the alloy doped graphitic carbon nitride, the following trend was observed and established: $3\%Au\text{-}Ag/g\text{-}C_3N_4 > 1\%Au\text{-}Ag/g\text{-}C_3N_4 > 0.5\%Au\text{-}Ag/g\text{-}C_3N_4 > Au/g\text{-}C_3N_4 > Ag/g\text{-}C_3N_4 > g\text{-}C_3N_4$

5.2 Future Prospects

The following recommendation should be observed in the near future:

- More visible light driven catalyst should be synthesized since the larger part of the sunlight consist of the visible region of the spectrum.
- Other ways to reduce the recombination effect on graphitic carbon nitride should be looked into, to enhance its efficiency.
- Composites such as the metal oxide incorporated on a semiconductor and surface plasmon photocatalyst should be explored for more harvest of photons in the visible region and better charge carrier separation efficiency.
- Physical properties of the catalyst such as particle size, crystal structure and charge transfer mechanism should be thoroughly investigated.
- Interesting composite materials should be synthesized applying soft chemical approach for photocatalytic application in the future.
- These visible light driven catalysts should also be thoroughly explored for heavy metal and sulphate bacteria removal.

REFERENCES

1. Li, K., et al., *A critical review of CO2 photoconversion: Catalysts and reactors.* Catalysis Today, 2014. **224**: p. 3-12.
2. Stasinakis, A.S., <*Use of selected advanced oxidation processes (AOPs) for wastewater treatment A mini review.pdf*>. Global NEST Journal. **10**(No 3): p. 376-385.
3. Hongbo Fu, C.P., Wenqing Yao, and Yongfa Zhu, <*Visible-Light-Induced Degradation of Rhodamine B by Nanosized Bi2WO6 (2).pdf*>. J. Phys. Chem. B 2005. **109** p. 22432-22439.

4. Pourahmad, A., S. Sohrabnezhad, and E. Kashefian, *AgBr/nanoAlMCM-41 visible light photocatalyst for degradation of methylene blue dye.* Spectrochim Acta A Mol Biomol Spectrosc, 2010. **77**(5): p. 1108-14.
5. Chatterjee, D. and S. Dasgupta, *Visible light induced photocatalytic degradation of organic pollutants.* Journal of Photochemistry and Photobiology C: Photochemistry Reviews, 2005. **6**(2-3): p. 186-205.
6. Chang, F., et al., *A facile modification of g-C3N4 with enhanced photocatalytic activity for degradation of methylene blue.* Applied Surface Science, 2013. **280**: p. 967-974.
7. Xu, Y., et al., *A plasmonic photocatalyst of Ag/AgBr nanoparticles coupled with g-C3N4 with enhanced visible-light photocatalytic ability.* Colloids and Surfaces A: Physicochemical and Engineering Aspects, 2013. **436**: p. 474-483.
8. Cao, J., et al., *Ag/AgBr/g-C3N4: A highly efficient and stable composite photocatalyst for degradation of organic contaminants under visible light.* Materials Research Bulletin, 2013. **48**(10): p. 3873-3880.
9. Zhu, Y.-P., et al., *Carbon-Doped ZnO Hybridized Homogeneously with Graphitic Carbon Nitride Nanocomposites for Photocatalysis.* The Journal of Physical Chemistry C, 2014. **118**(20): p. 10963-10971.
10. Zhang, L., et al., *Elimination of BPA endocrine disruptor by magnetic BiOBr@SiO2@Fe3O4 photocatalyst.* Applied Catalysis B: Environmental, 2014. **148-149**: p. 164-169.
11. Fujishima, A.H., Kenichi, *Electrochemical Photolysis of Water at a Semiconductor Electrode.* Nature, 1972. **238**(5358): p. 37-38.
12. Sun, H. and S. Wang, *Research Advances in the Synthesis of Nanocarbon-Based Photocatalysts and Their Applications for Photocatalytic Conversion of Carbon Dioxide to Hydrocarbon Fuels.* Energy & Fuels, 2014. **28**(1): p. 22-36.
13. Shi, H., et al., *Polymeric g-C3N4Coupled with NaNbO3Nanowires toward Enhanced Photocatalytic Reduction of CO2into Renewable Fuel.* ACS Catalysis, 2014. **4**(10): p. 3637-3643.
14. Ohno, T., et al., *Photocatalytic reduction of CO2 over a hybrid photocatalyst composed of WO3 and graphitic carbon nitride (g-C3N4) under visible light.* Journal of CO2 Utilization, 2014. **6**: p. 17-25.
15. Phairat Usubharatana, D.M., * Amornvadee Veawab, and Paitoon Tontiwachwuthikul, *<Photocatalytic Process for CO2 Emission Reduction from Industrial Flue Gas.pdf>.* Ind. Eng. Chem. Res. , 2006,. **45,** : p. 2558-2568.
16. Cao, L., et al., *Carbon nanoparticles as visible-light photocatalysts for efficient CO2 conversion and beyond.* J Am Chem Soc, 2011. **133**(13): p. 4754-7.
17. Ge, L., et al., *Enhanced visible light photocatalytic hydrogen evolution of sulfur-doped polymeric g-C3N4 photocatalysts.* Materials Research Bulletin, 2013. **48**(10): p. 3919-3925.
18. Zhang, F.-J., et al., *A novel photofunctional g-C3N4/Ag3PO4 bulk heterojunction for decolorization of Rh.B.* Chemical Engineering Journal, 2013. **228**: p. 435-441.
19. Das, S. and W.M.A. Wan Daud, *Photocatalytic CO2 transformation into fuel: A review on advances in photocatalyst and photoreactor.* Renewable and Sustainable Energy Reviews, 2014. **39**: p. 765-805.

20. Gondal, M.A., et al., *Preparation of WO3/g-C3N4 composites and their enhanced photodegradation of contaminants in aqueous solution under visible light irradiation.* Reaction Kinetics, Mechanisms and Catalysis, 2014.
21. Debabrata Chatterjee, A.M., *<Visible light induced photodegradation of organic pollutants.pdf>*. Journal of Photochemistry and Photobiology A: Chemistry 2002 **153** p. 199-204.
22. Debabrata Chatterjee∗, A.M., *Visible light induced photodegradation of organic pollutants*

on dye adsorbed TiO2 surface. 2002.
23. Kondo, K., et al., *Development of highly efficient sulfur-doped TiO2 photocatalysts hybridized with graphitic carbon nitride.* Applied Catalysis B: Environmental, 2013. **142-143**: p. 362-367.
24. P.N.Palanisamy, S.K.K., *<Photocatalytic Degradation of Vat Yellow 4 Using UV TiO2.pdf>*. Modern Applied Science, 2010. **Vol. 4,**(No. 5;).
25. Wang X1, M.K., Thomas A, Takanabe K, Xin G, Carlsson JM, Domen K, Antonietti M., *A metal-free polymeric photocatalyst for hydrogen production from water under visible light.* Nat Mater. , 2009 Jan. **8(1):** : p. 76-80.
26. Bian, Z., et al., *Au/TiO2 superstructure-based plasmonic photocatalysts exhibiting efficient charge separation and unprecedented activity.* J Am Chem Soc, 2014. **136**(1): p. 458-65.
27. S. Link, Z.L.W., ‡ and M. A. El-Sayed, *<Alloy Formation of Gold-Silver Nanoparticles and the Dependence of the Plasmon Absorption on Their Composition.PDF>*. J. Phys. Chem. B, , 1999. **Vol. 103,**(No. 18,).
28. Verbruggen, S.W., et al., *Plasmonic gold–silver alloy on TiO2 photocatalysts with tunable visible light activity.* Applied Catalysis B: Environmental, 2014. **156-157**: p. 116-121.
29. Gondal, M.A., et al., *Plasmon resonance enhanced photocatalysis under visible light with Au/Cu-TiO2 nanoparticles: Removal Cr (VI) from water as a case of study.* Science of Advanced Materials, 2013. **5**(12): p. 2007-2014.
30. Gondal, M.A., et al., *Sol-gel synthesis of Au/Cu-TiO2 nanocomposite and their morphological and optical properties.* IEEE Photonics Journal, 2013. **5**(3).
31. Gondal, M.A., et al., *Enhanced photoactivity on Ag/Ag3PO4 composites by plasmonic effect.* J Colloid Interface Sci, 2013. **392**: p. 325-30.
32. J. Shieh, H.M.F., M.H. Hon, H.Y. Juang, *WO3 and W-Ti-O thin film gas sensors prepared by sol gel dip-coating.* Sensors and Actuators B, 2002. **86**: p. 75-80.
33. Gondal, M.A., et al., *Photocatalytic removal of hazardous dye from water using nanostructured WO3.* International Journal of Nanoparticles, 2011. **4**(1): p. 53-63.
34. Ju, P., et al., *A novel calcined Bi2WO6/BiVO4 heterojunction photocatalyst with highly enhanced photocatalytic activity.* Chemical Engineering Journal, 2014. **236**: p. 430-437.
35. Chai, S.Y., et al., *Heterojunctioned BiOCl/Bi2O3, a new visible light photocatalyst.* Journal of Catalysis, 2009. **262**(1): p. 144-149.
36. Chang, X., et al., *Photodegradation of Rhodamine B over unexcited semiconductor compounds of BiOCl and BiOBr.* J Colloid Interface Sci, 2012. **377**(1): p. 291-8.
37. Wang, X., S. Blechert, and M. Antonietti, *Polymeric Graphitic Carbon Nitride for Heterogeneous Photocatalysis.* ACS Catalysis, 2012. **2**(8): p. 1596-1606.

38. Wang, Y., X. Wang, and M. Antonietti, *Polymeric graphitic carbon nitride as a heterogeneous organocatalyst: from photochemistry to multipurpose catalysis to sustainable chemistry.* Angew Chem Int Ed Engl, 2012. **51**(1): p. 68-89.
39. Jiang, F., et al., *A g-C3N4–CdS composite catalyst with high visible-light-driven catalytic activity and photostability for methylene blue degradation.* Applied Surface Science, 2014. **295**: p. 164-172.
40. Shi, S., et al., *Synthesis of g-C3N4/BiOClxBr1−x hybrid photocatalysts and the photoactivity enhancement driven by visible light.* Colloids and Surfaces A: Physicochemical and Engineering Aspects, 2014. **461**: p. 202-211.
41. Ge, L., C. Han, and J. Liu, *Novel visible light-induced g-C3N4/Bi2WO6 composite photocatalysts for efficient degradation of methyl orange.* Applied Catalysis B: Environmental, 2011. **108-109**: p. 100-107.
42. Liu, W., et al., *Facile synthesis of g-C3N4/ZnO composite with enhanced visible light photooxidation and photoreduction properties.* Chemical Engineering Journal, 2012. **209**: p. 386-393.
43. Tian, Y., et al., *Graphitic carbon nitride/Cu2O heterojunctions: Preparation, characterization, and enhanced photocatalytic activity under visible light.* Journal of Solid State Chemistry, 2014. **212**: p. 1-6.
44. Sridharan, K., E. Jang, and T.J. Park, *Novel visible light active graphitic C3N4–TiO2 composite photocatalyst: Synergistic synthesis, growth and photocatalytic treatment of hazardous pollutants.* Applied Catalysis B: Environmental, 2013. **142-143**: p. 718-728.
45. Yan, H. and H. Yang, *TiO2–g-C3N4 composite materials for photocatalytic H2 evolution under visible light irradiation.* Journal of Alloys and Compounds, 2011. **509**(4): p. L26-L29.
46. Han, C., et al., *Novel visible light induced Co3O4-g-C3N4 heterojunction photocatalysts for efficient degradation of methyl orange.* Applied Catalysis B: Environmental, 2014. **147**: p. 546-553.
47. Cao, S.-W., et al., *Solar-to-fuels conversion over In2O3/g-C3N4 hybrid photocatalysts.* Applied Catalysis B: Environmental, 2014. **147**: p. 940-946.
48. Wang, S., et al., *Synthesis and characterization of g-C3N4/Ag3VO4 composites with significantly enhanced visible-light photocatalytic activity for triphenylmethane dye degradation.* Applied Catalysis B: Environmental, 2014. **144**: p. 885-892.
49. Huang, L., et al., *Synthesis and characterization of g-C3N4/MoO3 photocatalyst with improved visible-light photoactivity.* Applied Surface Science, 2013. **283**: p. 25-32.
50. Li, T., et al., *Synthesis of g-C3N4/SmVO4 composite photocatalyst with improved visible light photocatalytic activities in RhB degradation.* Applied Catalysis B: Environmental, 2013. **129**: p. 255-263.
51. Ge, L. and C. Han, *Synthesis of MWNTs/g-C3N4 composite photocatalysts with efficient visible light photocatalytic hydrogen evolution activity.* Applied Catalysis B: Environmental, 2012. **117-118**: p. 268-274.
52. Zhou, X., et al., *Synthesis of porous Fe3O4/g-C3N4 nanospheres as highly efficient and recyclable photocatalysts.* Materials Research Bulletin, 2013. **48**(4): p. 1447-1452.
53. Dong, G., et al., *Facile synthesis of porous graphene-like carbon nitride (C6N9H3) with excellent photocatalytic activity for NO removal.* Applied Catalysis B: Environmental, 2015. **174-175**: p. 477-485.

54. Wang, K., et al., *Sulfur-doped g-C3N4 with enhanced photocatalytic CO2-reduction performance.* Applied Catalysis B: Environmental, 2015. **176-177**: p. 44-52.
55. He, Y., et al., *High-efficiency conversion of CO2 to fuel over ZnO/g-C3N4 photocatalyst.* Applied Catalysis B: Environmental, 2015. **168-169**: p. 1-8.
56. Chen, L., et al., *Gold nanoparticle-graphite-like C3N4 nanosheet nanohybrids used for electrochemiluminescent immunosensor.* Anal Chem, 2014. **86**(9): p. 4188-95.
57. Zhang, S., et al., *In situ ion exchange synthesis of strongly coupled Ag@AgCl/g-C(3)N(4) porous nanosheets as plasmonic photocatalyst for highly efficient visible-light photocatalysis.* ACS Appl Mater Interfaces, 2014. **6**(24): p. 22116-25.
58. Samanta, S., S. Martha, and K. Parida, *Facile Synthesis of Au/g-C3N4Nanocomposites: An Inorganic/Organic Hybrid Plasmonic Photocatalyst with Enhanced Hydrogen Gas Evolution Under Visible-Light Irradiation.* ChemCatChem, 2014: p. n/a-n/a.
59. Bu, Y., Z. Chen, and W. Li, *Using electrochemical methods to study the promotion mechanism of the photoelectric conversion performance of Ag-modified mesoporous g-C3N4 heterojunction material.* Applied Catalysis B: Environmental, 2014. **144**: p. 622-630.
60. Kundu, M.K., M. Sadhukhan, and S. Barman, *Ordered assemblies of silver nanoparticles on carbon nitride sheets and their application in the non-enzymatic sensing of hydrogen peroxide and glucose.* J. Mater. Chem. B, 2015. **3**(7): p. 1289-1300.
61. Ong, W.J., et al., *Heterojunction engineering of graphitic carbon nitride (g-C3N4) via Pt loading with improved daylight-induced photocatalytic reduction of carbon dioxide to methane.* Dalton Trans, 2015. **44**(3): p. 1249-57.
62. Xu, M., L. Han, and S. Dong, *Facile fabrication of highly efficient g-C3N4/Ag2O heterostructured photocatalysts with enhanced visible-light photocatalytic activity.* ACS Appl Mater Interfaces, 2013. **5**(23): p. 12533-40.
63. Zaiwang Zhao a, Y.S.a., Fan Dong, *<Graphitic carbon nitride based nanocomposites A review.pdf>*. Nano scale, 2014.
64. Zhai, H.-S., L. Cao, and X.-H. Xia, *Synthesis of graphitic carbon nitride through pyrolysis of melamine and its electrocatalysis for oxygen reduction reaction.* Chinese Chemical Letters, 2013. **24**(2): p. 103-106.
65. Q, F., *Encyclopedia of atmospheric sciences.* Academic Press, London, , 2002: p. pp 1859–1863.
66. Khan, H. and D. Berk, *Synthesis, physicochemical properties and visible light photocatalytic studies of molybdenum, iron and vanadium doped titanium dioxide.* Reaction Kinetics, Mechanisms and Catalysis, 2013. **111**(1): p. 393-414.
67. Asahi R, M.T., Ohwaki T, Aoki K, Taga Y Science, (2001) **293:**: p. 269–271.
68. Chen X, L.L., Yu P, Mao S Science 2011 **331:**: p. 746-750.
69. Wu CH, K.C., Lai CH, Chung WY Reac Kinet Mech Cat 2014 **111:**: p. 383–392.
70. Yu XN, L.Z., Wu D, Yu P, He M, Chen TT, Shi WD, Huo PW, Yan YS, Feng YX, Reac Kinet Mech Cat 2014 **111:**: p. 347–360.
71. Chakraborty AK, R.M., Hossain ME, Sobahan KMA, Reac Kinet Mech Cat, (2014) **111:**: p. 371–382.
72. Zou Z, Y.J., Sayama K, Arakawa H, Nature (2001). **414:**: p. 625–627.
73. Yi Z, Y.J., Kikugawa N, Kako T, Ouyang S, Hilary S, Yang H, Cao J, Luo W, Li Z, Liu Y, Withers R, Nat Mater (2010) **9:**: p. 559–564.

74. Wang X, M.K., Thomas A, Takanabe K, Xin G, Carlsson J, Domen K, Antonietti M Nat Mater (2008) **8:**: p. 76–80.
75. Pan H, L.X., Zhuang Z, Zhang C J Mol Catal A (2011) **345:**(90–95).
76. Yan S, L.S., Li Z, Zou Z Dalton Trans (2010) **39:**: p. 1488–1491.
77. Pan C, X.J., Wang Y, Li D, Zhu Y Adv Funct Mater (2012) **22:**(1518–1524).
78. Kai Shen a, Mohammed Ashraf Gondal b,#, Rashid Ghulam Siddique b, Shan Shi a, Siqi Wang a, and Q.X.c. Jiangbo Sun a, *Preparation of ternary Ag/Ag3PO4/g-C3N4 hybrid photocatalysts and their enhanced photocatalytic activity driven by visible light.* Chinese Journal of Catalysis, 2014. **35** p. 78–84.
79. Katsumata K, M.R., Matsushita N, Okada K J Hazard Mater (2013). **260:**: p. 475–482.
80. Hussain ST, R., Anjum D, Siddiqa A, Badshah A Mater Sci Bull (2013) **48:**: p. 705–714.
81. L, G., Mater Lett (2011) **65:**: p. 2652–2654.
82. Yan S, L.Z., Zou Z Langmuir (2009) **25**: p. 10397–10401.
83. Siqqiqui MN, G.M., Environ Sci Heal A 2011. **46:**: p. 1154–1159.
84. Siqqiqui MN, G.M., J Environ Sci Heal A (2014) **49:**: p. 52–58.
85. Hayat K, G.M., Khaled MM, Ahmed S, Shemsi AM Appl Catal A (2011) **393:**: p. 122–129.
86. Lu J, D.I., Drzal LT, Worden RM, Lee I, ACS Nano (2008) **2:**: p. 1825–1832.
87. Xu, H., et al., *Novel visible-light-driven AgX/graphite-like C3N4 (X=Br, I) hybrid materials with synergistic photocatalytic activity.* Applied Catalysis B: Environmental, 2013. **129**: p. 182-193.
88. Shen K, G.M., Li ZJ, Li LY, Xu QY, Yamani ZH Reac Kinet Mech Cat (2013) **109:**: p. 247–258.
89. Gondal MA, S.M., Alarfaj A, Chem Phys Lett (2007) **445:**: p. 325–330.
90. Chen CC, W.M., Zhao JC Chem Soc Rev (2010) **39:**: p. 4206–4219.
91. R. Asahi, T.M., T. Ohwaki, K. Aoki and Y. Taga, , Science,, 2001, . **293,** : p. 269–271.
92. X. Chen, L.L., P. Yu and S. Mao,, Science. , 2011, . **331,**: p. 746–750.
93. M. Aslam, I.M.I.I., N. Salah, S. Chandrasekaran, M. T. Qamar and A. Hameed,, J. Hazard. Mater., , 2014, . **286C,** : p. 127-135.
94. M. Aslam, I.M.I.I., S. Chandrasekaran and A. Hameed, , J. Hazard. Mater., , 2014, . **276,**: p. 120-128.
95. Y. Cui, Z.D., P. Liu, M. Antonietti, X. Fu and X. Wang, , Phys. Chem. Chem. Phys.,

, 2012, . **14,**: p. 1455-1462.
96. H. Pan, X.L., Z. Zhuang and C. Zhang J. Mol, , Catal. A: Chem., , 2011, . **345,** : p. 90-95.
97. S. Yan, S.L., Z. Li, Z. Zou and Dalton Trans, , Chem. Commun., , 2010, . **39,** : p. 1488.
98. C. Pan, J.X., Y. Wang, D. Li and Y. Zhu,, Adv. Funct. Mater., , 2012, . **22,** : p. 1518-1524.
99. L. Ge, C.H., J. Liu, and Y. Li,, Appl. Catal., A, , 2011, . **409-410,** : p. 215-222.
100. Y. Wang, R.S., J. Lin and Y. Zhu, , Energy. Environ. Sci., , 2011, . **4,** : p. 2922-2929.
101. S. Kumar, T.S., A. Baruah and V. Shanker,, J. Mater. Chem., A, , 2013, . **1,** : p. 5333-5340.
102. L. Ge, C.H., and J. Liu, , Appl. Catal., B., , 2011, . **108-109,** : p. 100-107.
103. J. Fu, Y.T., B. Chang, F. Xi, and X. Dong, , J. Mater. Chem., A,, 2012, . **22,** : p. 21159-21166.
104. J. Zhang, X.C., K. Takanabe, K. Domen, J. Epping, X. Fu, M. Antonietti and X. Wang, , Angew. Chem. Int. Ed., Angew. Chem.,, 2010, . **49, 122,** : p. 441- 444; 451 -454.

105. Y. Wang, J.Z., X. Wang, M. Antonietti and H. Li, . Angew. Chem. Int. Ed., Angew. Chem., , 2010, . **49, 122,** : p. 3428 -3431; 356 -3359;.
106. Y. Bu, Z.C.a.W.L., App. Catal. B. Env., , 2014, . **144,** : p. 622– 630.
107. Y. Chen, W.H., D. He, Y. Situ and H. Huang, , ACS. Appl. Mater. Interfaces., , 2014,. **6,** : p. 14405−14414.
108. X. Bai, R.Z., C. Li, D. Liu, Y. Liu, Y. Zhu, , App. Catal. B. Env., , 2014, . **147,** : p. 82–91.
109. M. Xu, L.H.a.S.D., ACS. Appl. Mater. Interfaces., , 2013, . **5,** : p. 12533−12540.
110. H. Li, J.L., W. Hou, Na Du, R. Zhang, X. Tao, , Appl. Catal. B: Environ., , 2014, . **160–161,**: p. 89–97.
111. J. Turkevich, P.C.S., J. Hillier, , *Discuss. Far. Soc.*, . 1951, . **11,** : p. 55–75.
112. M. A. Gondal, A.H.a.A.S., Appl. Catal., A, , 2003, . **243,** : p. 165–174.
113. Gondal, M., et al., *Production of hydrogen and oxygen by water splitting using laser induced photo-catalysis over FeO.* Applied Catalysis A: General, 2004. **268**(1-2): p. 159-167.
114. A. Hameed and M. A. Gondal, J. Mol. Catal. A: Chem., , 2005, . **233,**: p. 35–41.
115. M. A. Gondal, A.H., Z. H. Yamani and A. Suwaiyan, , Appl. Catal. A, , 2004, . **268,**: p. 159–167.
116. C. Noguez, J. Phys. Chem. C, , 2007, . **111,** : p. 3806-3819.
117. M. Bahram, E.M., Anal. Methods, , 2014, . **6,** : p. 6916–6924.
118. X. Wang, K.M., A. Thomas, K. Takanabe, G. Xin, J. M. Carlsson, K. Domen and M. Antonietti, M., Nat. Mater., , 2009,. **8,** : p. 76 - 80.
119. Z. Wang, W.G., Y. Sun, F. Dong, Y. Zhou and W. K. Ho, , Nanoscale, , 2015, . **7,** : p. 2471-2479.
120. Z. Zhao, Y.S.a.F.D., Nanoscale, , 2015, . **7,** : p. 15-37.
121. L. Ge, C.H., J. Liu and Y. Li, , Appl. Catal. A, , 2011, . **409–410,** : p. 215–222.
122. X. Wang, K.M., A. Thomas, K. Takanabe, G. Xin, J. M. Carlsson, K. Domen and M. Antonietti, M., Nat. Mater., , 2009,. **8,**: p. 76–80.
123. B. Rodriguez-Gonzalez, A.S.-I., M. Giersig and L.M. Liz-Marzan, , Far. Discuss., , 2004, . **125,** : p. 133–144.
124. S. Link, Z.L.W.a.M.A.E.-S., J. Phys. Chem. B,, 1999, . **103,** : p. 3529-3533.
125. X. Lu, Q.W.a.D.C., J. Mater. Sci. Technol., , 2010, . **26,** : p. 925-930.
126. X. Bai, L.W., R. Zong and Y. Zhu, , J. Phys. Chem. C, , 2013, . **117,** : p. 9952−9961.
127. A. Hameed, I.M.I.I., M. Aslam and M. A. Gondal, , Appl. Catal. A, , 2014, . **470,** : p. 327–335.
128. C. S. Turchi and D. F. Ollis, J. Catal., , 1990, . **122,** : p. 178-192.
129. P. Pichat, *Photocatalysis and water purification: from fundamentals to recent applications (1st ed.). Germany:* . Wiley-VCH, , 2013.
130. M. A. Henderson, *A surface science perspective on TiO2 photocatalysis.* . Surf. Sci. Rep., , 2011, . **66,**: p. 185–297.
131. M. Aslam, I.M.I.I., S. Chandrasekaran, H. A. Qari and A. Hameed, , Water Air and Soil Pollut.,, 2015, . **226,**: p. 70.
132. M. Aslam, I.M.I.I., S. Chandrasekaran, H. A. Qari and A. Hameed, , Water Air and Soil Pollut., , 2015, . **226,**: p. 70.
133. S. Linic, P.C., D.B. Ingram, , Nat. Mater,. , 2011, . **10,**: p. 911–921.

134. Z. W. Liu, W.B.H., P. Pavaskar, M. Aykol and S. B. Cronin, , Nano. Lett., , 2011, . **11,** : p. 1111-1116.
135. Y. Chen, W.H., D. He, Y. Situ and H. Huang, , ACS Appl. Mater. Interfaces, , 2014, . **6,**: p. 14405−14414.
136. D. B. Ingram, P.C., J. L. Bauer and S. Linic, , ACS Catal. , 2011,. **1,** : p. 1441–1447.
137. M. J. Kale, T.A., P. Christopher, , ACS Catal. , 2014, . **4,**: p. 116–128.
138. N. Cheng, J.T., Q. Liu, C. Ge, A. H. Qusti, A. M. Asiri, A. O. Al-Youbi and X. Sun,, ACS Appl. Mater. Interfaces, , 2013, . **5,** : p. 6815−6819.

Vitae

Name	:Adekolapo Adeniran Adesida
Nationality	:Nigerian
Date of Birth	:11/18/1982
Email	:adekolapo82@gmail.com
Address	:26 Ojodu berger, Lagos, Nigeria
Academic Background	:2013-2015 Masters in Chemistry

2013-2015 Masters in Chemistry

Synthesis of visible light driven catalys for water treatment via photcatalysis

King Fahd University of Petroleum, Saudi Arabia.

2007-2010 Bachelors in Sciences (Industrial Chemistry)

Assessment of water source around a pharmaceutical company

Ajayi Crowther University.

Publication (peer-reviewed)

1. *Preparation of WO_3/g-C_3N_4 composites and their enhanced photodegradation of contaminants in aqueous solution under visible light irradiation*

http://link.springer.com/article/10.1007%2Fs11144-014-0787-y

2. Synthesis, characterization and surface plasmon resonance (SPR) enhanced photocatalytic activity of Au-Ag alloy nanoparticles dispersed on g-C_3N_4

Conferences

1) International Petroleum Technology Conference, Qatar (2014).
2) The 3rd Saudi International Nanotechnology Conference 2014 (3SINC)